MICROLENS ARRYS FABRICATION TECHNIQUE

AND

ITS APPLICATION IN SURFACE NANOPATTERNING

BY

LIM CHIN SEONG (B. Eng (Hons))

DEPARTMENT OF MECHANICAL ENGINEERING

A DISSERTATION SUBMITTED IN PARTIAL FULFILMENT OF THE

REQUIREMENT FOR THE DEGREE OF

DOCTOR OF PHILOPOPHY OF ENGINEERING

NATIONAL UNIVERSITY OF SINGAPORE

2008

ACKNOWLEDGEMENT

I would like to express my earnest thankfulness to my supervisors, Prof. M. Rahman, A/Prof. A. Senthil Kumar and A/Prof. Hong Minghui, for their guidance and great support during the entire project. Without their invaluable advices and encouragements, progress of this project will not be as smooth as it is. Prof Hong’s acute sense in most recent trends of optics and laser technology provides me the valuable ideas in both my experimental setup and theoretical study.

I would also like to thank Dr Lin Ying, Dr. Chen Guoxin, Dr Wang Zengbo, Mr Zhou Yi and other staff and students of ECE-DSI Laser Microprocessing Lab for the countless helpful discussions with me during my research work. They also shared their experiences of studying and living during the past years. I deeply appreciate the time with them.

On a personal note, I would like to thank my mum for her great encouragement and constant support during my years of pursuing higher degree in National University of Singapore. I also deeply appreciate my sisters and brother for their care and support.

Lastly, I wish to acknowledge the scholarship provided by Singapore Institute of Manufacturing Technology for my PhD degree in the past 3 years.

TABLE OF CONTENTS

SUMMARY

Microlens array is one of the micro-optical elements consisting of a series of miniaturized concave or convex lenses that are arranged in certain form. In recent years, microlens array has attracted more and more attentions because the device miniaturization requires the optical elements to be miniaturized as well. Therefore, a lot of researches are being carried out on the fabrication techniques of microlens array and their applications. In this thesis, it is aimed to study and develop novel microlens array fabrication techniques, which can greatly improve the fabrication flexibility and reduce the production cost. The potential application of the microlens array in large area surface nanopatterning is also demonstrated.

Various types of microlens arrays with different dimensions are successfully produced by laser-assisted patterning and etching process. The concave microlens array is fabricated by laser direct writing followed by chemical wet etching whereas the combination of laser interference lithography (LIL) and reactive ion etcing (RIE) produce the convex microlens array. The direct patterning by laser offers an alternative in microlens array fabrication process, which is more flexible in terms of design change and the microlens dimensional control, thus eliminating the need of using expensive photo masks to define the microlenses dimension. The physical and optical properties of these fabricated microlens arrays are examined by numerous characterization methods.

Optical characteristics of the fabricated microlens array are modeled and studied by the simulation of wave propagation through the microlens array. Ray tracing and physical optics propagation techniques are used to simulate microlenses of few tenth micron of size while finite-difference time-domain (FDTD) method is more suitable when the microlenses size is approaching wavelength of the light. The simulation results of the intensity distribution are well matched to the experimental observations. The effect of different sag heights on the spot size and intensity at the focal plane is also presented.

The last part of the thesis demonstrates the use of microlens array in the surface nanopatterning of photopolymer materials. This nanopatterning technique utilized the laser irradiation through a microlens arrays to generate many tiny light spots which act as a series of ‘nano-pens’ for direct writing purposes. These identical nano-features are patterned in a single or multiple pulses of laser irradiation over a large area, which increases the patterning efficiency. The effects of laser pulse number, fluence and fractional Talbot plane on the feature size are studied. Super-resolution surface nanopatterning of sub-100nm pattern can be achieved by proper control of irradiation dose. The MLA-based surface nanopatterning has a great potential in various applications, such as patterning of optical/magnetic storage media and fabrication of photonic crystals or other periodic structures.

LIST OF TABLES

LIST OF FIGURES

LIST OF SYMBOLS

F	Laser fluence	M	Molarity by weight
λ	Laser wavelength	H	Packing Density
p_x	x-pitch of microlens array	p_y	y-pitch of microlens array
r	Radius of microlens	F^-	Fluorine ion
θ	Angle of two beams intersect	P	Period of interference pattern
T	Temperature	T_g	Glass transition temperature
ρ	Mass density	u	Flow speed
P_{int}	Internal pressure	P_{ext}	External pressure
g	Dynamic viscosity	g	Gravitational acceleration
γ	Surface tension	R	Surface curvature radius
Ra	Average mean roughness	D	Diameter of lens
k	Wave number	$\vec{e}$	Direction vector
$\vec{r}$	Position vector	v	Spatial frequency components of the plane wave
H	Magnetic field component	E	Electric field component
D	Electric flux density	J	Free current charge density
B	Magnetic field density	M	Magnetization density
P	Polarization density	σ	Electric conductivity
χ_m	Magnetic susceptibility of the material	χ_e	Electrical susceptibility of the material

ε	Permittivity of the material	μ	Permeability of the material
t	Time	n	Refractive index
S	Poynting vector	r	Lateral resolution of a focused light beam
τ	Pulse width	f	Focal length
R	Radius of curvature	h	Sag height
d_{min}	Minimum spot size		

CHAPTER 1

INTRODUCTION

In the past decades the study of light propagation behavior and its applications in optical engineering have drawn a lot of attentions from researchers in various fields. The researches include the fundamental study of optical properties of light, design of optical components and systems as well as the applications of these optical elements. These research activities were being carried out extensively mainly due to the unique properties of light, whereby the light can be reflected, refracted and diffracted by several means. The unique properties of light have made optical engineering as one of the important factors in stimulating the rapid growth of microelectronics, biological science and optical data storage industries. For the engineering application purposes, numerous optical elements are used individually or integrated with other elements to form an integrated optics. These optical elements appear in various sizes, from few centimeters down to several tenths of micrometers, depending on the applications and size of the engineering devices.

According to Sinzinger et. al. [1], the areas of optics are divided into 3 categories; classical optics, fiber optics and micro-optics which are classified based on the dimension of these optics as well as their fabrication techniques. Classical optics is referring to the conventional “macro-optics” components that are fabricated using grinding or polishing [2]. Due to the rapid development of miniaturization in electrical and electronic devices, there is a need to further miniaturize the corresponding optical elements integrated into these micro-devices. This process of optical elements miniaturization has led to the term “micro-optics”.

1.1 Overview of micro-optics

Micro-optics is one of the optical elements that is widely used in various micro-devices, such as micro/nano-electromechanical system (MEMS/NEMs), microfludic components, semiconductor lasers, micro-sensors and actuators. The micro-optics is the optical part that is miniaturized into millimeter or even micrometer scales [3]. The miniaturization of these micro-optical elements is stimulated by the rapid development of micro- and nano-fabrication techniques used in semiconductor industry. These advanced fabrication techniques enable one to fabricate micro-optical components with the available lithography and etching techniques at minimal modification of the process parameters. In general, there are various categories of micro-optical elements, such as refractive micro-optics, diffractive optical elements (DOEs), optical waveguides and gradient index optics, etc. Within the family of refractive micro-optics, microlens array is one of the most commonly used and extensively researched micro-optical elements.

1.1.1 Refractive micro-optics – microlens array

Similar to its conventional macro-lens counterpart, microlens array (MLA) is one of the micro-optical elements that is used to refract and focus the incident light beam [4]. The difference is that it consists of series of miniaturized lenses in a certain form of arrangement, either squarely or hexagonally packed. These microlenses, whose surface profiles can be convex or concave depending on its applications, are normally cylindrical, square or hemispherical in shape. Therefore, when a single light beam is incident to a microlens array, thousands and sometimes millions of tiny light spots are generated at the focal plane of the microlens arrays, depending on the size of the microlenses. The formation of these arrays of tiny light spots makes the microlens array as one of the important components to be integrated into most of the micro-systems for optoelectronics, optical communications and other engineering applications.

1.1.2 Applications of microlens array

Microlens array has become one of the important features in the integration of various micro-systems for its ability to create multiple light spots and its smaller dimension as compared to conventional macro-optics. The rapid growth of optical communication and imaging has drawn much research interests in fabrication and integration of these micro-optical elements into the devices. In the area of optical imaging, microlens array functions as a 'copier' to transfer the image of an object to a screen or a detector when they are scanned through the documents as demonstrated by Borrelli et. al [5], Kawazu et. al [6] and Hutley et. al [7]. In their experiment, each microlens was used to image a portion of the object and copy onto a photo-sensor before it is printed out as photocopy. The photocopying efficiency of these copiers is highly dependent on the density of the microlens arrays and its precise alignment to the photo-sensor.

Meanwhile, microlens array is also widely integrated into 3D photography imaging and display devices. In an integral photography system, a highly packed microlens array is integrated into a camera to record the three dimensional images [8-11]. The resolution of the imaging is determined by the lens diameter and its focal length. Each microlens captures a micro-image or element image of the whole object and reconstructs the 3D image through another matching microlens array or computational stereo-matching algorithm [12] onto a display device, such as LCD screen [13]. This not only creates high resolution 3D images but also increases the depth of focus of imaging system [14]. Völkel et. al. [15,16] used the wafer-level packaging technique to align and stack microlens array with image sensor array. This combination gives better image quality, which is suitable for micro-cameras and CMOS imagers. Other applications of the microlens array in imaging systems include auto-focus during image snapping [17] and advanced optical imaging systems for LCD display [18-21]. In the design and development of confocal microscope for bio-imaging applications, microlens array is adopted into the system setup to enable the parallel scanning and processing of the sample surface topography. The advantages of having a microlens array in the confocal microscope include large field of view, while maintain the require resolution [22] and enhance the contrast of the fluorescence images [23].

Besides working as an imager, the microlens array was also used for detection of fluid and chemical flow inside a small channel in biochemical applications [24,25]. In a micro-total-analysis system (µTAS), the excitation beam was focused to the chemical and fluorescence emitted from the molecules was collected by a microlens array to the detector for further analyses. To detect and measure the dynamic heated air jet flow, microlens array was used together with a CCD camera to provide wavefront measurement. More recently microlens array was integrated into an optical system to create multiple laser spots that can act as optical tweezers [26]. These laser light spots created optical trapping, which is important for the manipulation of series of molecules and particles in an aqueous solution.

The coupling of laser light with optical fibers or fiber to fiber coupling is another important application of the microlens array [27-29]. The numerical aperture and precision positioning of the microlens array play a major role in achieving optimal performance to avoid any losses of the coupling effect. For optoelectronic devices, a microlens array acts as an interface between the source and the microelectronic structures such as CCD or sensor. Microlens array served as an “array illuminator” to distribute light signals to the chip that contains a series of detector sensors [30]. A 3 × 3 optoelectronic switch using VCSEL arrays was demonstrated using the microlens array to direct the laser beams to the photodetector array so that electrical signals can be generated [31].

Microlens array is also used in lithographic systems to project images onto resist layers. The “microlens lithography” technique consists of a stack of 3 ~ 4 layer microlens array, which were combined together to form an array of micro-objectives [32,33]. Each micro-objective projects a small part of the photomask onto photoresist and the complete mask image forms as these individual images overlap [33]. Using this concept of image projection, Wu et. al [34-36] created arrays of two dimensional micropatterns on photoresist by projecting a transparent mask pattern using a microlens arrays. This created uniform repetitive micropatterns over a large area.

More recently, Kato et. al [37] reported surface nanopatterning by illuminating a microlens array using a femtosecond laser. This nanolithography technique utilized a light source, usually a monochromatic light beam, to irradiate through a microlens array. The microlens array focused the incoming light and created a series of tiny light spots at the focal plane of the microlens arrays. The light spots were then projected onto a layer of photopolymerizable resin, which was then undergone photo-chemical reaction to change its material properties. This enabled thousands of identical two- and three-dimensional nano-features to be generated over a large area of the resin in a short time. Besides photopolymerizable materials, Lin et. al [38] demonstrated this surface nanopatterning could also be used on phase change material by phase transformation. The phase transformation is induced due to the heating effect when the energy intensity of the focused light beams is sufficiently high. By using the femtosecond laser as the light source, the transformation of the phase state was confined into a small region, usually in sub-200 micron range. This is because the interaction between phase change film and femtosecond laser is multi-photon absorption and therefore optically nonlinear. The above-mentioned microlens array surface nanopatterning technique offers some advantages over the other nanostructuring techniques in terms of throughput and industrialized feasibility. However, there are several research challenges, such as to reduce the feature size down to sub-nano regime at a lower cost and higher efficiency.

1.2 Microlens array fabrication techniques

There are various ways of fabricating the microlens array. Differ from the conventional grinding and polishing of glass materials for optical surface finish, the fabrication of microlens arrays generally requires more process steps. As it consists of arrays of microlenses on a planar surface, the fabrication is not as straight forward as single lens fabrication. Generally it involves a pattern generation and transfer through various microfabrication techniques.

As most of the microelectronic and optical system devices are getting smaller, the miniaturization of these lenses and improvement of their performance are essential so that the integration into the devices can lead to the stability and reliability of the devices. The alignment precision of the micro-lenses, control of the lens dimension accuracy, such as radius of curvature and diameter, etc as well as the surface quality are issues that draw a lot of attention from researchers from all over the world. In the past decade, numerous researches have been done and reported on the development of microlens array fabrication techniques. These techniques have their own advantages and disadvantages, depending on the suitability of the specific applications.

1.2.1 Photolithographic and thermal reflow

Most of the microlens arrays commercially available are fabricated using existing VLSI processing method. Popovic et. al [39] first demonstrated the formation of arrays of hemispherical microlenses on a substrate by thermal heating of the resist patterns. Using a pre-designed chromium photo mask with circular opaque patterns, an array of resist pillars were created on photoresist by photolithography. It was then followed by the heating of the photo resist which causing the resist to reflow into hemispherical microlens arrays. These resist microlens arrays were further transferred to the substrate by reactive ion etching (RIE) [40-42]. As a result, microlens arrays ere created permanently on the substrate. This technique enables the mass forming of microlens arrays with good surface finish quality.

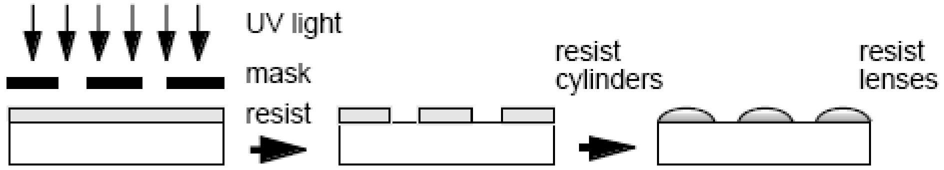

FIG. 1.1 Fabrication steps of microlens arrays using photolithography and thermal reflow process. The formed resist microlenses was then passed through an etching process to transfer the patterns onto the substrate [42].

1.2.2 Grey-tone mask pre-forming

On the other hand, in order to eliminate the need to heat the photoresist, some researchers used grey tone mask, a specially designed mask, which permits different amount of light intensity to go through the mask opening to directly form a hemispherical resist lenses [43-46]. This method enabled not only photoresist to be patterned but also some other light-sensitive materials, such as sol-gel [44] and dichromate gelatin [43]. However, the disadvantages of this method were the use of expensive photomasks, the lack of flexibility as the size of the microlenses was limited by the mask pattern and lastly, time consuming as it involved lots of process steps.

1.2.3 Laser direct writing

As the lithographic method requires the use of expensive photomask and the lacked of flexibility to design changes, there were other researchers who generated patterns directly without the need of photo mask. Numerous researchers [47-51] reported the method of lens profile generation using modulated laser beam scanning system. This can be accomplished by using a so called laser pattern generator, which modulates the exposure dosage by changing the dwell time, scanning speed or irradiation laser power. As the photoresist is sensitive to the exposure dosage, changing the beam intensity while scanning across the substrate produces optical structures on the photoresist, which was subsequently transferred to the substrate by RIE. While using the photoresist could be tedious, Heather et. al [52] irradiated a borosilicate glass with modulated laser beam. The area that under intense laser irradiation was selectively etched to create micro-optical elements on the glass substrate.

1.2.4 Laser direct heating and forming

The other method of forming microlens array is the direct forming by laser irradiation on the glass substrate [53-57]. The advantage of this method is the elimination of complex lithography process, which is time consuming and costly.

Using CO_2 or Argon lasers, the adsorption of the laser beam energy causes the locally heating of the glass substrate, which leads to the melting of the material. Owing to the surface tension of the melted material, a spherical or elliptical micro lens is formed. By proper control of the laser beam exposure parameters, one can control the dimension of the micro-lenses. The drawback of this method is the limitation of types of glass materials that can be used for fabrication process. Only borosilicate glass doped with semiconductor material is suitable by this method. The other problem faced in this technique is that the heat transfer to the adjacent area could affect the formation of subsequent lenses.

1.2.5 Photothermal technique

The microlens array is fabricated on a photosensitive glass by photolithography process [58-60]. The photosensitive glass substrate is exposed through a chromium mask using a UV light source and followed by the heating of the substrate (photothermal cycle). The area whereby is under UV exposure produces color due to the absorption of the metal colloids inside the photosensitive glass and induced crystalline phase in this exposed area. Therefore, the exposed area densifies, creating stress surrounding the unexposed areas and pushing them up. This creates a spherical shape if the unexposed area is in circular shape, thus forming a microlens.

1.2.6 Hybrid materials

There are more efforts to develop microlens array fabrication techniques on some novel materials. One of the common special materials is the hybrid sol-gel material, which consists of mixture of organic and inorganic compounds, such as SiO_2, TiO_2 and ZrO_2 [61-65]. Besides that siloxane film [66] is also used to fabricate microlens array. The fabrication process is based on the lithography exposure to form the lens arrays pattern or the replication using a soft mould. The lithography can be carried out by laser direct writing with the precise control of the exposure dosage. The need of etching process is eliminated as the development of these materials forms the microlens array structures. Even though the processing is not as complicated as the resist reflow technique, the preparation of these novel materials is costly and complex.

1.2.7 Microjet printing

Microjet printing uses a piezoelectronic actuator to eject droplets of UV curable polymer onto a substrate surface [67-69]. The printer head has an orifice diameter in a few tenth of micron placed at a few mm away from the substrate surface. The UV curable material is heated up before it is ejected. The microlenses shape is highly dependent on the orifice size, the UV material’s viscosity and operating temperature. The most commonly used UV curable material is UV curing optical epoxies because of its excellent chemical and thermal stability [69].

1.2.8 Replication technology

Another microlens array fabrication method is to use a replication mold or insert to transfer the lens patterns through molding or hot embossing process [70-77]. This replication technique requires the making of a PDMS or silicon mold by lithography and isotropic etching. This mold serves as a template for the actual microlens array fabrication whereby molten glass or plastic material is injected into the master mold to replicate the dimension of the mold. The advantage of this technique is that it enables repeatable and mass production of the microlens array. However, the material shrinkage during cooling causes the dimensional change and thus affects the microlens dimensional accuracy.

1.2.9 Other fabrication techniques

The microlens array fabrication technique is not limited to those mentioned above. Fu et al. [78] introduced the fabrication of diffractive and refractive microlens array by focused ion beam milling and deposition of SiO_2. Replacing the conventional photolithography process with LIGA process, Ruther et. al [79] demonstrated the fabrication of spherical microlens arrays by melting the PMMA resist pillars after the development. Chan et. al [80] fabricated microlens arrays by controlling the wrinkle formation of an UV ozone oxidized PDMS material. This method allows control of the microlens' geometrical shape and arrangement.

In general, the fabrication of microlens arrays requires the ability to produce microlens arrays that can meet the requirements of a specific system or device. The demand of compactness and small size for most of the electronic appliances has lead to the rapid development of precision engineering and nanotechnology in microlens array fabrication techniques.

1.3 Objectives and motivation

The main objective of this research project is to study the feasibility of fabricating various types of microlens arrays by the combination of laser assisted patterning method and etching process. There are several issues concerned in the mass production of the microlens array such as the production of a template and the design flexibility. In conventional photolithographic and gray tone mask techniques of the microlens array formation, the requirement of photomask becomes essential and critical [46]. The making of these photomasks is costly and time-consuming. Meanwhile, as the microlens shape is determined by mask design, any changes of the microlens array layout require the alternation of mask design as well.

Therefore, it is important to develop a microlens array fabrication process that eliminates the needs of expensive photomasks, while at the same time gives the flexibility to design changes as well as controlls the lenses dimension. In this case, the maskless laser direct patterning is a good candidate for fabricating micro structures, such as microlens arrays. The patterns are formed directly by either laser ablation or interference of laser beams without the need of photomask. The fabricated microlens array is measured and tested on their physical and optical properties.

Besides the fabrication techniques, this study also investigates the potential applications of the microlens array in surface nanopatterning by pulsed laser irradiation. The significance of the microlens array to precision engineering applications has motivated the research interest of this project to further explore the future potential applications, such as in bio-engineering and nanotechnology. For example, the requirement of higher volume density of data storage has driven the development of surface nano-structuring and nano-patterning.

The studies discussed previously on the applications of the microlens array show that the use of the microlens array can be a potential candidate in surface nanopatterning. The studies by Wu et. al [34-36] revealed the possibility of nanopatterning using microlens arrays but it was limited to normal light, which is diffraction limited. Lin et. al [38] and Kato et. al [37] demonstrated the use of femtosecond laser as light sources. The nanopatterning was not done on photoresist, which is one of the most common and widely used photopolymer materials in semiconductor manufacturing.

Furthermore, the previously mentioned studies concentrated more on the methodology but not the characterization and simulation of the optical behaviors of the microlens array. The emphasis of this study is to carry out nanolithography on photopolymer materials, such as photoresist by the laser light irradiation through the microlens array. A significant challenge will be the large scale patterning and the mechanism of patterning process. Thus, it is believed that with microlens array at small lens size, this task can be accomplished while lots of studies need to be carried out to understand the underlying physical mechanisms.

The use of fabricated microlens arrays for surface nanopatterning could provide a more versatile platform to create large area sub-micron features at a high speed as compared to other patterning methods. There is still room for improvement, such as the control of sizes of the microlenses and the alignment precision of the microlens. Therefore, extensive researches on the fabrication technique of the microlens array and its applications in surface nanopatterning are needed.

1.4 Organization of the thesis

The contents of the remaining chapters in this thesis include the following:

Chapter 2 presents the fabrication technique of the concave microlens array by the laser direct patterning and isotropic etching. The experiemental setup and characterization methods will be discussed. Mechanism of the concave microlens array formation will be presented as well.

Chapter 3 will discuss the fabrication process of the convex microlens arrays by laser interference lithography (LIL) followed by resist reflow and reactive ion etching. The process parameters of thermal reflow and its effects on the microlens array formation are presented. The fabricated microlens array is characterized for its physical and optical properties.

Chapter 4 presents the theoretical and simulation studies of optical behaviors of the microlens array under a laser irradiation. Models and mathematical expressions used in the simulation are presented. The finite difference time domain (FDTD) simulation is applied to calculate the intensity and energy flux distribution of the focused laser beams.

Chapter 5 describes the surface nanopatterning technique by irradiating a laser beam through a microlens array. The physical processes and experimental details are revealed in this chapter. Results of nano-features generation will be investigated and it potential applications is discussed.

Chapter 6 concludes the research results on the microlens array fabrication techniques and its applications for surface nanopatterning. The possible future works are also proposed.

CHAPTER 2

MICROLENS ARRAYS BY LASER DIRECT PATTERNING AND ISOTROPIC ETCHING

2.1 Overview of Laser Ablation

Laser ablation is a process that involves the removal of a material by laser irradiation on a substrate surface. The ablation process can be performed by a continuous wave (CW) or a pulsed laser [81] as long as the energy supplied to the material is sufficient. Ablation takes place when the irradiated laser fluence, F, is above the laser ablation threshold, F_{th} of the material [82]. Pulsed laser is a more preferred source of laser for ablation because it has a high intense peak power as compared to a CW laser. When the laser irradiates on the substrate surface, the material is first heated up due to the absorption of the laser energy by the material under the laser irradiation. The heating of the material then causes the material to melt and eventually evaporate or vaporization takes place. The total amount of material ablated away is dependent on laser fluence, number of pulses and material properties.

Laser ablation has been proven to be one of the useful tools for microprocessing of various materials for device fabrication, such as laser cutting, drilling, marking and welding [83-90]. The non-contact mode and versatility of laser ablation process make it a preferred microfabrication tool over other conventional tool-based methods.

2.1.1 Direct patterning by laser ablation

In the fabrication of electronic circuits, pulsed lasers with pulse width, τ in the range of typically 15 ~ 100 nanoseconds (ns) are used to cut the thin films [91-93] or to ablate surface of a solid material [94]. These lasers give minimal thermal damage to the films and adjacent irradiated areas. Nd:YAG, CO_2 and excimer lasers are among the pulsed lasers that are widely used in surface direct patterning [95]. Direct patterning on a sample surface can be done through various methods. Using excimer laser, a mask image is projected onto a substrate surface by a lens. The area under the laser irradiation is ablated away due to the high output energy of the excimer laser. By stepping the mask with respect to the substrate, a large area processing is achieved [96]. However, this mask projection direct patterning technique has its disadvantages of toxic laser gases, high maintenance/setup cost and the need of expensive mask [97] which limits its applications.

Another laser direct patterning method is by focusing a laser beam into a small spot and irradiate onto the substrate surface. The laser spot is "scanned" across the substrate surface either by moving the substrate on motion controlled X-Y-Z stage or by scanning the laser beam using a set of galvanometer driven mirrors. The patterns formed on the substrate surface can be designed by computer-aided-design (CAD) software or by directly generating the numerical code from an imported image file. This "scanning spot" method uses high repetition rate lasers, such as diode pump solid state (DPSS) Nd:YAG lasers, as the laser source. Since the laser beam is focused into a small spot, a relatively good lateral resolution can be achieved as compared to the mask projection method. Meanwhile, it also eliminates the use of mask for pattern generation [98].

2.2 Mechanism of etching

Etching is a material removal process by chemical reaction or ion bombardment to the substrate surface, [99] which is widely used in semiconductor manufacturing. Etching is usually applied to transfer patterns defined by a masking layer to the thin film coated on the substrate or bulk material's surface. The etching process can be classified into 2 categories: anisotropic and isotropic etching [100,101]. In the etching process, two types of etching profile can be obtained, depending on the types of etchants used, and the environment of etching whether it is in liquid phase (wet etching) or in gaseous phase (dry etching) [102]. Figure 2.1 illustrates the different profiles obtained by isotropic and anisotropic etching.

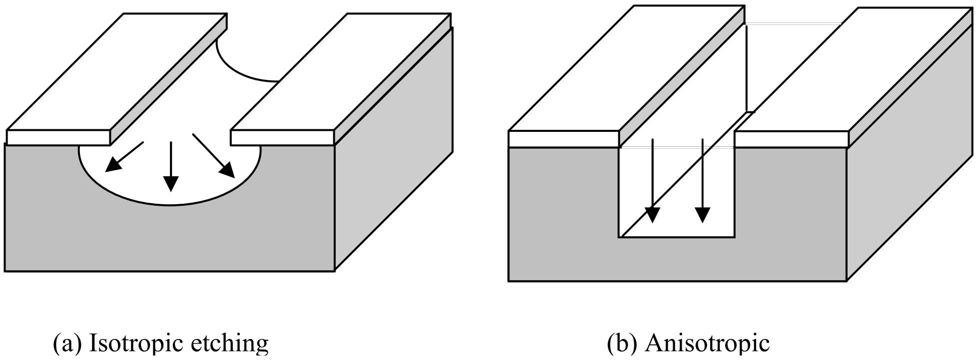
(a) Isotropic etching

(b) Anisotropic

FIG 2.1 Two types of etching profiles: (a) isotropic etching and (b) anisotropic etching.

2.2.1 Anisotropic etching

For the anisotropic etching, the etching rate is higher at a particular direction than those at other directions. Therefore, a straight side wall profile at the etched pattern can be easily achieved. Most of the dry etching is anisotropic etching, while for wet etching, anisotropic can only be achieved with certain materials, such as silicon.

Examples of anisotropic etching processes are plasma etching, reactive ion etching (RIE) and hydroxide etching of silicon [103], etc.

2.2.2 Isotropic etching

Isotropic etching is another type of etching process, which the etch rate of the horizontal direction is equal to the etch rate of vertical direction. The isotropic etching involves three major steps. Firstly the mass transport of reactants or etchants to the substrate surface, followed by chemical reactions with the substrate material at the surface interface and finally by-products transported out from the surface. As compared to anisotropic etching, which is ion assisted and has a low etch selectivity, isotropic etching involves chemical reaction between etchant and substrate interface. The etchant dissolves away the substrate materials when the free ions from the etchant are in contact with substrate surface. Since it is a chemical reaction, isotropic etching has high selectivity thus a relatively thin masking film is sufficient to protect the substrate from being etch away.

The isotropic nature of SiO_2 etching enables one to smoothen glass for various applications [104,105]. The experiment carried out utilizes the concept of isotropic etching to create the concave lens arrays on the glass substrate. The reaction involved between etchant (HF acid) and substrate (SiO_2) is given as Eq. 2.1:

$$SiO_2 + 6HF \rightarrow H_2 + SiF_6 + 2H_2O \tag{2.1}$$

The reactant (HF) diffuses into SiO_2 surface, is adsorbed by SiO_2 and chemical reactions take place [106,107]. The free fluorine ions combine with silicon ions, which generate SiF_6 molecule products and subsequently the products diffuse away from the substrate surface. Therefore, the etch rate of the SiO_2 at certain temperature depends on the amount of free ions of fluorine in the solution. By alternating the F^- concentrations in the etchant solutions, a different etch rate can be achieved.

$$HF \rightarrow H^+ + F^- \tag{2.2}$$

The control of the F^- concentration can be done in two ways, one is to dilute the 49% concentrated HF (by weight) with DI water based on the theory of conservation of mass as Eq. 2.3:

$$M_1 c_1 = M_2 c_2 \tag{2.3}$$

where M represents the molarirty by weight
and c represents the weight of the solution

The other method to controll the concentration of F^- includes the buffering of original HF solution by the addition of ammonium fluoride, NH_4F. The advantage of using buffered HF is the etching mechanism is not as aggressive as diluted HF, thus giving better controllability of etching process. The etching chemical reaction involving buffering of HF acid is given by Eq. 2.4.

$$\begin{gathered} SiO_2 + 4HF + 2NH_4F \rightarrow (NH_4)2SiF_6 + 2H_2O \\ SiO_2 + 3HF_2^- + H^+ \rightarrow SiF_6^{2+} + 2H_2O \end{gathered} \tag{2.4}$$

2.3 Experimental procedure

2.3.1 Sample preparation

The material used in this experiment was soda lime glass slide with dimension of 1.5 cm × 1 cm. The samples were cleaned in ultrasonic bath using Iso-propanol (IPA) and De-ionized water (DI water) to remove any contaminations. This is important for the improvement of film stiction on the substrate's surface. The cleaned substrates were then placed inside a vacuum chamber and coated with 200 nm of gold film by an E-beam evaporator.

2.3.2 Experimental setup

Figure 2.2 shows the experimental setup for the patterning process. The system includes laser source, laser beam delivery setup and XYZ motion control system. The laser used was a 3rd harmonic Nd:YAG laser with light wavelength λ of 355 nm. The repetition rate of laser was set at 1 kHz while patterning was done with various laser fluneces (mJ/cm^2). The laser beam from the source output was directed to the XY translation stage with a series of reflective mirrors. A laser spot size of 3 ~ 5 μm can be achieved by focusing the laser beam through a near-UV objective lens with 50X magnification and focal length of 4 mm. To obtain focal point on the film surface, the Z height of the objective lens was adjusted accordingly.

The design of the laser patterning tool path and pattern dimension was done by MasterCAM software. Subsequently, it was translated into NC codes to be executed by the XYZ motion controller. Circular lens patterns with diameters of 100, 50 and 20 μm were designed with hexagonal arrangement. The patterned substrates were then cleaned with IPA and dried with nitrogen gas blowing.

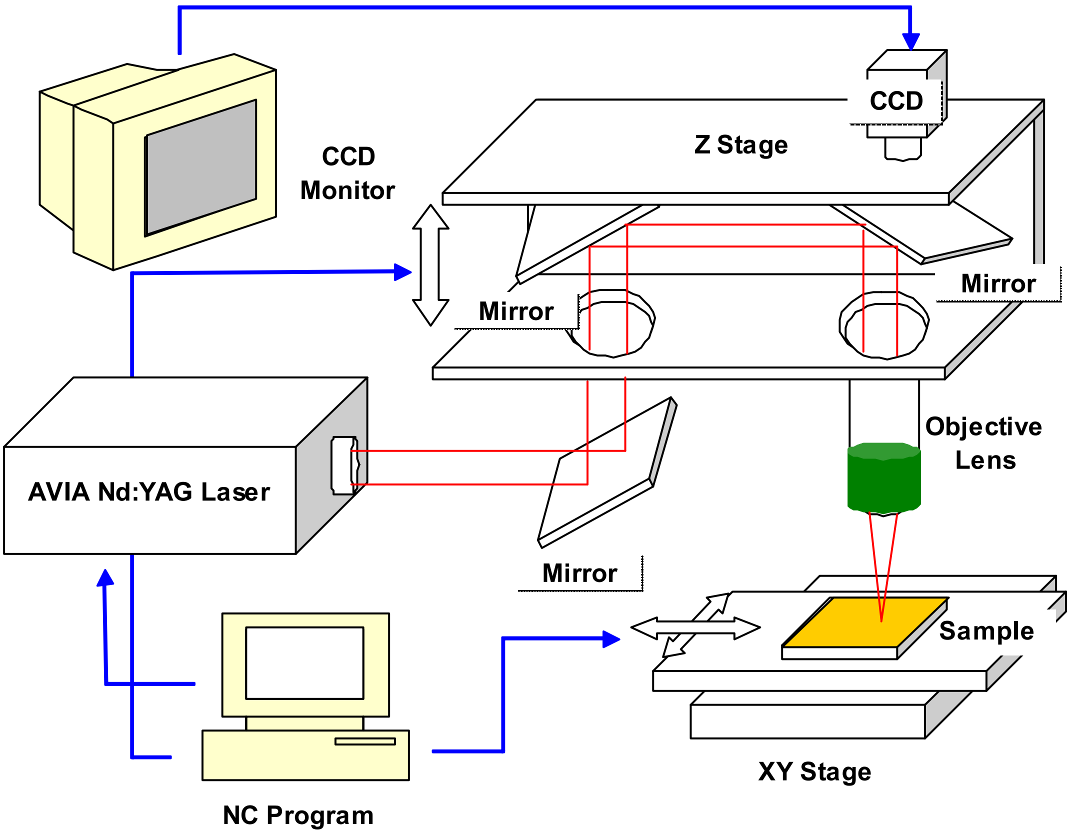

FIG 2.2 Schematic drawing of the laser system setup for laser patterning of gold film.

Figure 2.3 shows the schematic drawing of the etching process carried out after the laser patterning. The sample was dipped and etched in an etchant solution that contained in a PVC beaker for a period of time. The etchant used in this experiment was hydrofluoric acid (HF) which was commonly used for etching of glass material (SiO_2). Two types of HF etchants were used in this experiment – diluted HF and buffered HF. Diluted HF was prepared by mixing 49% concentrated HF with DI water while buffered HF contained mixtures of HF and ammonium fluoride (NH_3F) [108]. Various concentration of diluted HF of 40%, 35%, 30% and 25 as well as NH_3F:HF ratio of 5:1, 6:1 and 7:1 were prepared.

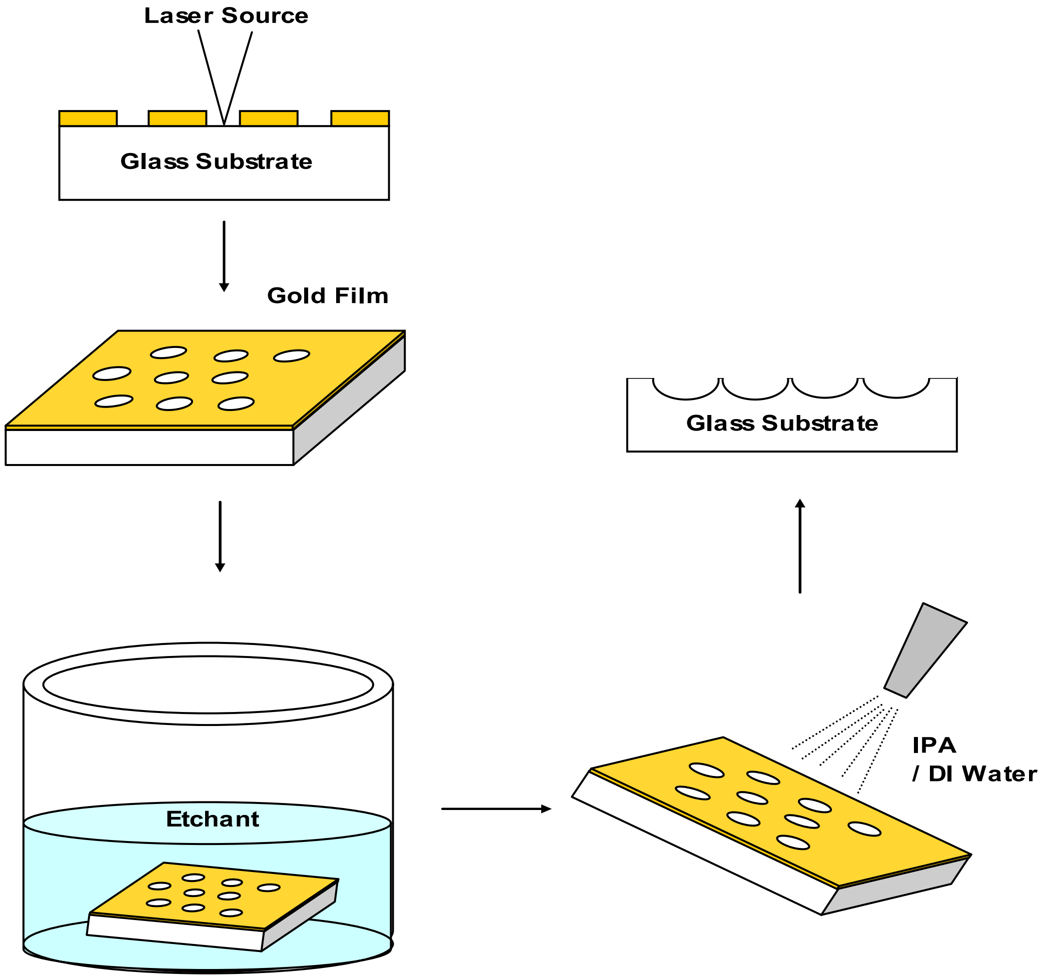

FIG. 2.3 Schematic drawing of etching process flow for the fabrication of concave microlens array.

The etched samples were then taken out from the beaker and gold masking film was stripped away before they were cleaned using IPA and DI water. The sequence of cleaning the samples were IPA rinse, IPA ultrasonic bath for 15 minutes, rinsed with DI water and finally DI water ultrasonic bath for another 15 minutes. This is important for complete chemical residual removal as well as debris contamination.

2.3.3 Characterization methods

Various methods were used to characterize the concave microlens array formed on the glass substrate. The most commonly used was optical microscope with high magnification objective lens to observe the integrity of the patterns before and after etching. It was also used to measure the dimension of the lens diameters. For surface morphology, scanning electron microscopy (SEM) was used to examine the quality of the lens surfaces after etching. The profile of the etched patterns was captured using Alpha-Step 500 surface profiler (Tencor Instrument) with vertical resolution of 1Å for 100 µm & 50 µm diameters lens. For 20 µm diameter lens, AFM was used due to the limitation of the profiler's stylus to obtain good resolutions.

2.4 Patterns Formation by Laser

Figure 2.4 shows the comparison of transmission spectra between photoresist and gold thin film (thickness = 200 nm) in the range from 300 nm to 800 nm. At λ = 355 nm, it was found that about 65% of the light intensity at this wavelength is transmitted through the resist layer without being adsorbed whereas less than 5% of the light intensity is transmitted for the thin gold film. Therefore, by 3rd harmonic Nd:YAG laser, the thin gold film can be effectively ablate since most of the laser energy is absorbed by the film. Meanwhile, the thin gold film exhibits lower melting temperature at 1063˚C as compared to other novel metals, such as chromium and titanium, which ease the material removal process at a lower laser fluence.

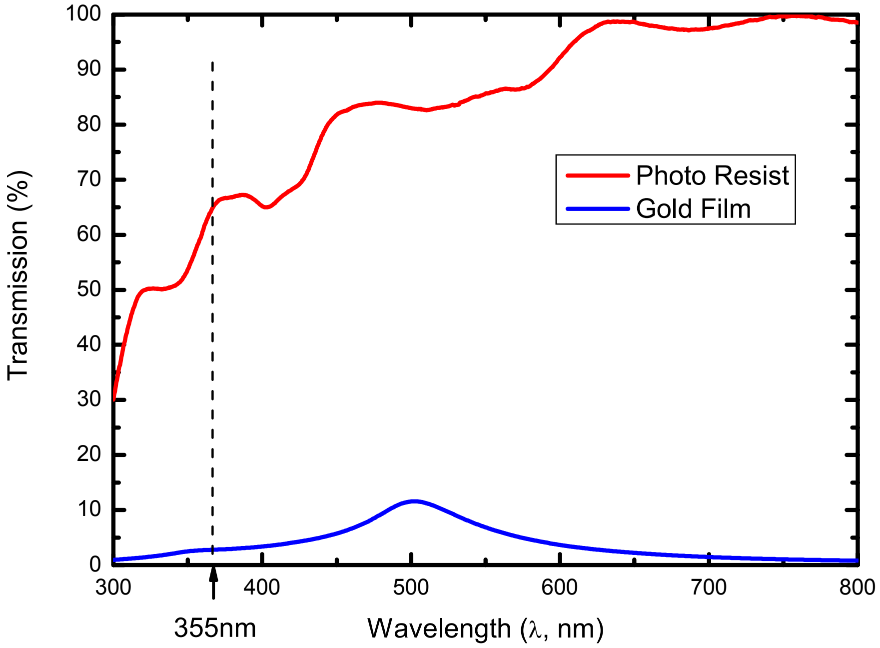

FIG. 2.4 Transmission spectra of photoresist and gold thin film (thickness = 200 nm).

Figure 2.5 shows a circular pattern arrays created by laser patterning by laser ablation. The patterning procedure was designed using MasterCAM and translated into NC codes. The tool path used in this experiment was pocket scanning whereby the ablation was done by focusing the laser beam on the thin film and followed by circular movement by the XY stage. Each complete circular motion removes the thin film on the substrate from inner ring towards outer ring with 15% overlapping until a circular pattern at a desire diameter was created. As seen from the figure, the patterned area is free from debris re-deposition while maintains a good patterning repeatability.

It can be seen from Fig. 2.5 that the arrangement of the pattern is in hexagonal shape, which gives denser lens arrays as compared to rectangular packed arrays. For hexagonally packed lens arrays, the Y pitch is equal to $2/\sqrt{3}$ of X pitch [42], thus gives more compact arrays per unit area, which is known as packing density, η (Eq. 2.5).

$$\eta = \frac{r^2 \pi}{p_x p_y} \tag{2.5}$$

where p_x is x pitch, p_y is y pitch and r is the diameter of the lens pattern

From the figure, it also shows that the patterns are uniformly and precisely distributed. This is due to the precision XY stage used and coupled with the NC-coded controller. For 100 µm and 50 µm circular lenses, the x pitch was 20 µm that results in packing density of 63.5% and 46.3%, respectively. Whereas for 20 µm circular lens, it is 10 µm, giving packing density of 40.3%.

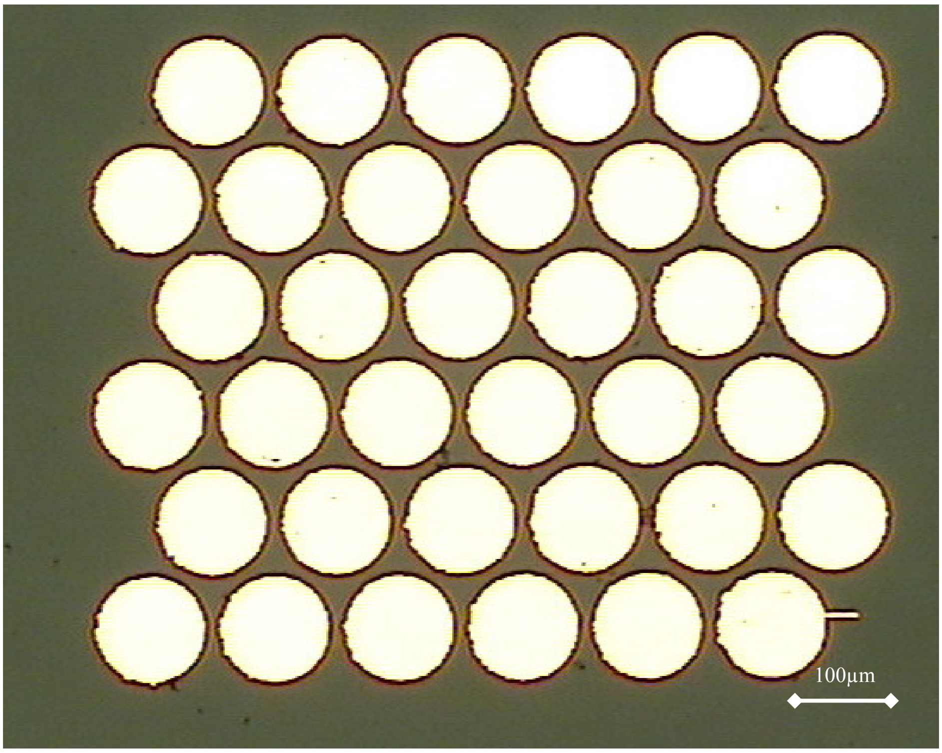

FIG. 2.5 A 6 × 6 100 µm diameter pattern arrays generated by the laser ablation.

The effect of laser fluence on the patterns quality was studied. Figure 2.6 shows the comparison of the pattern arrays created within and below the ablation condition that gives clean and complete removal of the gold film. The study was carried out by patterning the film by different laser fluences and at a repetition rate of 1 kHz. The patterned film was observed under an optical microscope to determine the optimal ablation condition. It is found that the optimal range of fluence is from 0.015 J/cm^2 to 0.045 J/cm^2. This range agrees to the findings of Andrew et al. [109] on the laser ablation of various thin film removal using 308 nm XeCl laser. In his paper, the removal threshold reported for a 500 nm gold thin film was 0.03 J/cm^2. As the fluence falls below this range, black dots were observed at the patterned area. This is due to the insufficient laser energy to fully vaporize the film material thus a small portion of the materials melt and stay at the patterned area as it re-solidifies.

On the other hand, if the laser fluence exceeds the range, the boundary of the patterned thin film is heated up and lifted from the substrate surface. This is due to the excess heat generated by laser energy around the pattern boundaries. Laser fluence of 0.017 J/cm^2 was selected for the patterning process at a scanning speed from 15 µm/s to 167 µm/s. It was also observed that at this laser fluence no damage was found on the glass substrate surface after the laser patterning. This is because the laser power is much lower than the ablation threshold for glass substrates. Therefore, the laser light transmits through the glass without any damages created.

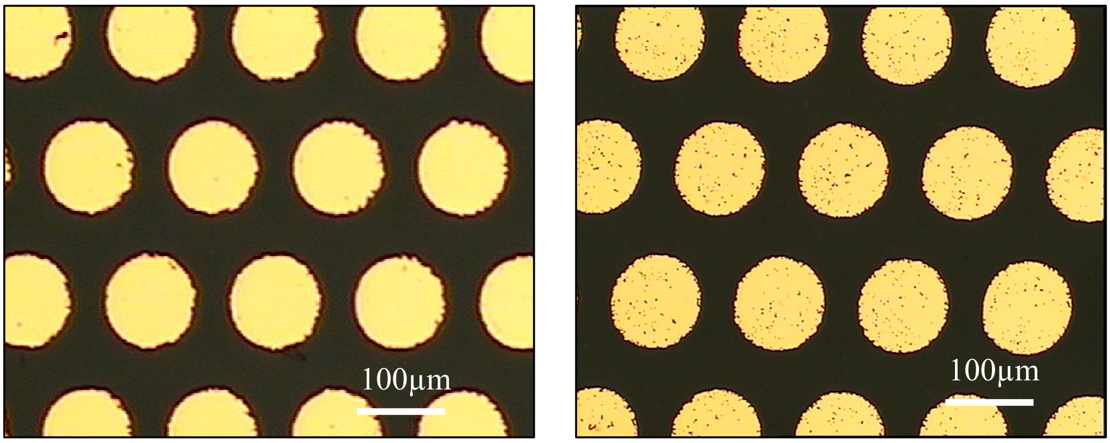

(a) (b)

FIG. 2.6 Comparison of laser ablated circular patterns arrays on the gold thin film at a laser fluence (a) above and (b) below optimal laser fluence.

2.5 Concave lens arrays formation by chemical wet etching

2.5.1 Uniformity of microlens array

Figures 2.7 (a) and 2.7 (b) show the optical images of the etched pattern arrays for 100 µm and 50 µm lens diameter using 30% diluted HF etching. It can be seen from the figures that a series of hexagonally arranged microlens array was formed on the glass substrate after the etching. These arrays resembled the patterns generated on the film which explained the purpose of the gold thin film, which acts as the masking layer. The equal etch rate in all directions for the chemical wet etching enables the exposed glass surface to react with ions F^- and removes uniformly across the whole area. Thus a hemispherical profile was formed at the exposed glass surface to create concave lenses whereas other areas were protected by the gold thin film.

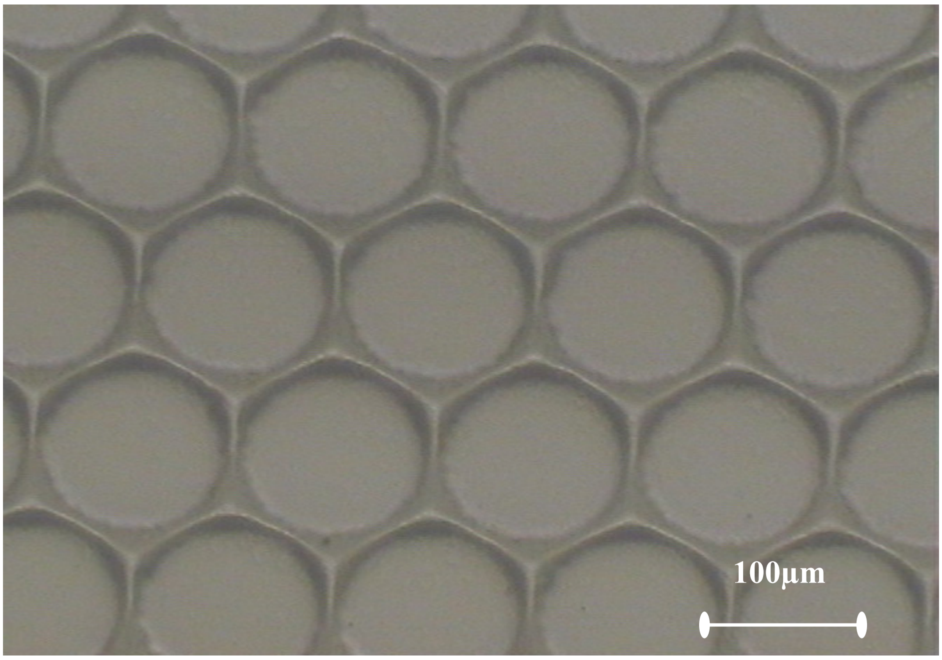

(a)

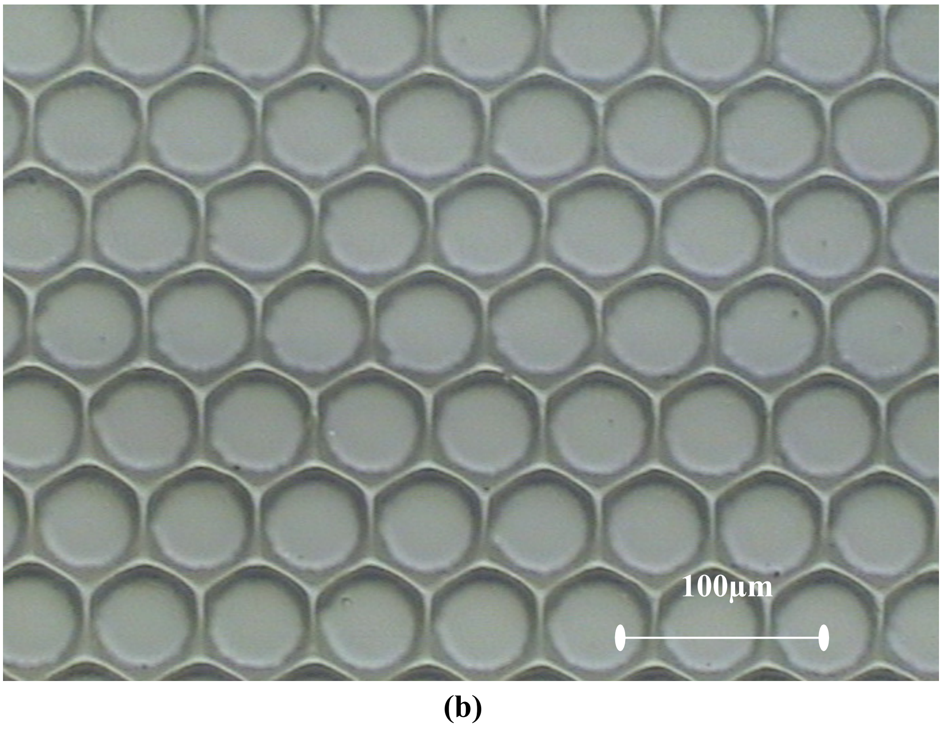

(b)

FIG. 2.7 Optical image of a (a) 100μm and (b) 50 μm microlens array formed by 30% HF etching.

Due to isotropic characteristic of the HF etching on glass, undercut was observed at the protected areas. This was more obvious at the gap between 2 lenses whereby it caused the lens diameters of the etched lenslets about 3 ~ 5 % larger than the original patterns on the film. Figure 2.8 explains the phenomenon of undercut by the isotropic etching. Measurement was taken for 20 samples for each type of lens arrays and it was found that the average diameters after the chemical etching for 100 µm, 50 µm and 20 µm microlens array patterns on the gold thin film were 105.4 µm, 50.6 µm and 20.1 µm, respectively.

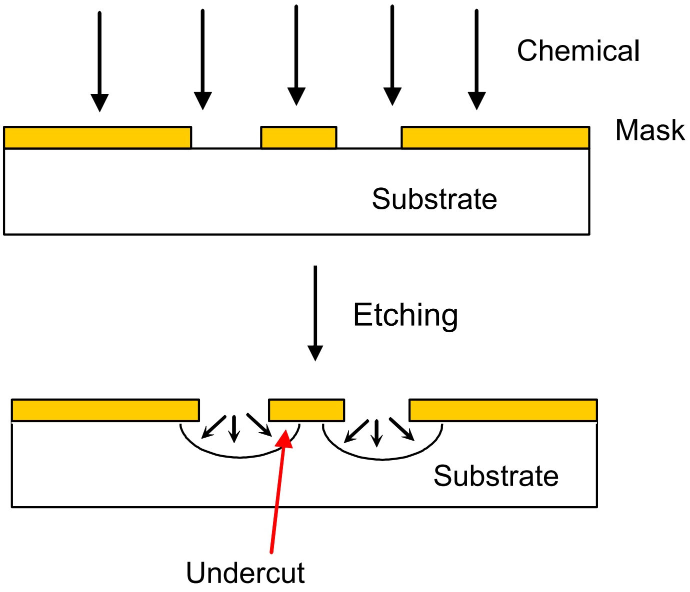

FIG. 2.8 Phenomenon of undercut in the isotropic etching.

2.5.2 Surface morphology analyses by scanning electron microscopy

The surface morphology of the microlens array was further investigated by scanning electron microscope (SEM). Figures 2.9 (a) and 2.9 (b) show the SEM images of 100 µm and 50 µm microlens array. Both images show that the most of the lens surfaces were smooth after being etched by the etchant. However, there were some defects shown at Fig. 2.9 (b). It is due to the contaminations that act as a protecting medium at the exposed area. This prevents the area from being etched and thus generates abnormality on the lens surfaces.

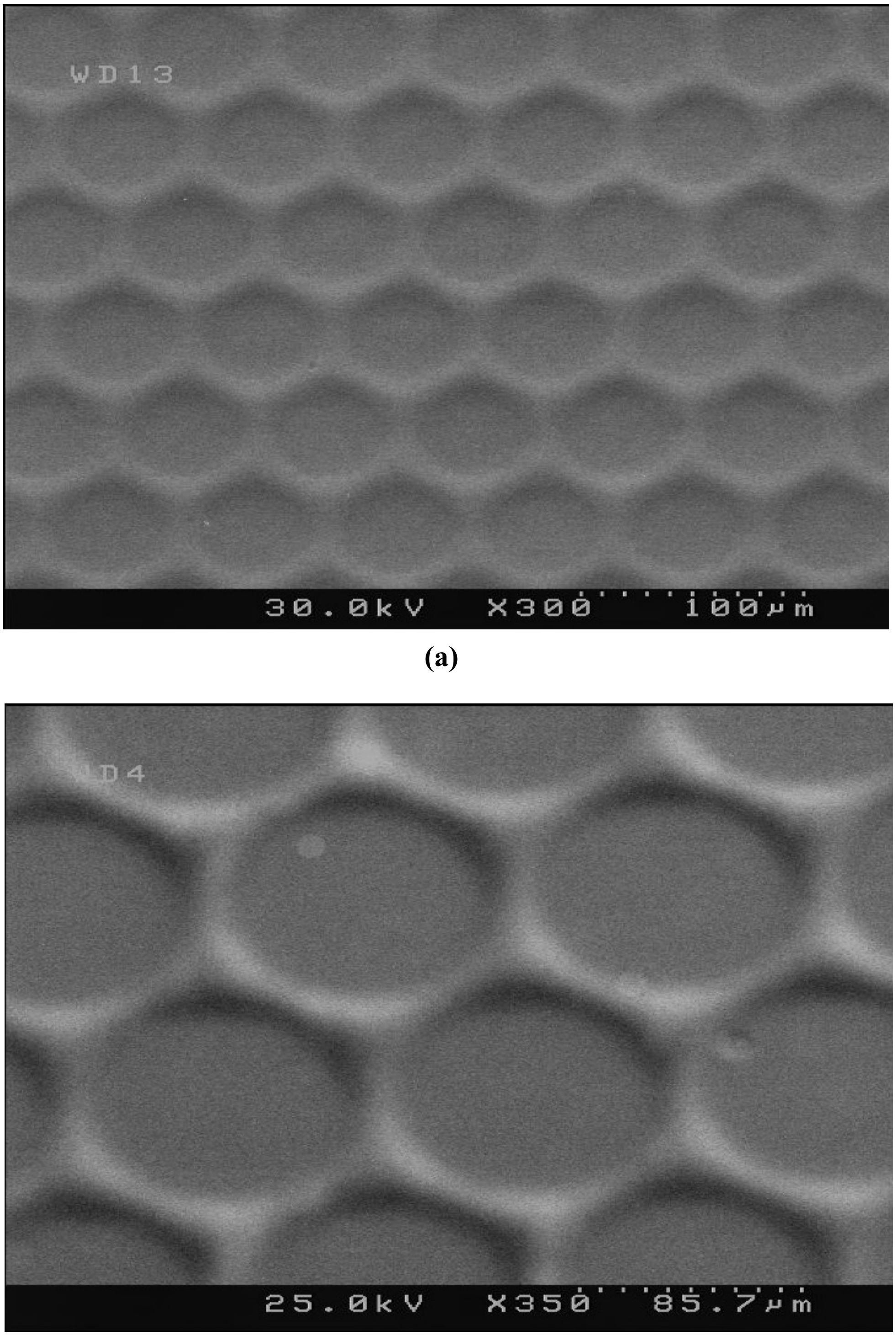

(a)

(b)

FIG. 2.9 SEM images of (a) 100 µm and (b) 50 µm microlens arrays etched by 30 % HF solution.

2.5.3 2D cross sectional profiles of microlens arays

The 2D profile of lens arrays was measured and captured by an Alpha Step surface profiler. Figure 2.10 show the 2D profile plots of a 50 µm and 100µm lens arrays. Periodic hemispherical lens profile was observed with a pitch distance of ~ 70 µm with lens sag of ~ 1.25 µm and pitch distance of ~ 110 µm with lens sag of ~ 6.5 µm for 50 µm and 100µm lens array, respectively. These hemispherical profiles show that the etching is isotropic, driven by the chemical reaction between HF and SiO_2. This agreed well with the hypothesis made earlier that the isotropic etching of a series of circular patterns formed on a glass substrate generates the concave lens arrays. Similar observation was seen on Fig. 2.11, whereby the lens array was fabricated using buffered HF. However, the sag height was much lower than that using diluted HF. This will be discussed further in the next section.

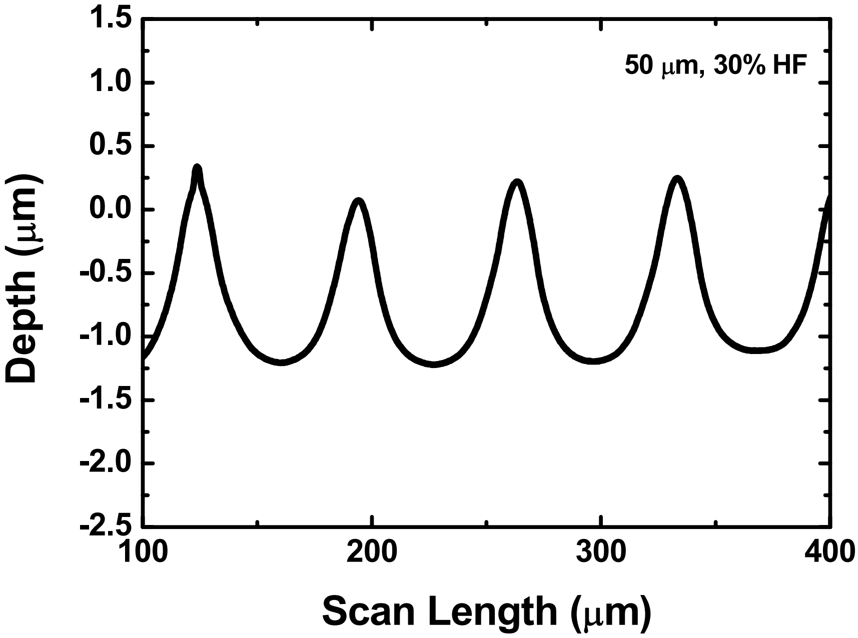

(a)

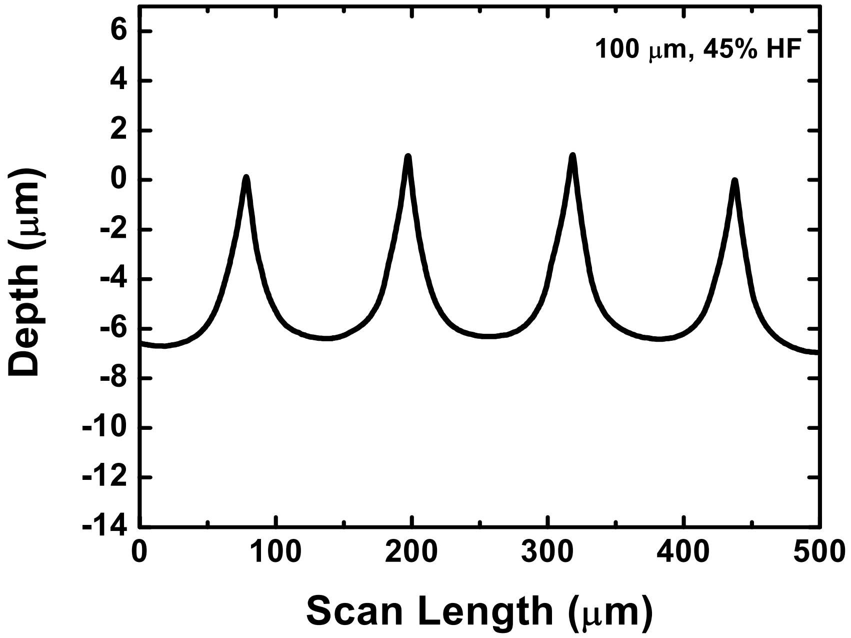

(b)

FIG. 2.10 2D cross sectional surface profile of microlens arrays fabricated by diluted HF etching for the lens diameter of (a) 50 μm, 30% and (b) 100μm, 45%, respectively.

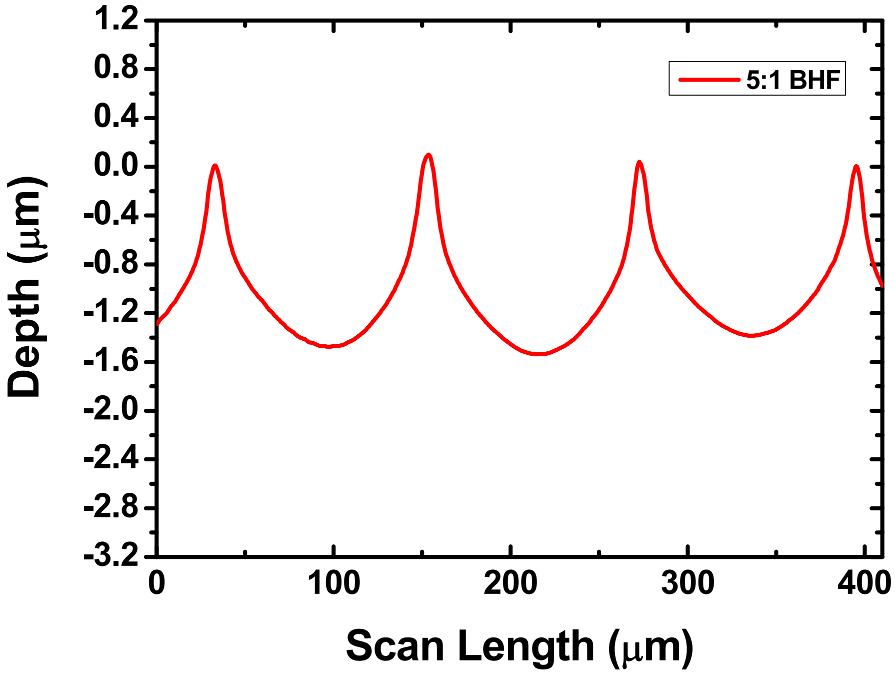

(a)

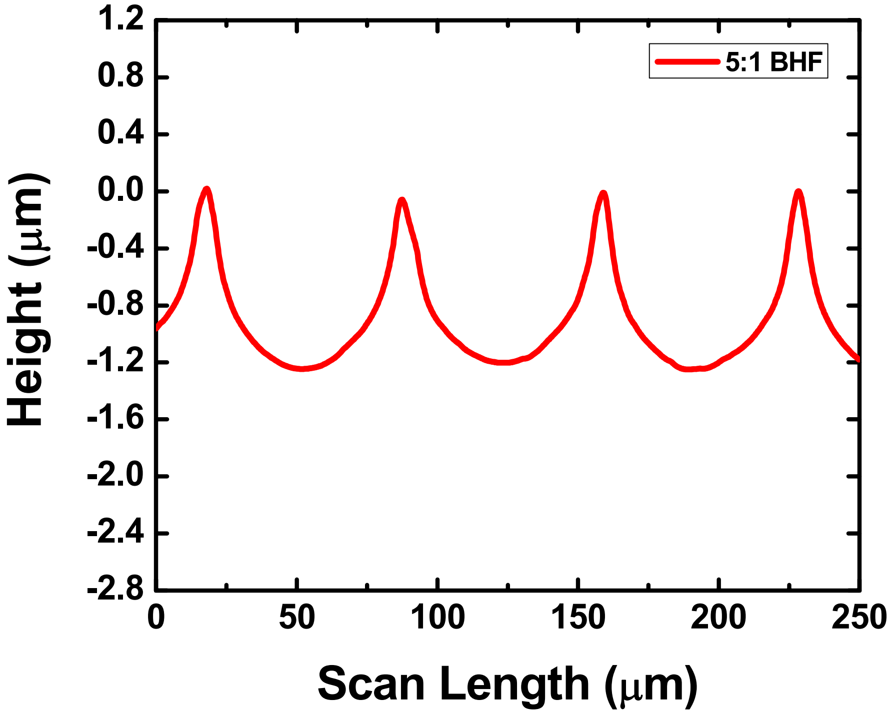

(b)

FIG. 2.11 2D cross sectional surface profile of microlens arrays fabricated by buffered HF etching at the lens diameter of (a) 100 μm, and (b) 50 μm, respectively.

2.5.4 Influence of HF concentration

To compare the effect of HF concentration, graphs of lens sag versus HF concentration were plotted for lens diameters of 50 μm and 100 μm as shown in Figs. 2.12 (a) and 2.12 (b). The increase in HF concentration will result in the increment of the lens sag obtained. On the other hand, lower HF concentrations by diluting the etchant with DI water (H_2O) give lower sag value. The reason is that the etching efficiency is highly dependant on the F^- ions concentration. Since the isotropic etching of glass is mainly a chemical reaction between two reactants, the higher ion concentration of the reactants, the faster etching rate. Therefore, as the etching rate gets faster, the lens sag obtained increases due to the more materials are being removed.

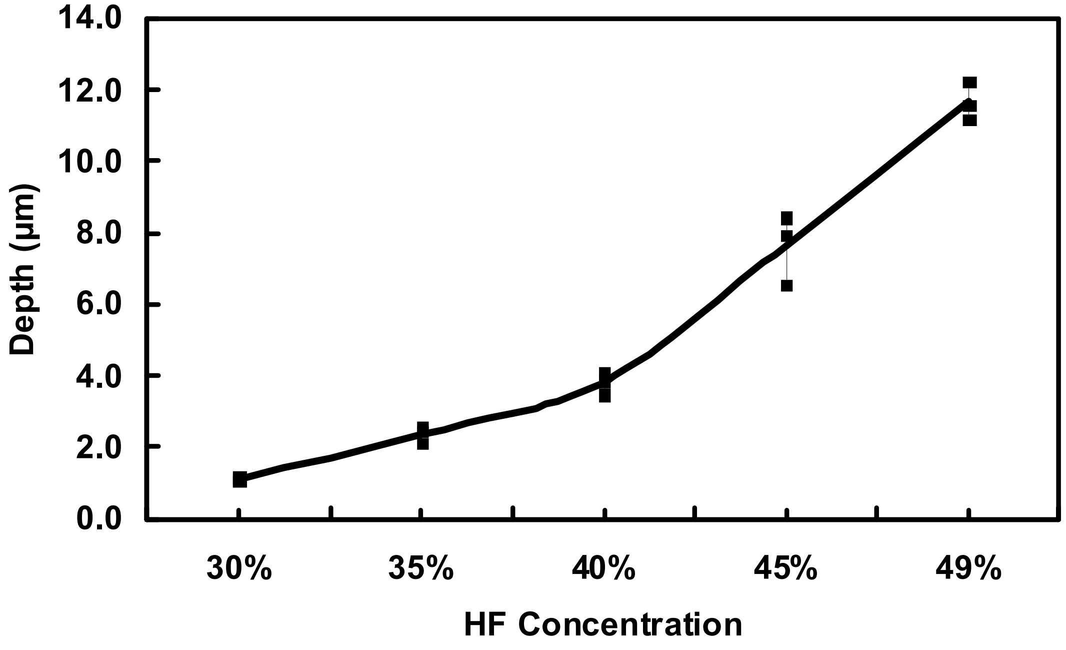

(a)

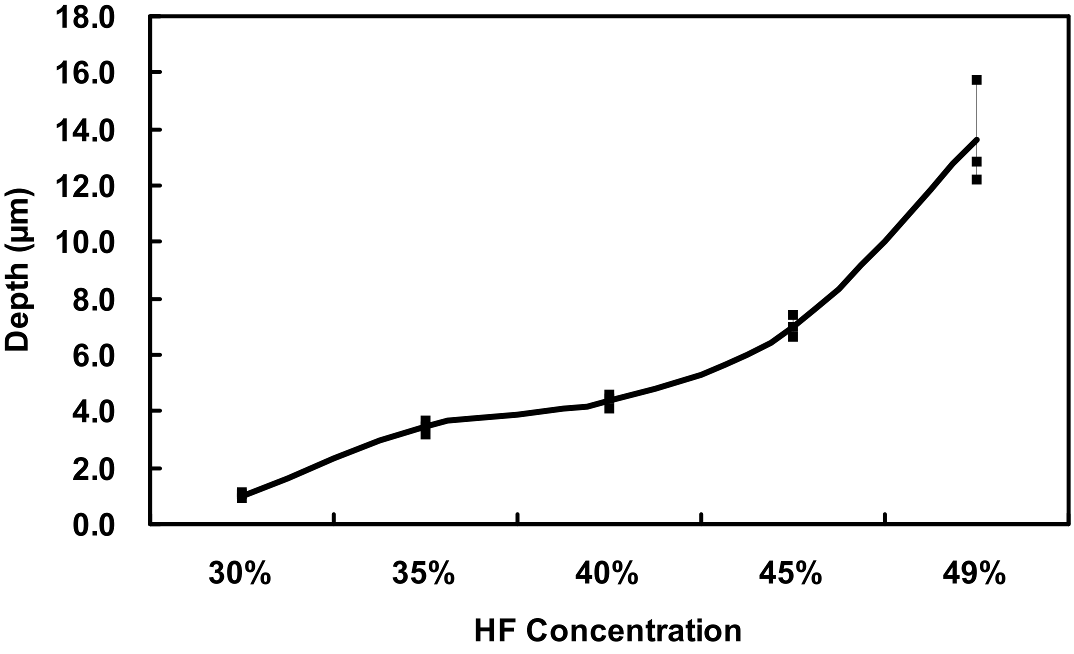

(b)

FIG. 2.12 The microlens sag value dependence on HF concentration for lens diameter of (a) 50 μm and (b) 100 μm.

Besides the diluted HF, buffered HF (BHF) was also used as an etchant. The study of different ratios of NH_3F to HF in determining the lens sag obtained was carried out in a similar way as that is being done previously on the diluted HF. Figure 2.13 shows the Alpha Step surface profiler's 2D scanned surface profile of microlens array etched at different types of BHF. An upward trend similar to the case of diluted HF is observed, whereby the higher concentration of F^- ions gives rise to the lens sag values. However, the etching of BHF was not as aggressive as diluted HF because it was stabilised by the addition of ions $NH_{3.}$ Thus to achieve a certain etching depth, diluted HF takes a shorter time than BHF.

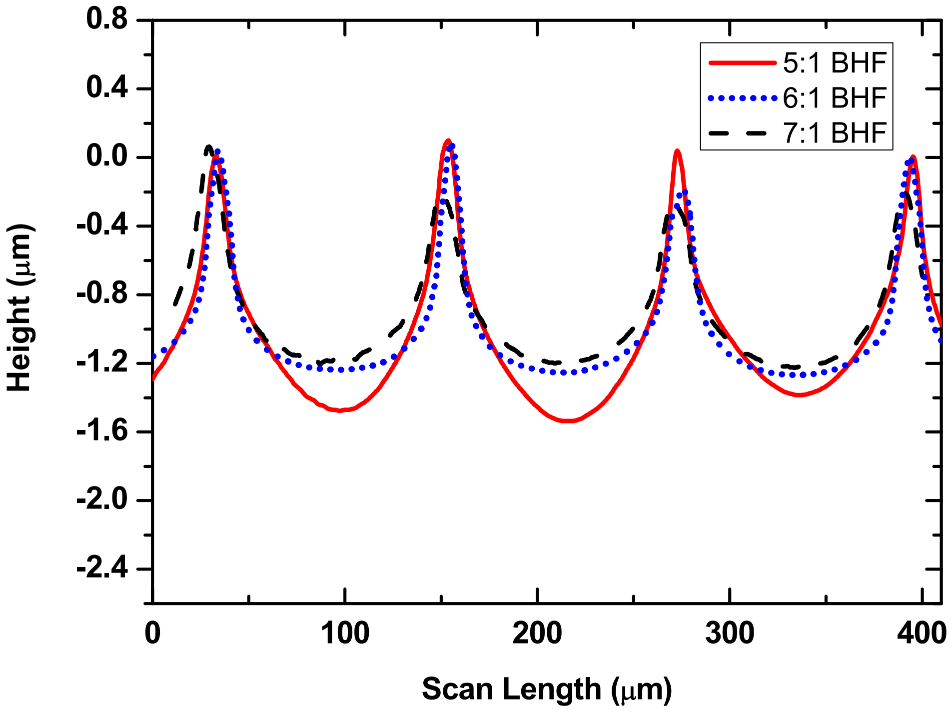

(a)

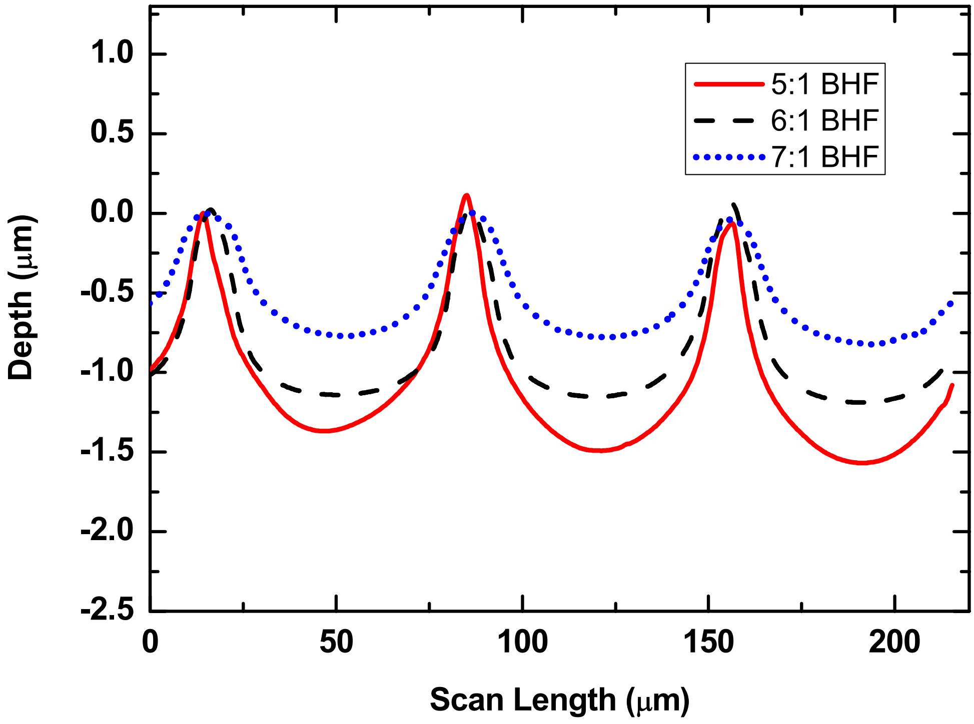

(b)

FIG. 2.13 Different lens sag values at different $NH_3F:HF$ ratios for (a) 100 µm and (b) 50 µm microlen array, respectively.

2.5.5 Three dimensional topography of microlens array

Atomic force microscope (AFM) was used as an additional measuring tool to characterise the 3D morphology of the microlens array. AFM is important to measure the profile of lens arrays with small dimension since the stylus of 2D surface profiler is not effective especially for lens diameter of 20µm. Figures 2.14 and Figure 2.15 show the AFM topography of 20 µm and 50 µm microlens arrays. The average lens sag of 20 µm lens arrays etched at same HF concentration is smaller than the obtainable sag for the other two lens diameters. This is due to the smaller area exposed for the chemical reaction, which attributes to a lower etching rate.

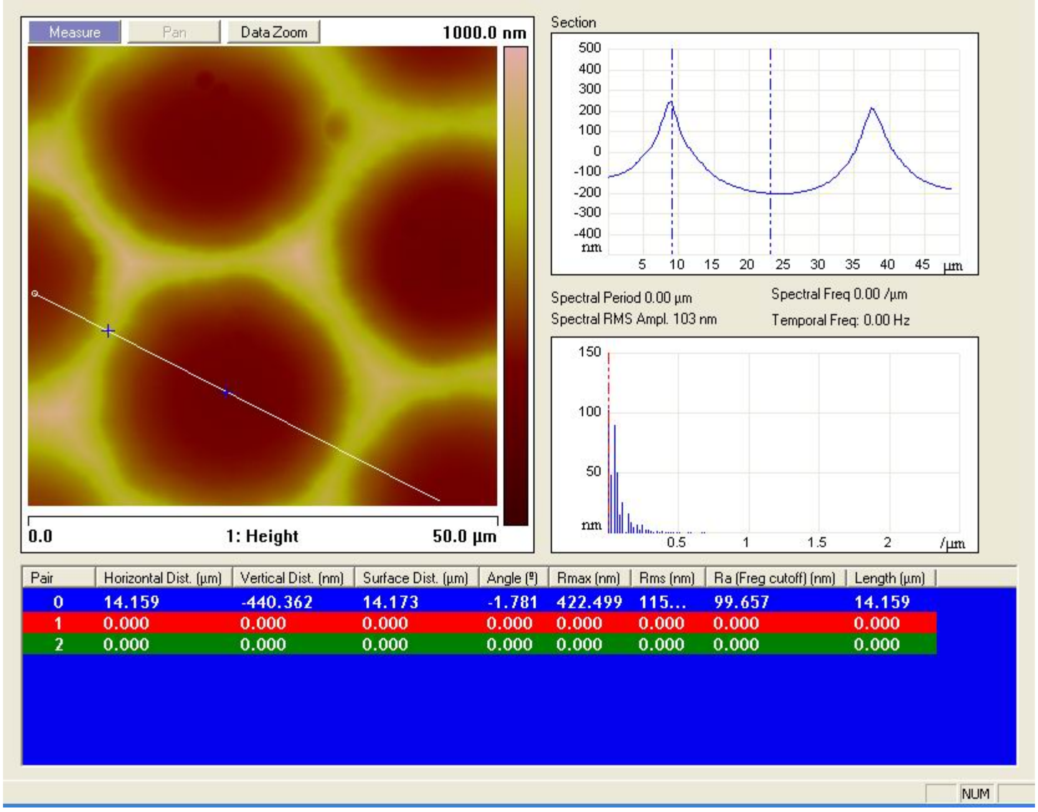

Spectral Period 0.00 µm
Spectral RMS Ampl. 103 nm
Spectral Freq 0.00 /µm
Temporal Freq: 0.00 Hz

Pair	Horizontal Dist. (µm)	Vertical Dist. (nm)	Surface Dist. (µm)	Angle (º)	Rmax (nm)	Rms (nm)	Ra (Freq cutoff) (nm)	Length (µm)
0	14.159	-440.362	14.173	-1.781	422.499	115...	99.657	14.159
1	0.000	0.000	0.000	0.000	0.000	0.000	0.000	0.000
2	0.000	0.000	0.000	0.000	0.000	0.000	0.000	0.000

(a)

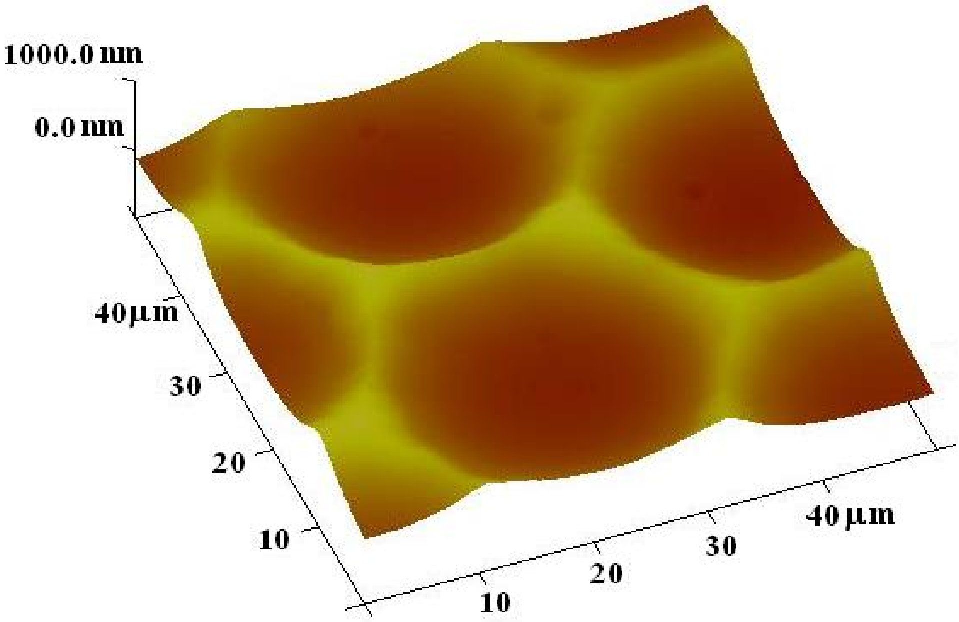

(b)

FIG. 2.14 (a) Cross section and (b) 3D views of a 20 µm microlens array measured by AFM.

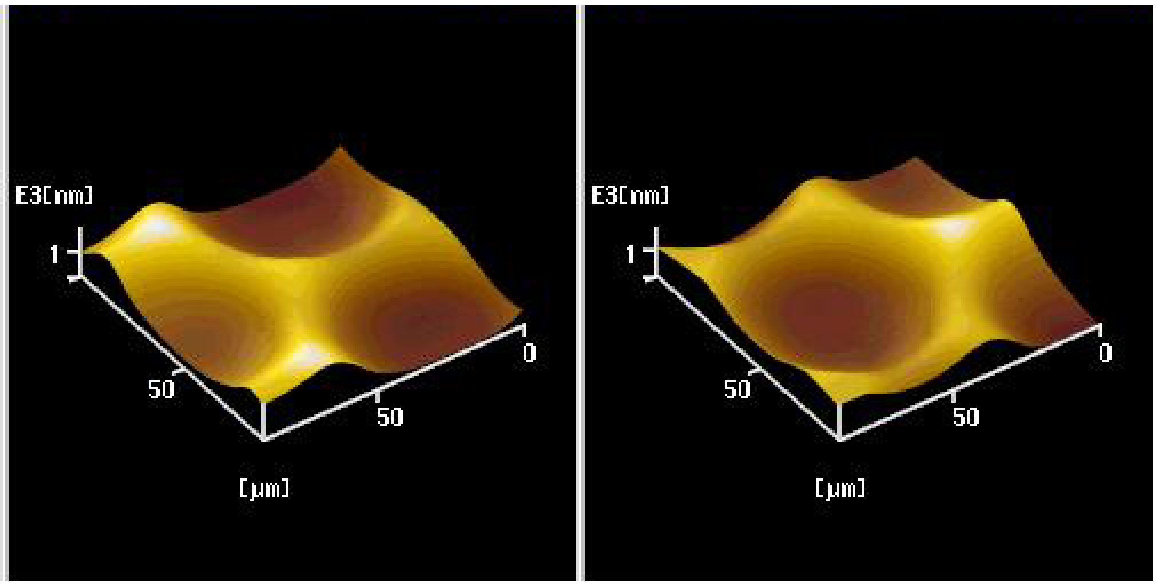

FIG. 2.15 AFM 3D images of 50 µm microlens array.

2.6 Optical Properties of Concave Microlens Arrays

The optical characteristic of the lens arrays was examined by illuminating a white light through the lens arrays and the image at the focal plane was captured. Figure 2.16 shows the images of the focused light at the focal plane, which were magnified by an objective lens and snapped by a CCD camera. From the images, it can be seen that the incident light beam was focused into a series of light dots by each individual lens. By proper adjustment of the distance from the lens surface, one can obtain different spot sizes, which eventually the smallest spot size was observed at the focal plane. This suggests that the lens arrays have several potential applications in optical beam shaping and imaging.

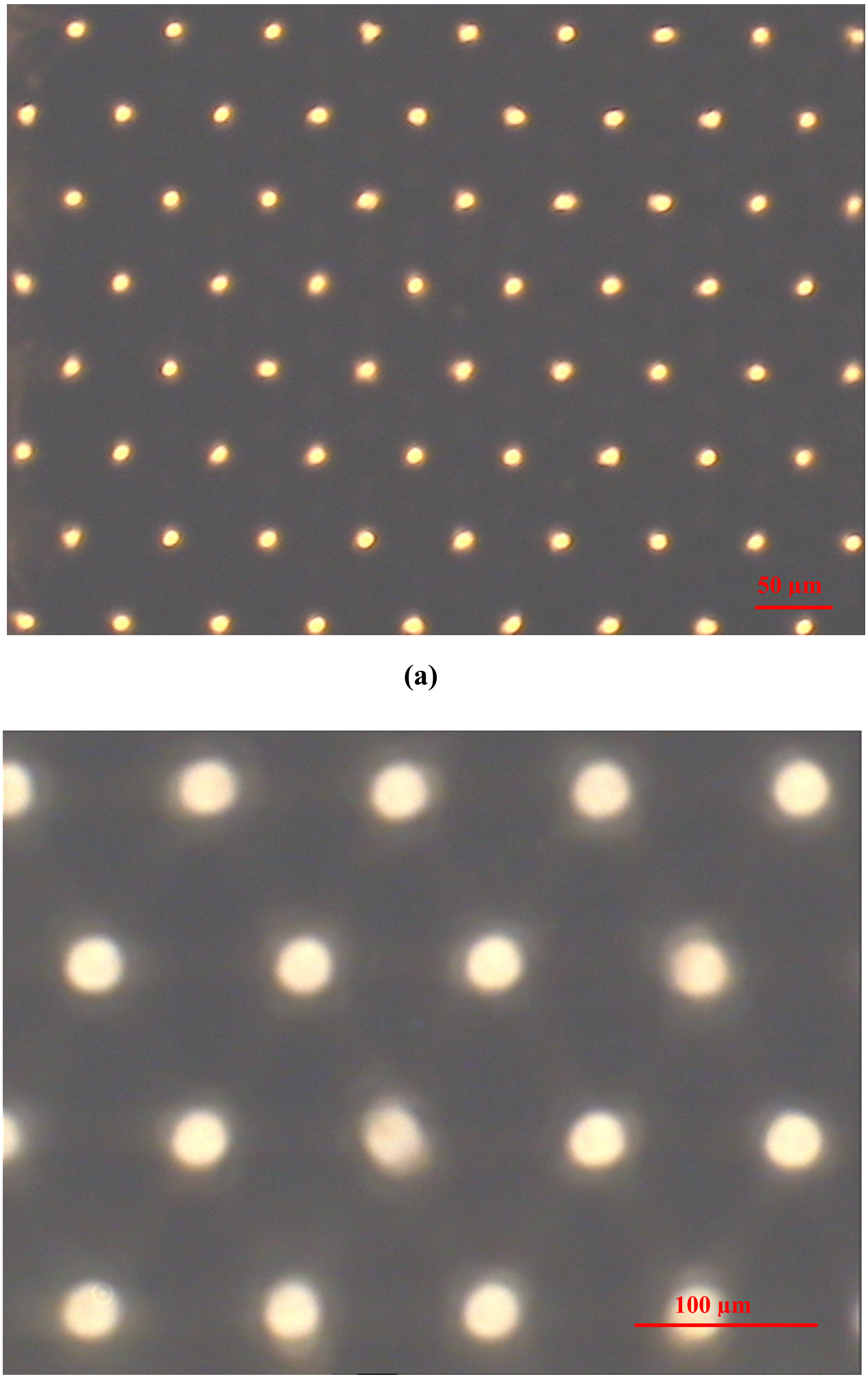

(a)

(b)

FIG. 2.16 Visual images captured at focal plane from a white light illumination for (a) 50 µm and (b) 100 µm microlens array.

The fabrication of microlens array has been demonstrated by the combination of laser direct patterning and chemical wet etching. This method provides the flexibility in designing and controlling of lens patterns by modifying the initial design and translating it into NC codes, which can be done in a few minutes. This technique also eliminates the complicated lithography process that is relying much on the photomask production.

Lens arrays of diameters 20 μm, 50 μm and 100 μm with hexagonal arrangement have been successfully fabricated. The optical and SEM images show that a smooth lens surface can be obtained. This is further confirmed with 2D cross sectional profile by the Alpha Step surface profiler for spherical profile of the lenses fabricated. Chemical etching by diluted HF is more efficient as compared to buffered HF. The maximum lens sag obtained is ~ 12.5 μm for diluted HF and ~ 1.5 μm for buffered HF. It is also found that by varying the percentage of F^- ion concentration, different lens sag values can be obtained, which suggests that possibility of controlling the lens curvature.

The present work focused on the fabrication of concave microlens arrays. In next chapter, the feasibility to fabricate convex microlens arrays and in reducing the size of the lens arrays will be explored.

CHAPTER 3

MICROLENS ARRAYS BY LASER INTERFERENCE LITHOGRAPHY AND REACTIVE ION ETCHING

3.1 Introduction

3.1.1 Principle of Laser Interference Lithography

When two monochromatic waves are superposed, the resulting intensity is the sum of two individual intensities of these two waves. It is known as the wave interference [110]. Practically, the interference of two coherent light waves generates sinusoidal varying standing wave patterns. Laser interference lithography (LIL) is a lithographic technique by using laser as a light source to record the periodic patterns onto a layer of light sensitive polymer materials, such as photoresist [111,112]. It is a maskless and simple method for patterning to fabricate periodic, quasi-periodic and spatially coherent structures over a large area [113-116]. Figure 3.1 shows a schematic illustration of the resulting fringes generated by interference of two light beams that forms a standing wave. The resulting patterns are a series of gratings with a certain period length. The factors that affect the period of the structures are the light wavelength λ and the angle of which the two light waves intersect θ as given by Eq. (3.1).

$$\text{Standing wave period } \mathrm{P} = \frac{\lambda}{2\sin(\theta)} \tag{3.1}$$

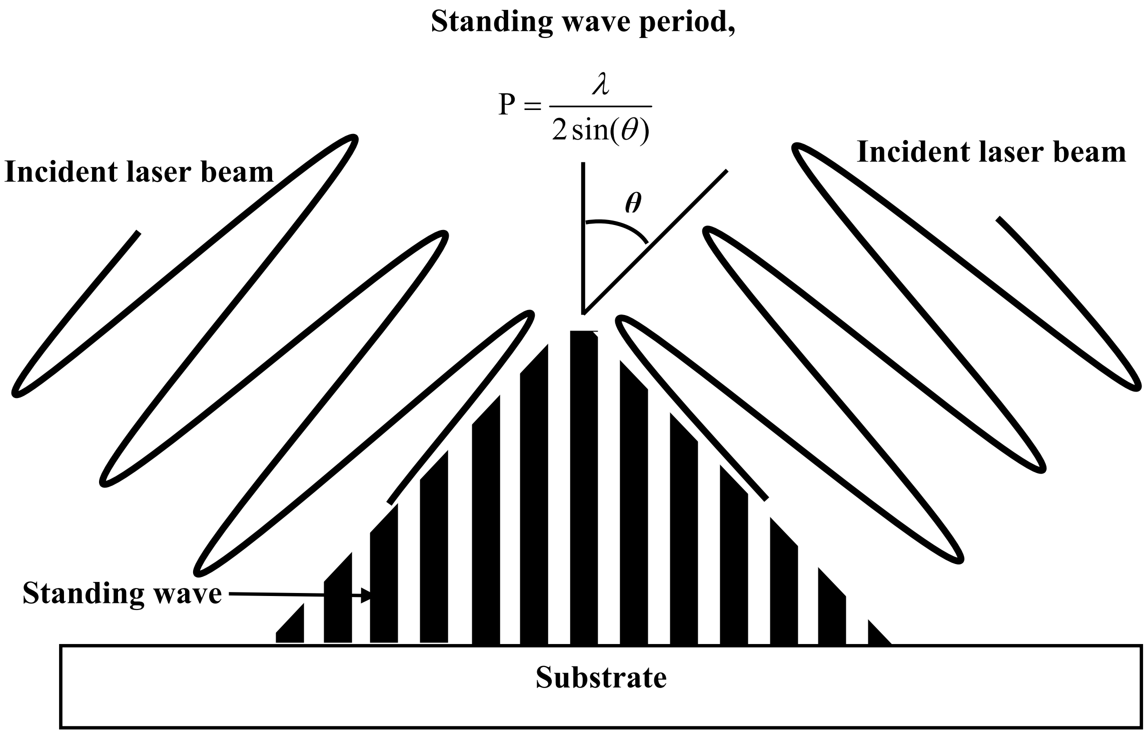

FIG. 3.1 Schematic drawing of a standing wave generated by interference of two laser beams.

3.1.2 Lloyd's Mirror Setup

There are several different setups for the laser interference lithography and each setup has its own advantages and disadvantages. Figure 3.2 shows the schematic drawing of a simple setup for laser interference lithography by Lloyd's mirror configuration. A laser beam from a laser source is directed to a spatial filter by a set of mirrors. The spatial filter consists of an objective lens and a pinhole with its diameter approximately equal or larger than the focused laser beam size. The function of the spatial filter is to filter out the high frequency noise so that a uniform Gaussian beam profile can be obtained. Meanwhile, it also acts as a beam expander whereby the beam diameter after the pinhole increases thus gives more uniform beam intensity. The expansion of the laser beam diameter by the spatial filter gives a closely approximated plane wave over the exposure area [112].

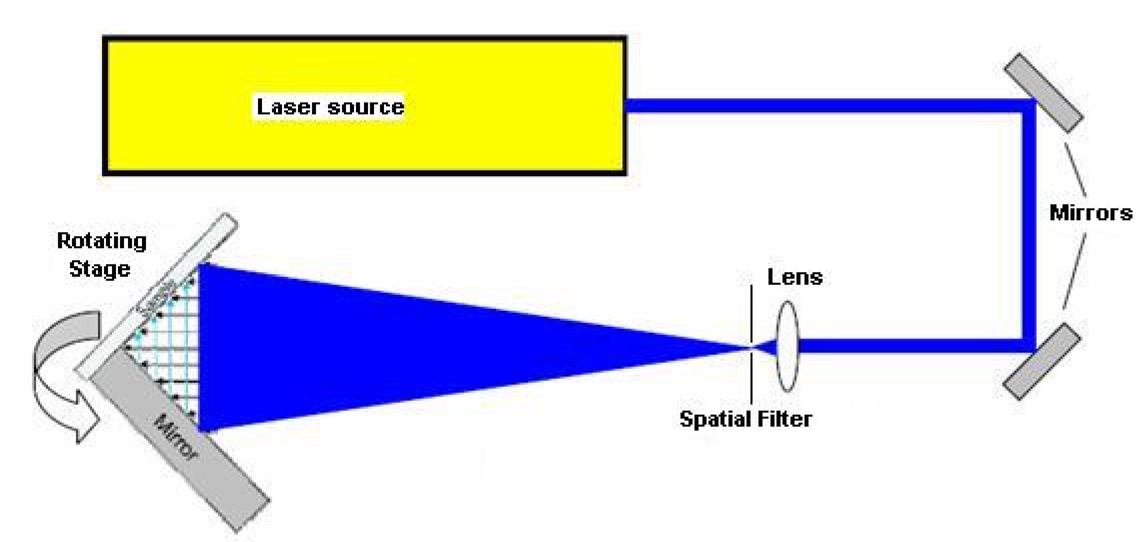

FIG. 3.2 Schematic drawing of a Lloyd's mirror setup for laser interference lithography of periodic structures on photoresist.

In front of the spatial filter there is a rotating stage with a mirror mounted perpendicularly to the sample holder. A part of the expanded beam is reflected by the mirror on the sample held at 90º to the mirror surface and interferes with the other portion of the beam on the sample to create grating-like standing wave, which is recorded on the photoresist layer of the sample. Due to the reason that the mirror is at the right angle corresponding to the sample surface, the light always reflectes at angle same as the original incident beam. Therefore, altering the angle of the incident beam by rotating the rotation stage varies the period of the pattern as mentioned in Eq. 3.1. In this case, different values of standing wave periods can be obtained and thus periodic structures with different dimensions can be created.

The period of the fringes can be as low as a half of the light wavelength of the incident laser beam. Therefore, depending on the types of laser used, structures in an order of sub-micron can be produced. The use of LIL technique enables the size of gratings or periodic structures to be as small as the half of the incident beam wavelength created on the photoresist. The applications of LIL include the patterning of magnetic media materials and MRAM (Magnetic Random Access Memory) devices, structuring of polymers and also creating distributed feedback (DFB) structures for quantum dot lasers. However, the utilisation of the LIL technique to create microlens arrays is a new field, which requires intensive study and experimentation.

3.1.3 Thermal reflow of photoresist

Thermal reflow of photoresist is one of the common techniques to get hemispherical lens profile and was first introduced by Popovic [39]. By heating the patterned resist structures at a temperature above the glass transition temperature of photoresist ($T>T_g$), the photoresist pillar pattern melts and pulls into a certain shape. Subjected to the force by the surface tension among liquid resist, substrate surface and surrounding air, the resist tries to minimize its surface energy [117-120]. For a given volume, the smallest surface is a sphere, thus hemispherical patterns forms on the substrate surface. The formed hemispherical structures can be directly used as lenses or as mask for the further etching to transfer the profile onto the substrate.

A pre-defined mask tends to restrict the pitch and size of the microlenses to the photomask's pattern, thus limiting the flexibility of the fabrication process. In this chapter the microlens arrays were fabricated by the combination of LIL and thermal reflow technique, which gave significant advantages over conventional photolithography with low cost and simple setup. The detail experiment procedure will be discussed and the properties of microlens arrays fabricated, such as roughness, uniformity and optical focusing ability, will be reviewed as well.

3.2 Experimental details

3.2.1 Sample preparation

There are several types of materials that are suitable for lens fabrication, such as polymer, fused silica and quartz. In this experiment, quartz was used as the substrate due to its excellent optical properties, which is ideal material to transmit light at a broad band of wavelength. Quartz also has high resistance to thermal shock and this enables the fabricated microlens arrays to maintain good physical properties, especially during etching process at a high temperature. Before the quartz sample was used, it was cleaned by solvents, such as acetone and IPA, to remove contaminations on the substrate surface.

The sample was then coated with S1805 positive tone photoresist from Shipley. To obtain a uniform layer of photoresist, the resist was spin coated on the sample surface by a spin coater. The centrifugal force during the spinning of the sample vacuum chuck causes the photoresist to widespread from the center of the sample until it covers the whole sample surface. The coater's spin speed determines the thickness of the photoresist coated over the substrate. For S1805 photoresist, a typical spin speed at 2000 rpm corresponds to a resist thickness of ~ 0.8 μm. The coated sample needs to undergo a pre-exposed soft bake at 115 ºC on a hot plate for 60 seconds to remove the moisture and harden the photoresist.

3.2.2 Exposure by laser interference lithography

The sample was exposed by the interference of two laser beams at a same angle, which results in the generation of periodic grating structures on the photoresist. The exposure was carried out by the Llyod's mirror setup with a Helium Cadmium (He-Cd) continuous wave (CW) laser (Kimmon, Japan) as the laser source. The laser wavelength λ is 325 nm with a long coherence length of 10 cm, which makes it suitable for interference lithography purpose.

After a single exposure, lines array periodic structure is formed. The subsequent cross exposure of the photoresist by rotating the sample in 90 degrees enables the forming of pillar arrays on the quartz surface. The period of the structure is set by changing the angle of the rotating stage. In this experiment, the angle was set as 4 degree, which is approximately equivalent to a period of 2 μm according to Eq. 3.1 and gives the pillars with a size of approximately 1 μm. The exposure time required to fully expose the photoresist mainly depends on laser fluence (mJ/cm^2) and developing time, allowing the exposed resist to be dissolved completely.

3.2.3 Resist reflow and reactive ion etching

The sample was then heated on a contact hot plate at a temperature for ~ 160 to 180 ºC. The heating of the photoresist pillars at a high temperature causes the resist to melt. Due to the surface tension among the melted resist, sample surface and surrounding air, the resist pillar changes its shape into hemispherical to minimize the surface energy. The dynamic mechanism of the resist reflow can be explained and modeled by the Navier-Stoke equation [119]:

$$\rho \frac{\partial u}{\partial t} = -\Delta P + \rho g + \eta \Delta u \tag{3.2}$$

where ρ is resist mass density, u flow speed, P external pressure, g dynamic viscosity and g gravitational acceleration. The gravity effect is negligible ($\rho g \sim 0$) so the external force applied on the fluid is the external pressure exerted on the surface and is resulted from Laplace' law, thus Eq. 3.3 is obtained:

$$\Delta P = \left(P_{\text{int}} - P_{ext}\right) = \frac{2\gamma}{R} \tag{3.3}$$

whereby γ is the resist surface tension and *R* the surface curvature radius.

By proper control of the heating parameters such as time and temperature, the large area of resist pillars forms into microlens arrays on the quartz surface. However, due to low chemical and thermal resistances of photopolymer material, the photoresist microlenses patterns need to be transferred into the quartz substrate by reactive ion etching (RIE). RIE is the most common dry etching process suitable for pattern transfer onto SiO_2 substrate [121-129]. It uses gases, such as CHF_3, CF_4 and SF_4, etc as the etchant to perform the etching process.

3.3 Characterization techniques

3.3.1 Optical microscope

This is the basic 2D image acquisition technique to examine the uniformity of the photoresist patterns before and after the thermal reflow. It is also used to measure the dimension of the patterns, such as the periods of the structure as well as the size of the pattern. The Olympus MX-50 optical microscope was used in this experiment. It is equipped with up to 150× magnifications and connected to a CCD camera fed to image acquisition software for accurate measurement. The optical microscope illuminates the sample either through the top light or backlight, which makes the characterization more versatile.

3.3.2 Atomic force microscope (AFM)

The AFM is a non-destructive characterization technique that is able to image 2D and 3D profiles of a sample by scanning through the sample surface. In an AFM system, a tip made of Si_3N_4 is mounted on the micro-fabricated cantilever. During the scanning of the sample, the small force of interaction between the tip and sample surface causes the tip to reflect as it scans through the sample surface, thus revealing the sample's topography. The recorded topography, which is in 3D form, can be displayed using the microscope software. In this case, the various information of the measured sample, such as width, height and defects of the microlenses can be extracted from the 3D image easily. The AFM used in this project, DI 3100 from Veeco Instrument, has the capability of vertical resolution of 1 Å.

3.3.3 Scanning electron microscope (SEM)

SEM serves as an alternative to the optical microscope and AFM to retrieve the sample's surface morphology information. By applying a voltage to the sample, SEM is able to capture the image of the sample surface by the reflected electrons. Due to the conductivity requirement, for non-conductive materials such as quartz, it is important to coat the sample with a layer of Au film by sputtering machine or thermal evaporator. This could be a disadvantage as compared to AFM since it can only be used to examine samples after the RIE etching instead of un-etched sample with the photoresist coated on it. This is because the Au coating on the photoresist damages the underlying photoresist when gold etchant is used to remove the thin Au layer.

3.4 Microlens arrays formation

3.4.1 Optimal laser interference lithography parameters

The optical characteristic of photoresist plays an important role in determining the quality of the patterns obtained after the LIL. Figure 3.3 shows the absorbance spectrum for S1805 photoresist obtained from the data sheet provided by the photoresist manufacturer. It shows that the strongest absorption occurs for the wavelengths between the lower side of the UV and near to deep UV regions, which is from 300 to 420 nm. At the wavelength, λ = 325 nm, which is the wavelength for the He-Cd laser, the absorption is very high at about 0.98. Since it is close to the peak absorbance, the S1805 photoresist is suitable for the lithographic process.

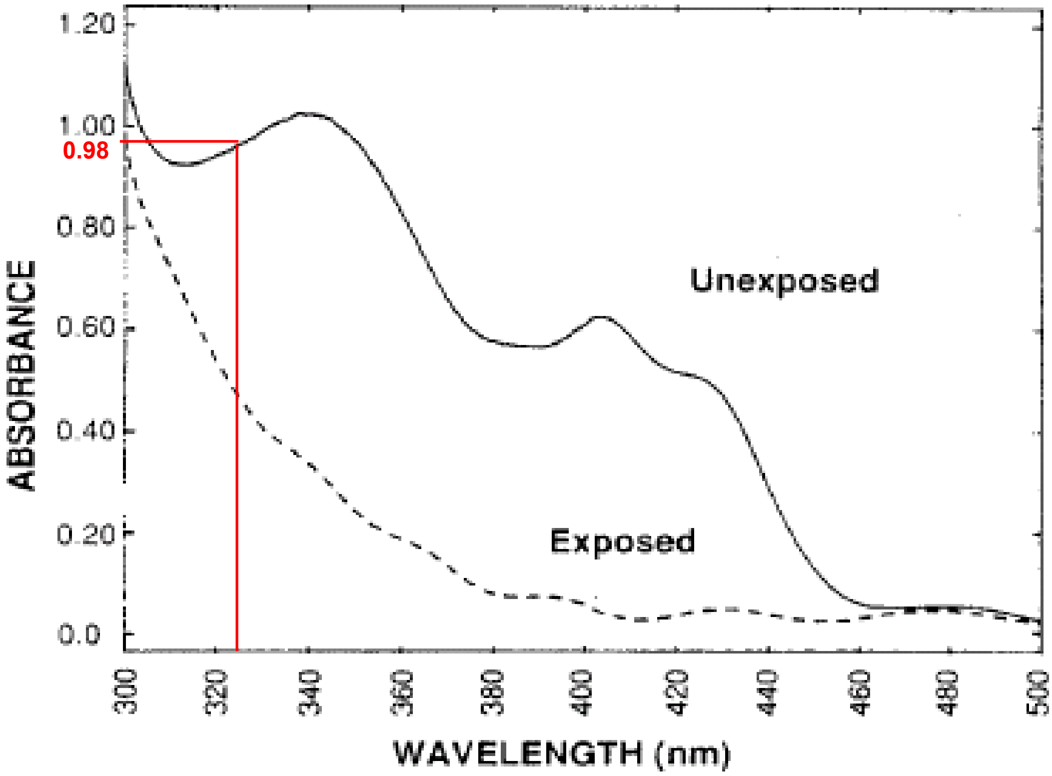

FIG. 3.3 Absorption spectra for Shipley S1805 photoresist. Corresponding absorbance for wavelength of 325 nm is about 0.98.

Single exposure gives parallel line arrays, while the cross exposure of the photoresist produces rectangular packed arrays of pillar patterns. Since the angle of the Lloyd's mirror was set at 2.5° ~ 4°, the period of the standing wave was about 3.7μm ~ 1.8 μm according to Eq. 3.1. Figure 3.4 shows an optical microscope view of a sample after the cross exposed two times at 90° and developed the exposed resist for 30 seconds. From the figure, it can be found that the patterns formed were in circular shape instead of square shape. This is due to the Gaussian beam profile of the laser source. The diameter of one pattern is about half of the period, which is about 1 μm.

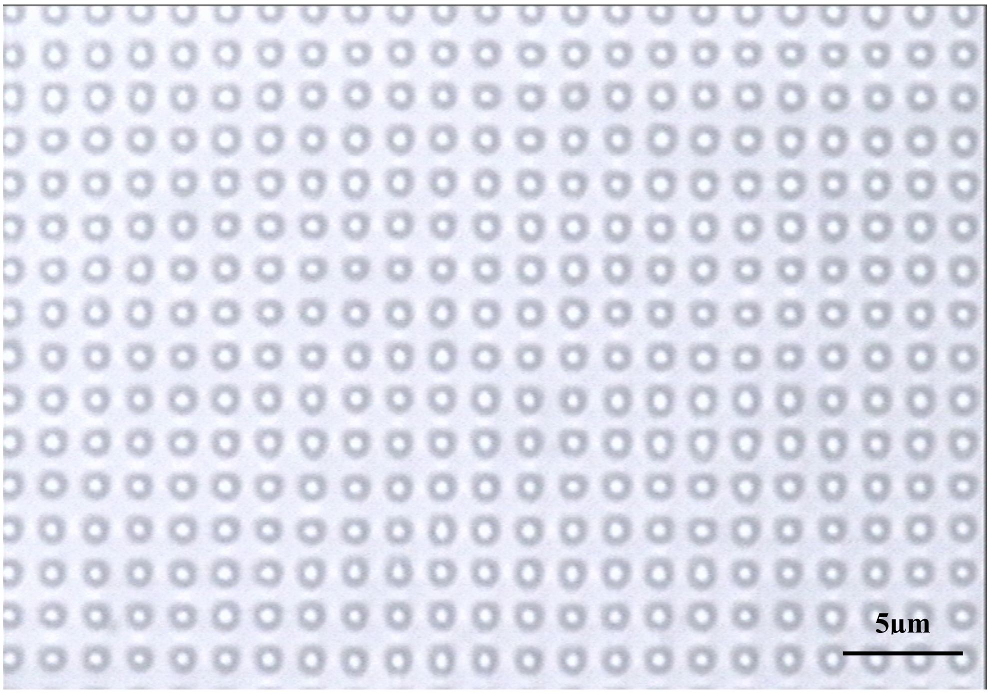

FIG. 3.4 Optical microscope image of dot arrays on photoresist after two times of cross exposure.

The optical microscope offers a very simple way to determine the quality of the resist exposure and development. However, optical microscope is only able to capture images in 2-dimension. Therefore, it is difficult to get 3-dimensional profile of the patterns, for example its height in order to determine the patterns is under or over expose.

The other limitation of the optical microscope is the resolution due to the diffraction limit of the objective lens. The surface image of a same sample was captured by an optical microscope and AFM as shown in Figs 3.5 (a) and 3.5 (b), respectively. From Fig. 3.5 (a), it is clear that the patterns profile is circular in shape, uniformly distributed over the sample surface. By AFM scanning across the sample surface, it is found that the patterns are not fully circular. There was a 'sharp edge' at one side of all patterns, forming oval-like patterns as shown in Fig. 3.5(b).

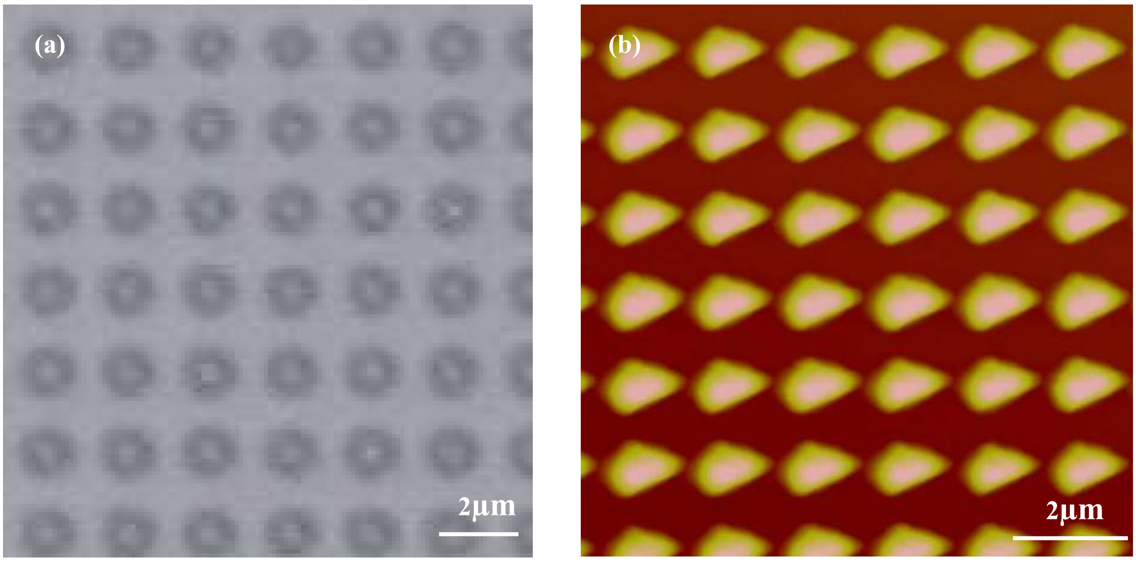

FIG. 3.5 (a) optical microscope and (b) AFM images of sub-micron patterns formed on a same sample surface after the photoresist is developed away.

This is due to the variations of the laser intensity distribution between two exposures and insufficient exposure. For a Gaussian beam distribution, the intensity of the laser is the strongest at the centre of the beam and dropped gradually as it moves outwards from the circumference. When the sample was rotated after the first exposure, it is possible that the sample is placed in a region where the intensity was not equal to the intensity during the first exposure. This results in the second exposure being of insufficient or excessive exposure relative to the first exposure if the exposure time is remained same.

This can be solved by either placing the sample to ensure the exposure area at the same location on the sample holder or increasing the exposure time for the lower intensity exposure. Figure 3.6 shows a sample after resist development, whereby the exposure area was adjusted so that the laser intensity remained the same. It is clear that the photoresist structures were more circular as expected after the two exposures. The other way to solve this problem is to place the sample far from the spatial filter so that the laser beam expands until its wavefront is close a plane wave profile. However, this will significantly reduce the laser intensity and increases the exposure time.

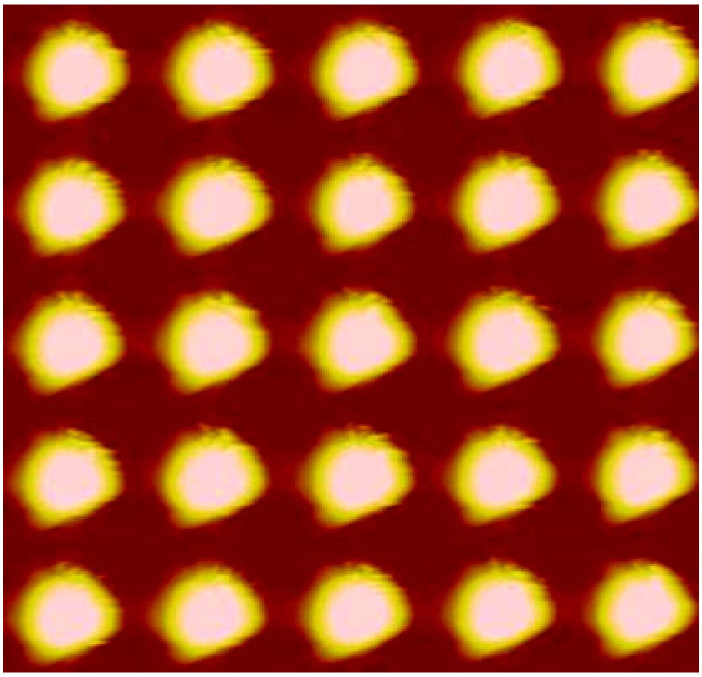

FIG. 3.6 The AFM image of patterns after the adjustment to make sure the exposure at the same location on the sample holder.

The patterning process by laser interference lithography with the Lloyd's mirror set-up is very successful in producing large arrays of identical line or circular structures. During the resist exposure, laser fluence plays an important role that affects the patterns quality. From the experiment data, it is found that the optimal range of laser fluence resulting in sufficient exposure of photoresist is from 20 mJ/cm^2 to 55 mJ/cm^2.

With the samples exposed within this range of laser fluence, the pattern size is about a half of the standing wave period. As the laser fluence increases, the pattern shrinks and becomes smaller until there are no patterns formed on the sample surface. This is because all the resist has been dissolved away. The increase in pattern size with respect to the laser fluence is attributed to the increase of laser energy absorbed by the photoresist. In this case, more energy absorbed means that more photoresist undergoes photo-chemical reaction and thus more resist is washed away during the resist development. Figure 3.7 (a) shows an optical microscope image of a sample over-exposed at a laser fluence of 67 mJ/cm^2 as the dot size is small. Figures 3.7 (b) and 3.7 (c) show other two samples, which were exposed at laser fluences of 20 mJ/cm^2 and 45 mJ/cm^2, respectively.

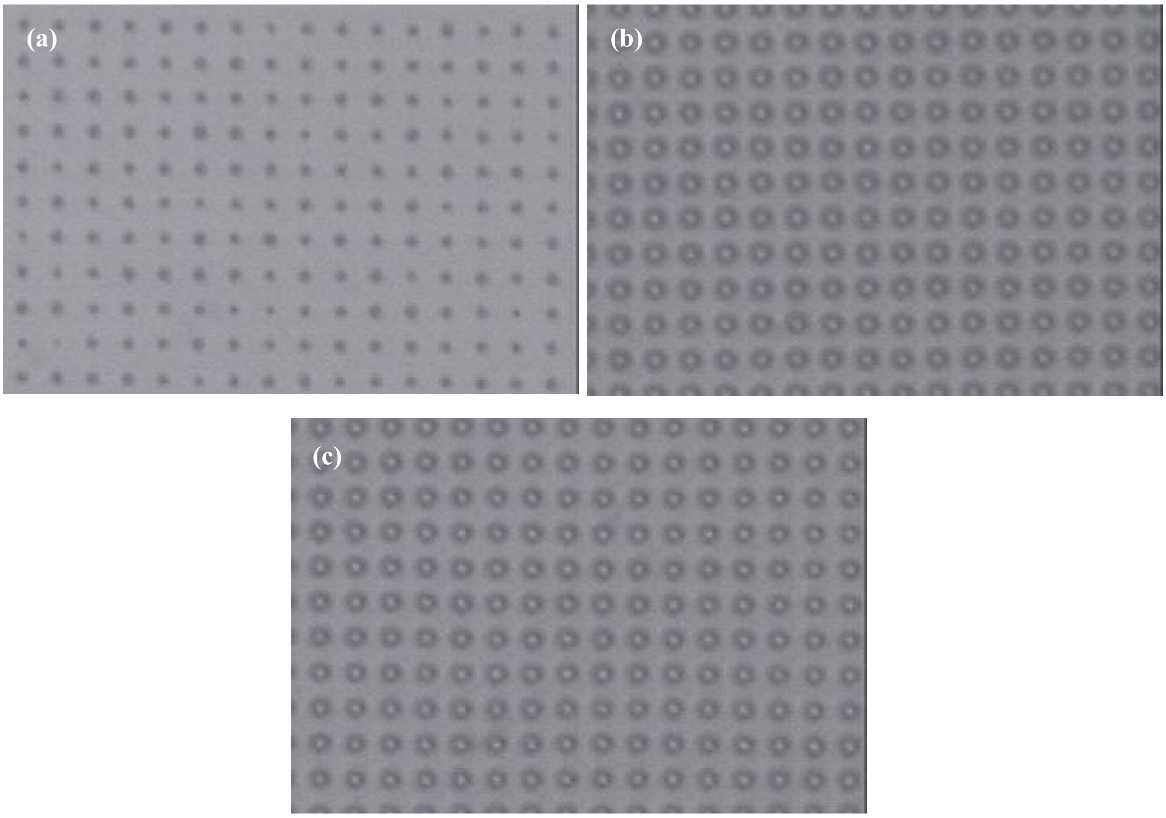

FIG. 3.7 Optical images of three samples surface after exposed at laser fluences of (a) 66.85 mJ/cm^2, (b) 45 mJ/cm^2 and (c) 20 mJ/cm^2, respectively.

To further verify the influence of laser fluence on the pattern size, two samples were exposed at different laser fluences. Other parameters such as period, reflow time and temperature, were set as constants in this case. Figure 3.8 shows the three dimensional AFM images and the corresponding microlens width measured at the cross-sectional view. It is shown that the microlens width is larger for the sample in Fig. 3.8 (a) as compared to the sample in fig. 3.8 (b). The former was exposed at 27 mJ/cm^2 while the latter was exposed at 45 mJ/cm^2. The period remains the same at 3.28 µm for both samples.

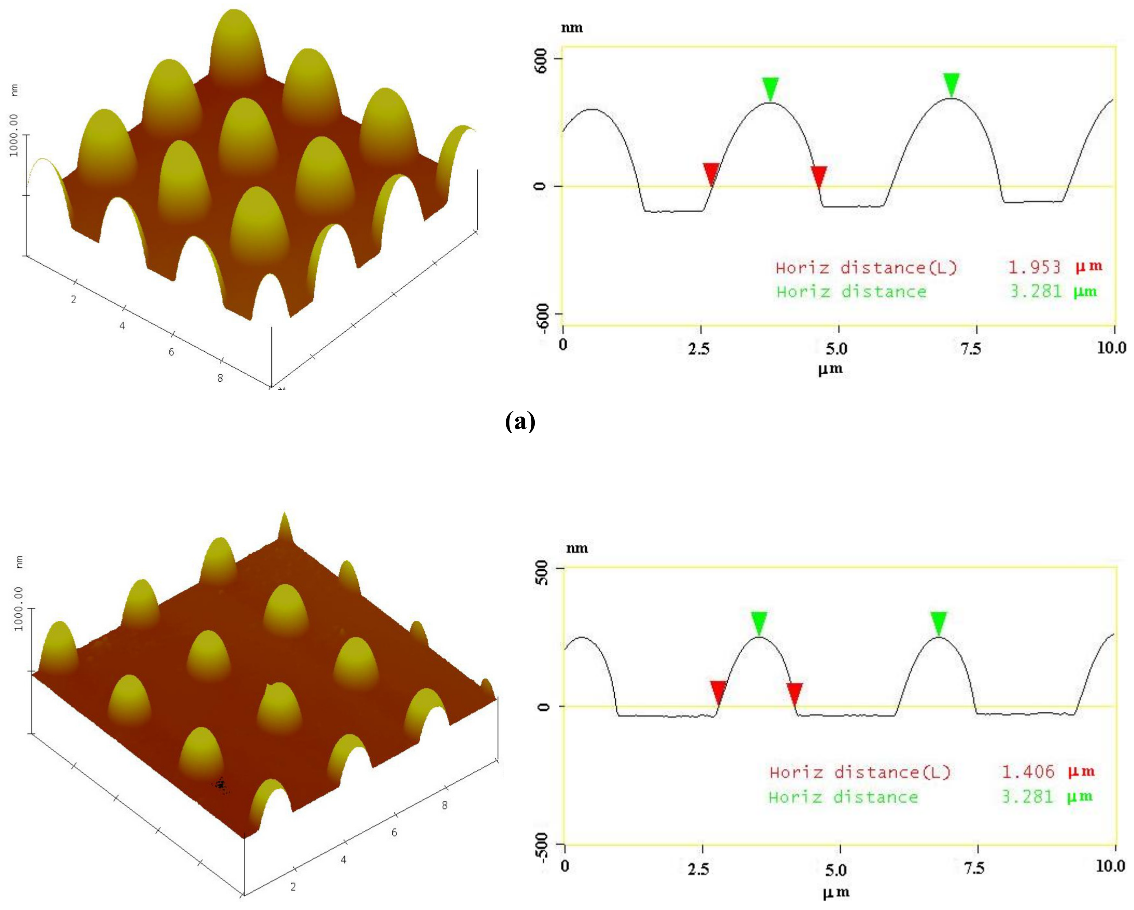

FIG. 3.8 AFM images of different samples exposed at laser fluences of (a) 27 mJ/cm^2 and (b) 45 mJ/cm^2.

3.4.2 Thermal reflow forming of microlens arrays

Figure 3.9 shows the photoresist pattern arrays after thermal reflow captured by optical microscopy and AFM. Figure 3.9 (a) is the cylindrical microlens arrays (single exposure) and Fig. 3.9 (b) is the plano-convex microlens arrays (cross exposure). Thermal reflow process allows the photoresist structures to melt and reflow to form cylindrical or hemispherical microlenses due to the surface tension of the melted resist [39]. It was also found that after the thermal reflow process, the samples which had oval shaped photoresist structures resulted from unequal exposures were corrected to circular shapes and had a good surface profile.

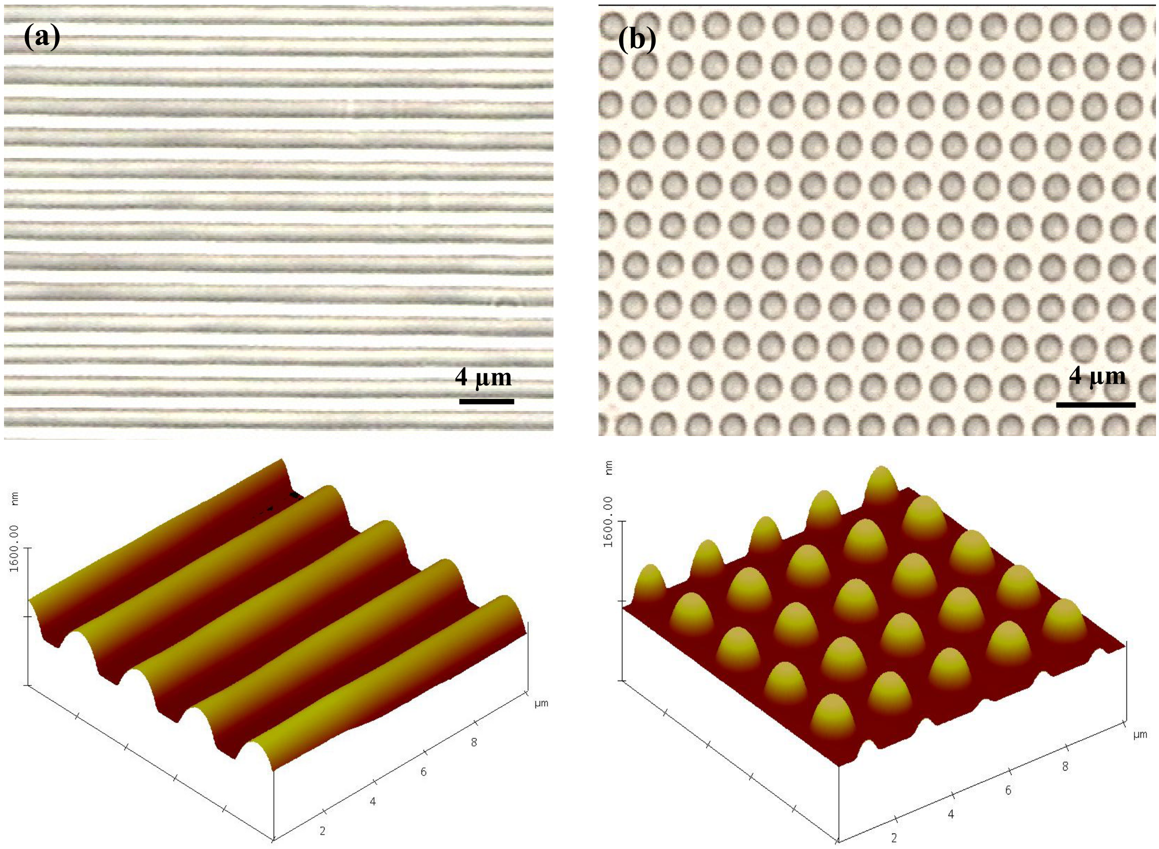

FIG. 3.9 Optical microscope images and AFM 3 dimensional profiles of (a) cylindrical microlens arrays and (b) plano-convex microlens arrays, after the photoresist reflow.

To verify that the patterns only change its shape to hemispherical while maintain the same pitch distance, AFM was used to scan across a sample before and after the thermal reflow process. Figure 3.10 shows two cross-sectional measurements of the sample surface for the 2 process situations. Several changes have been observed. Firstly, the period of the photoresist structures and the arrangement of rectangular packed structures are not affected by the thermal reflow process. It was found that the periods before and after reflow are almost the same when random measurement was done across the sample. Table 3.1 shows a comparison of the period before and after reflow. Five randomly selected points were measured before and after the reflow process. Similar results were obtained for other samples.

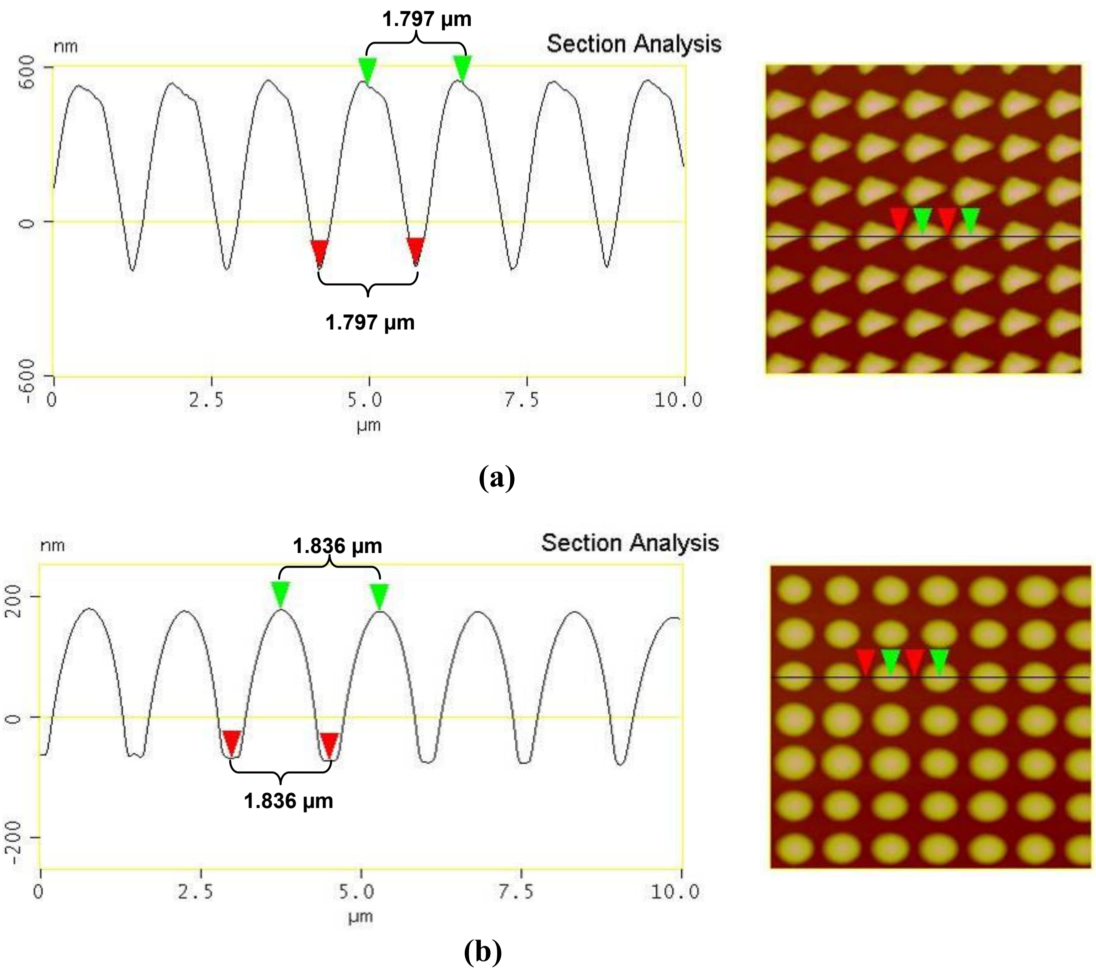

FIG. 3.10 AFM sectional analyses of photoresist patterns (a) before and (b) after the reflow.

Table 3.1 Comparison of the pitch of microlenses before and after the reflow.

Data points	1	2	3	4	5	**Average**
Before reflow	1.797 µm	1.875 µm	1.836 µm	1.797 µm	1.797 µm	**1.820 µm**
After reflow	1.797 µm	1.836 µm	1.797 µm	1.836 µm	1.836 µm	**1.820 µm**

It is also observed that the structures are corrected and form circular based microlens array. It was also noticed that after the reflow, the height of the photoresist structures was reduced. This is because when the photoresist structures reflow to form hemispherical structure, the resist tends to pull together to reduce the surface energy while maintain a constant volume to reduce the height of the microlenses. The heating of photoresist also causes the resist to vaporize slightly from the resist surface in some extend; therefore the height becomes lower.

Figure 3.11 shows the dependent of microlenses width on the reflow time and reflow temperature. Three reflow temperatures, 160 °C, 170 °C and 180 °C were investigated by varying the reflow time from 50 seconds to 100 seconds. The interval was set at 10 seconds and two samples were measured for each interval. As the reflow temperature increases, the microlenses width becomes larger. The same phenomenon was observed for increasing the reflow time. This could be because the increase of temperature or heating time reduces the viscosity of the resist during the melting; thus the resist becomes wider. Temperature increase also reduces the surface tension. The relationship among reflow temperature, reflow time and microlens width gives an idea to control the microlens radius of curvature and its focal length.

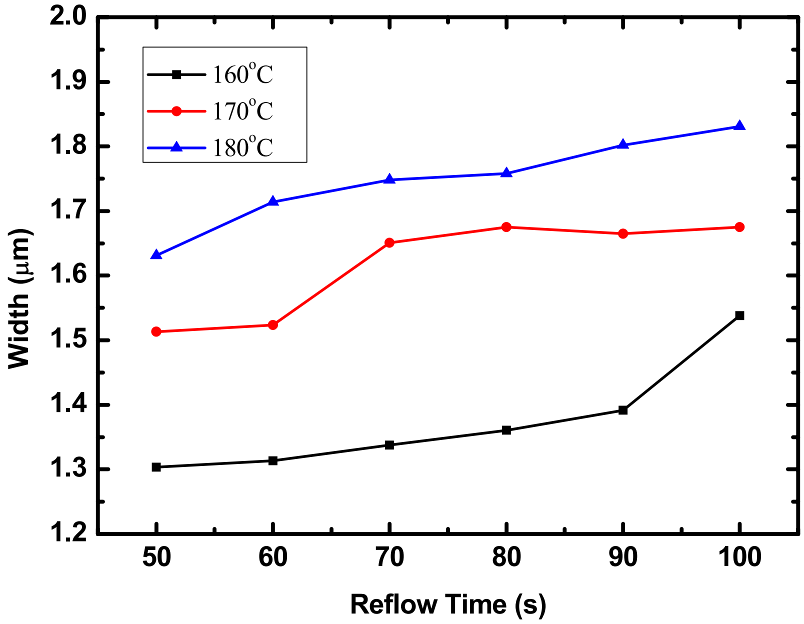

FIG. 3.11 Dependence of microlenses width on the reflow time at reflow temperatures of 160°C, 170°C and 180°C, respectively.

The reflow process is also affected by the exposure condition. During the exposure process, if there is insufficient exposure energy or duration, it causes photoresist under-exposure. Under-expose subsequently causes the area of photoresist that is supposed to be developed away becomes not fully removed. This leaves some residual resist connecting the photoresist structures, as shown in Fig. 3.12. The sample was exposed at a laser fluence of 17 mJ/cm^2. When the sample was heated up to its melting temperature, the residual resists tend to pull adjacent patterns together to form a series of holes instead of lens arrays. Figure 3.13 shows the AFM image of ‘hole’ patterns after the resist reflow.

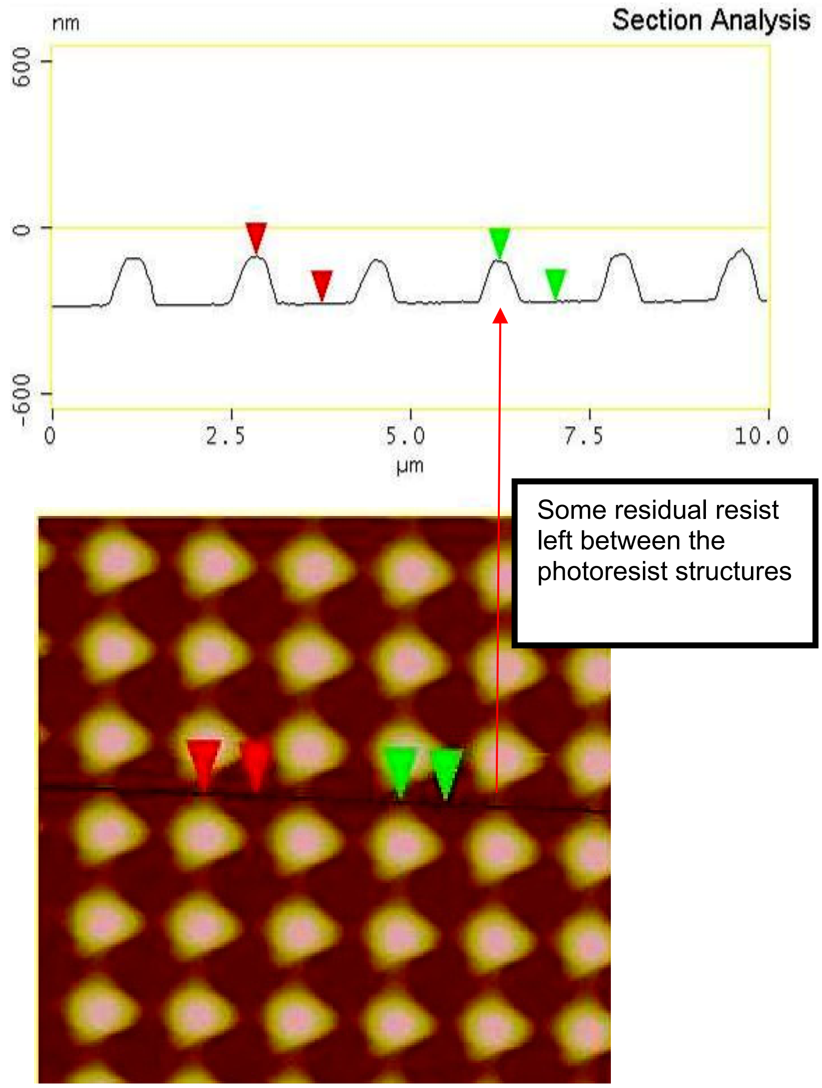

Some residual resist left between the photoresist structures

FIG. 3.12 Residual resist left over at the exposed area when the resist is under-developed.

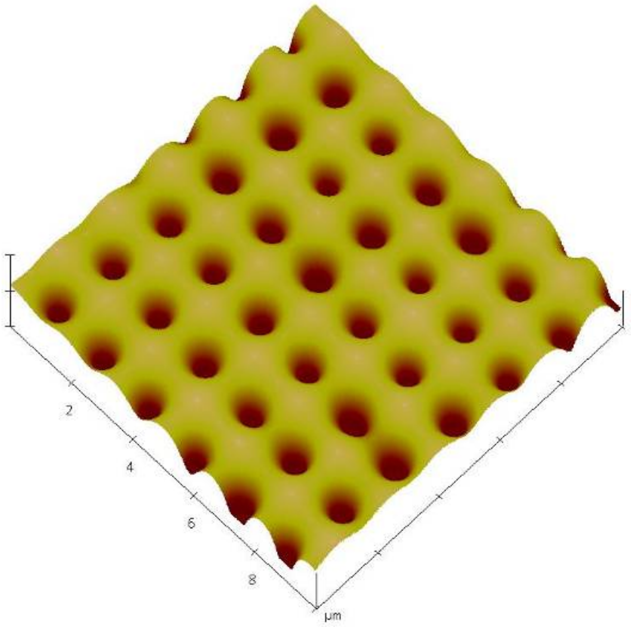

FIG. 3.13 ‘Hole’ patterns after the reflow caused by the incomplete exposure.

The success of thermal reflow process highly relies on the LIL exposure and development processes. As long as the photoresist is fully exposed, the thermal reflow process will melt the photoresist structures to form the microlens array. The period between two structures melted into identical microlenses is pre-determined by the laser interference fringes and does not change with reflow conditions.

3.4.3 Pattern transfer by reactive ion etching (RIE)

In order to transfer microlens patterns after the reflow onto the quartz substrate, an anisotropic etching method, namely reactive ion etching (RIE) was used to perform the task. In this case, isotropic etching is no longer suitable for such pattern transfer process since the isotropic etching results in undercut at the sides of the base of the photoresist microlenses. On the other hand, RIE process maintains almost a same profile after etching due to its anisotropic nature depending on the etch rates of the photoresist and quartz substrate. To determine the etch rates of both the photoresist and quartz substrate, the sample with S1805 photoresist was coated and sent for RIE etching under CF_4 gas at a flow rate of 45 sccm (standard cubic centimetre per minute). The resist thickness before and after etching as well as the etched substrate depth after the resist stripping was measured. The calculated etch rates for photoresist and quartz are shown in Table 3.2. It can be seen that the etch rates for both photoresist S1805 and quartz substrate are almost the same at about 61 nm/min. To fully transfer the resist microlenses structure onto quartz substrate, the amount of time for the RIE etching should take into account the height of the microlenses.

Table 3.2 Etch rate of photoresist and quartz etched using CF_4 gas RIE.

Resist Thickness coated (A)	Depth Measured after RIE (with resist) (B)	Depth Measured after resist stripped (depth of sample etched) (C)	Depth of resist etched {A-(B-C)} (D)	**Sample Etch rate (nm/min) (C/13)**	**Resist Etch rate (nm/min) (D/13)**
940	916	775	799	**59.6**	**61.5**
880	874	809	815	**62.2**	**62.7**
896	877	770	789	**59.2**	**60.7**
826	818	780	788	**60.0**	**60.6**
			Average	**60.3**	**61.4**

To verify whether the resist microlens patterns are fully transferred onto the quartz substrate, the two dimensioanl lens profiles of the sample before and after the RIE etching were measured and compared as shown in Fig 3.14. There is a slight difference in the height of the microlenses, 343.15 nm before the RIE (Fig. 3.14 (a)) and 342.96 nm after the RIE (fig. 3.14(b)). The photoresist S1805 has an etch rate slightly higher than the quartz. The microlens surface profile remains smooth after the

RIE. The difference is 1.0 % and it shows that the photoresist microlens patterns are fully transferred onto the quartz substrate. The surface morphology of the etched sample can be observed by the SEM. Figure 3.15 shows a SEM image of the MLA fabricated after the RIE etching. The microlenses are uniformly distributed with excellent surface finish.

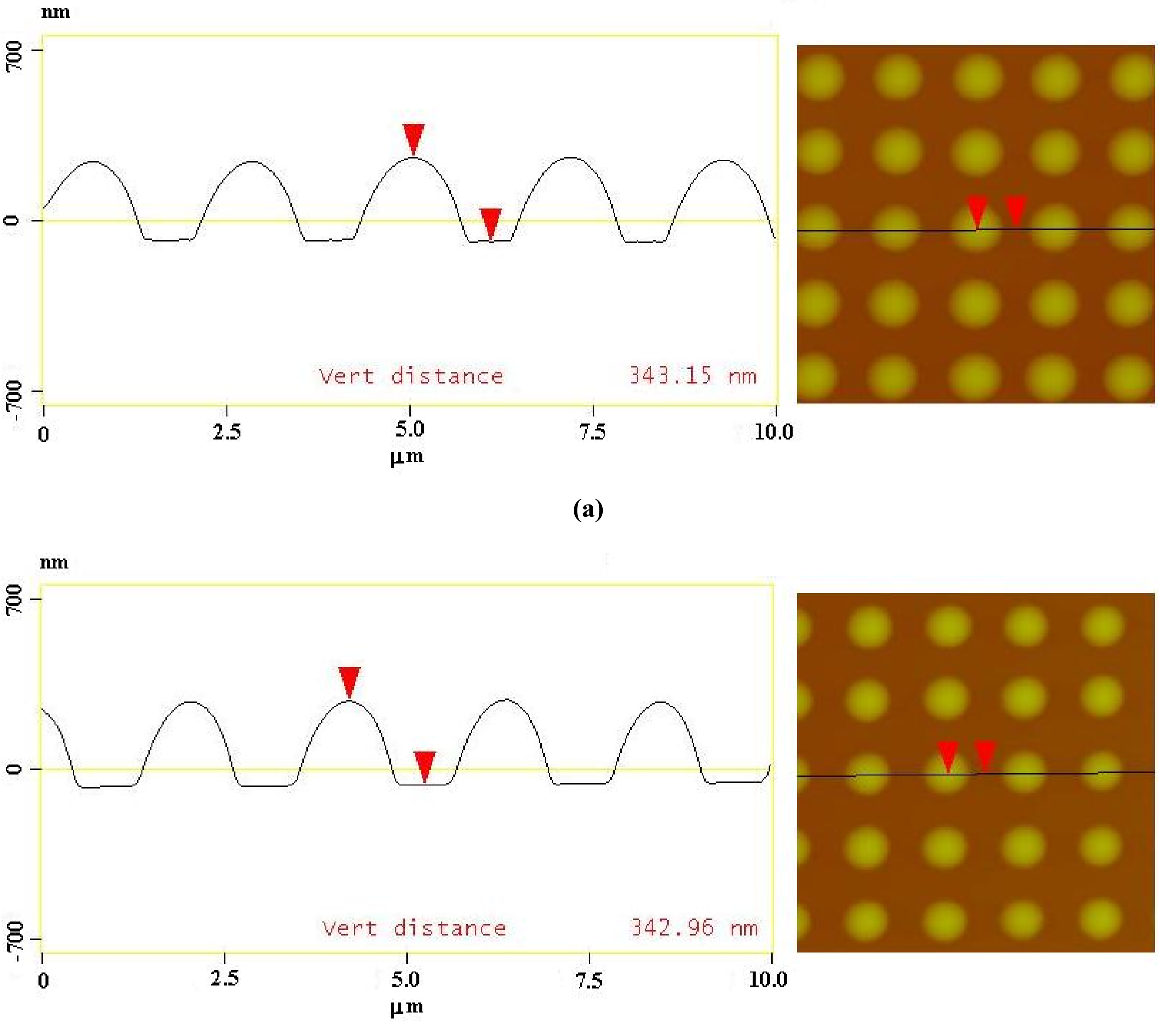

(a)

(b)

FIG. 3.14 Sag height and pitch of microlenses (a) before and (b) after the RIE.

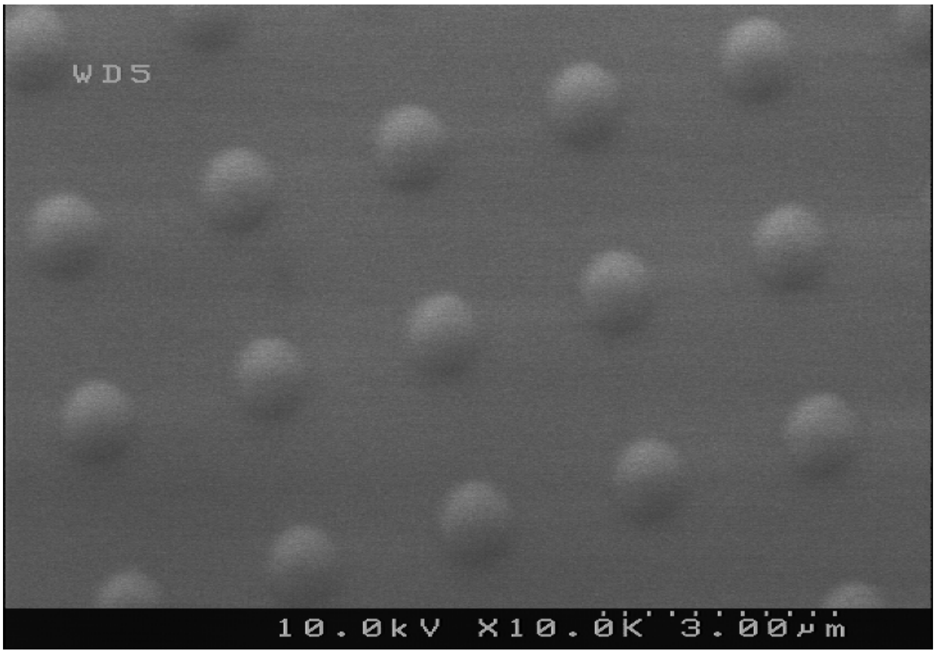

FIG. 3.15 SEM image of a MLA sample after the RIE etching.

3.4.4 Microlens uniformity and surface finish

The physical properties of the fabricated microlenses were measured by the AFM with a vertical resolution of 1 Å. The surface roughness of the lens was measured at the area of the lenses peak. It was found that the lenses have excellence surface quality with average mean roughness *Ra* of 2.67 nm. Such roughness is critical as smooth optical surface reduces the optical aberration and gives better light focusing.

Microlens array uniformity is the indicator of the variation of microlens dimension, such as width and sag height value across the fabrication area. To determine the uniformity of the microlens array, total 60 data points were collected by measuring 60 different microlenses at 5 locations across the a microlens array sample for their width and sag values. The histograms on the distribution of these values are shown in Fig. 3.15.

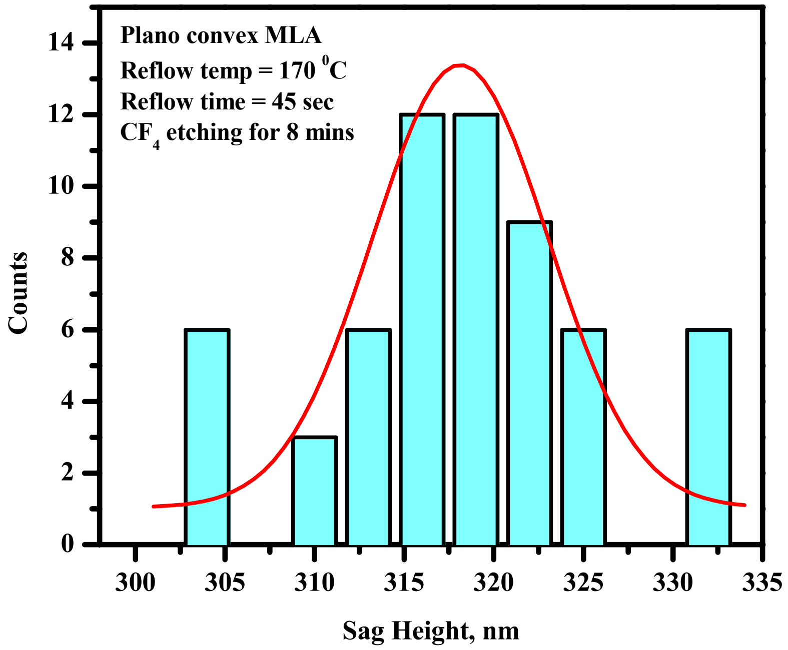

(a)

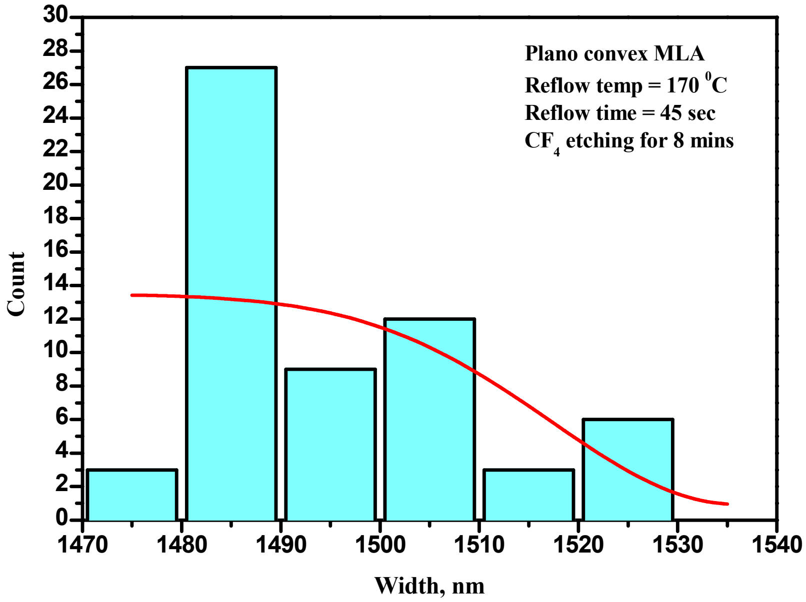

(b)

FIG. 3.16 Histogram distributions of microlense (a) sag height and (b) width measured over a microlens array sample. Total 60 points were taken.

For the microlenses sag height, it can be seen from Fig. 3.15 (a) that the mean sag height is calculated at 318.50 nm with a standard deviation of 6.43 nm, which is equivalent to 2.02% of error. As for the microlenses width, the mean value is 1495.1 nm and standard deviation of 14.13 nm. The dimensional error is 1.00 %. The measured results show that the microlens array fabricated has a very good uniformity of microlenses over the sample area.

3.5 Optical focusing ability of the microlens array fabricated

A laser light illuminates through the MLA is focused by the individual microlenses and forms an array of light spots. Here, the Point Spread Function of a diffraction-limited (dl) lens when a light incident on a lens is given by [130]:

$$PSF_{dl}(r) = \left| \frac{2J_1\left(\frac{kD_r}{2FL}\right)}{\frac{kDr}{2FL}} \right|^2 \tag{3.4}$$

where r the radial coordination in the focal plane with the focal point as center, k the wave number ($k=2\pi/\lambda$), D the lens diameter and J_1 the first order Bessel function. Equation (3.4) is obtained when the far field calculation of the intensity profile (Fraunhofer diffraction pattern) at the focal plane through a lens pupil $P_{ideal}(r, \theta)$ is normalized. In this case, the focal spot of the Gaussian beam is considered diffraction limited and the diameter of the spot size can be calculated as the full $1/e^2$ width of the beam waist as given by Eq. 3.5.

$$D_{spot} = 1.26\lambda F/\# \tag{3.5}$$

In order to examine the ability of the fabricated microlens array in focusing a light source, the microlens array was illuminated by a laser light from the top and an 80X objective lens was placed under the microlens array. By adjusting the objective lens so that it focused on the focal plane of the MLA, the image of the laser light focused by the MLA was captured as shown in Fig. 3.16. It is clearly seen that the microlens array can effectively focus the incoming laser beam into a series of identical tiny light spots. The laser beam was focused by a plano-convex microlens array (Fig. 3.15 (a)) and cylindrical microlens array (Fig. 3.15 (b)), respectively.

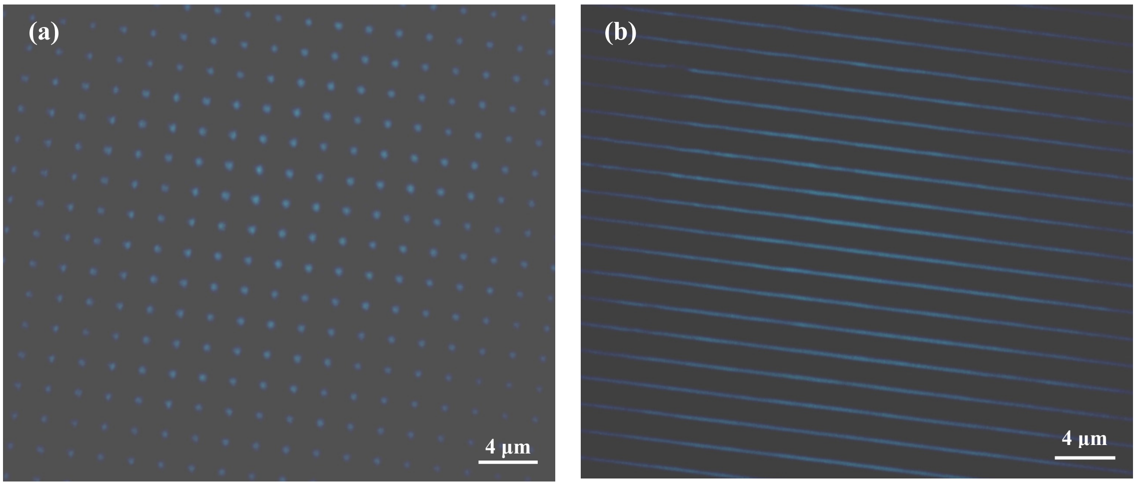

FIG. 3.17 The incoming laser beam was focused by (a) a plano-convex microlens array and (b) a cylindrical microlens array.

The microlens array was also used to perform surface nanolithography by record the focused light beams on to a photopolymer layer coated on a Si substrate. The surface nanopatterning can be carried out by placing the substrate at a distance equal to the focal length of the MLA and allowed the photopolymer to be exposed by illuminating the microlens array with a laser source. Figure 3.17 shows the results obtained after the substrate was exposed and developed. A series of dot arrays were formed on the photopolymer layer with an average diameter of 210 nm measured at full-width at half maximum (FWHM). It was also seen that the holes were evenly spaced in square packed shape with a distance between 2 dots of 2 μm. This equals to the arrangement and the pitch of the microlens array as expected.

However, it was also noticed that there was low uniformity in the holes formed. The holes were of different sizes. This may be due to the microlens array not fully parallel to the photoresist sample, causing some holes to be bigger and some to be smaller. A few possible applications of this surface nanopatterning method are the photonic crystals and also the nano-gratings fabrication for VCSEL semiconductor lasers.

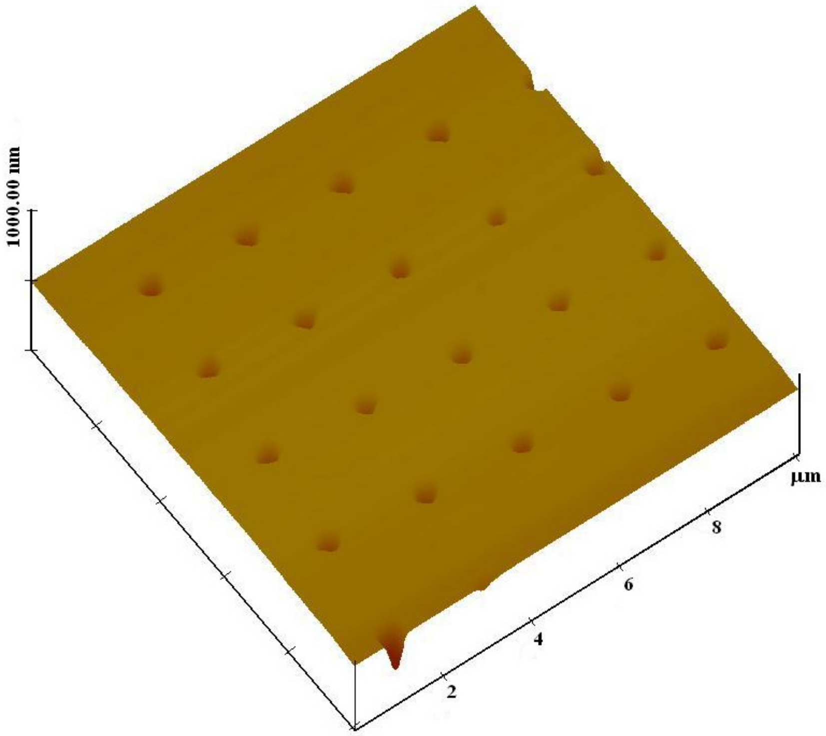

FIG. 3.18 Dot arrays generated on the photopolymer layer by the laser illumination through the microlens array.

In the following chapter, geometrical and physical optics simulation techniques were used to simulate and understand the optical behavior of the microlens array when it is under a light illumination. The models and algorithms used in the simulation will be introduced as well. The simulation results are compared with the experimental observations and followed by some explanations.

CHAPTER 4

SIMULATION STUDIES OF FIELD DISTRIBUTION OF MICROLENS ARRAYS

4.1 Background

To study the behaviors and properties of light and its interaction with microlens array, it is necessary to carry out theoretical simulation analysis using a suitable micro-optical system modeling technique. The simulation technique should be able to give detail analyses and characterization of a particular micro-optical system when a single or multiple sources of light propagate through the system. The classical theoretical simulation techniques of micro-optics generally can be divided into the geometrical optics and the physical optics. Geometrical optics modeling involves the tracing of rays, which can be represented by a series of imaginary lines. Physical optics or wave optics, on the other hand, models the propagation of light wavefronts through optical systems, including both the amplitude and the phase of the wave [131-132].

In recent years, numerical methods, such as Method of Moment (MoM), Finite Elements Method (FEM), Finite-Difference Volume-Domain (FDVD) and Finite-Difference Time-Domain (FDTD) have been used to model the electromagnetic wave interaction with matter. Since light is a form of electromagnetic wave, its behavior and characteristic can also be described using Maxwell's equations. In this chapter, the method of microlens arrays modeling and simulation will be presented together with its results obtained.

4.2 General Ray Tracing

Ray tracing [133-135] is one of classical geometrical optics modeling and optimization techniques. It traces a series of optical rays that propagate along a certain optical axis in straight lines without interfering each other. Rays are imaginary lines that are normal to the optical wavefront, and it can be described by a position vector, $\vec{r}$ and direction vector, $\vec{e}$ as [132]

$$\vec{r} = (x, y, z) = \vec{p} + \mu\vec{e} \tag{4.1}$$

where $\vec{p}$ is the starting point of the particular ray, μ is a distance constant and $|\vec{e}|=1$.

When these rays are propagating through an intersection between 2 mediums eg, free space-optical surface, it changes its propagation direction through refraction and reflection. The point of intersection is subsequently used as the starting point of next ray path and all these can be calculated by a vector equation as mentioned above. The determination of ray’s propagation path and its corresponding optical path length keep continuing until the rays reach the final image surface.

There are two types of ray tracing, the sequential ray tracing and the non-sequential ray tracing. For the sequential ray tracing the surface where the optical system is hit by the rays is known; whereas for the non-sequential system, the actual path taken by the rays is not clear. The ray tracing of microlens arrays is one of the non-sequential methods. In general, ray tracing provides significant simplification and flexibility of modeling techniques for almost all micro-optical systems, but it fails to account for many important optical effects, such as diffraction and polarization.

4.3 Physical Optics Propagation

The physical optics models the propagation of wavefront in an optical system. Wavefront propagates in a same direction as optical rays in a constant phase and coherently self-interfere. A transfer function is computed when the wave propagates from an optical surface to another or from a medium to another. This beam is represented by an array of discretely sampled points similar to the ray tracing methods. It has taken into account of diffraction, interference and polarization during the modeling process.

For a plane wave propagating in a homogeneous medium, the plane wave can be written as [131-132]

$$Ae^{2\pi i\left(v_x x+v_y y+v_z z\right)} \tag{4.2}$$

where *v* represent the spatial frequency components of the plane wave. The angular spectra of plane waves are obtained by Fourier transform of the complex wave amplitude *u(x,y,0)* at *z*=0

$$\tilde{u}\left(v_x,v_y\right)=\int_{-\infty}^{+\infty}\int_{-\infty}^{+\infty}u\left(x,y,0\right)e^{-2\pi i\left(v_x x+v_y y\right)}dxdy \tag{4.3}$$

A transfer function by inverse Fourier transform is needed to propagate the plane wave to another location, said z_k by multiply the $\tilde{u}\left(v_x,v_y\right)$ with a propagator, *P*

$$P(z_k)=e^{\frac{i2\pi z_k\left[1-v_x{}^2-v_y{}^2\right]^{\frac{1}{2}}}{\lambda}} \tag{4.4}$$

where $P(z_k)$ describes the complex phase of a plane wave with unity amplitude and

$$\frac{\left[1-v_x{}^2-v_y{}^2\right]^{\frac{1}{2}}}{\lambda}=v_k$$

Therefore, the complex amplitude at z_k is the superposition of the propagated plane wave and is given as

$$u\left(x,y,z_k\right)=\int_{-\infty}^{+\infty}\int_{-\infty}^{+\infty}\tilde{u}\left(v_x,v_y\right)P\left(z_k\right)\left[e^{i2\pi\left(v_x x+v_y y\right)}\right]dv_x dv_y \tag{4.5}$$

In this case, the numerical solution can be obtained using the fast Fourier transform [136].

4.3.1 Simulation of Light Propagation through Microlens Array

Angular spectrum propagator works well when the beam is collimated but it is suitable only for the propagation in free space and homogeneous medium. For a micro-optical system whereby it consists of free space as well as various optical components with arbitrary surface, it is important to use the ray tracing method to trace the rays that represent the wavefront through the optical surface and construct the complex amplitude after each surface. Then the physical optics propagation is used to calculate the change in amplitude.

Since microlens array is non-sequential components, it is difficult to model using only physical optics propagation. In this section, the results of simulation of a laser irradiation of a microlens array using the combination of ray tracing and physical optics propagation is presented. Figure 4.1 shows the model of the microlens array arranged in hexagonally packed arrangement and the corresponding intensity distribution at the focal plane. The microlens array modeled has a diameter of 23 µm, sag of 9 µm, which gives a focal length of 28.7 µm. A laser light source of λ=400 nm was irradiated through the backside of the microlens array. As can seen from Fig. 4.1 (a) the microlens array effectively focused the incident laser beam into a series of discrete focus spots with equal intensity at the focal plane.

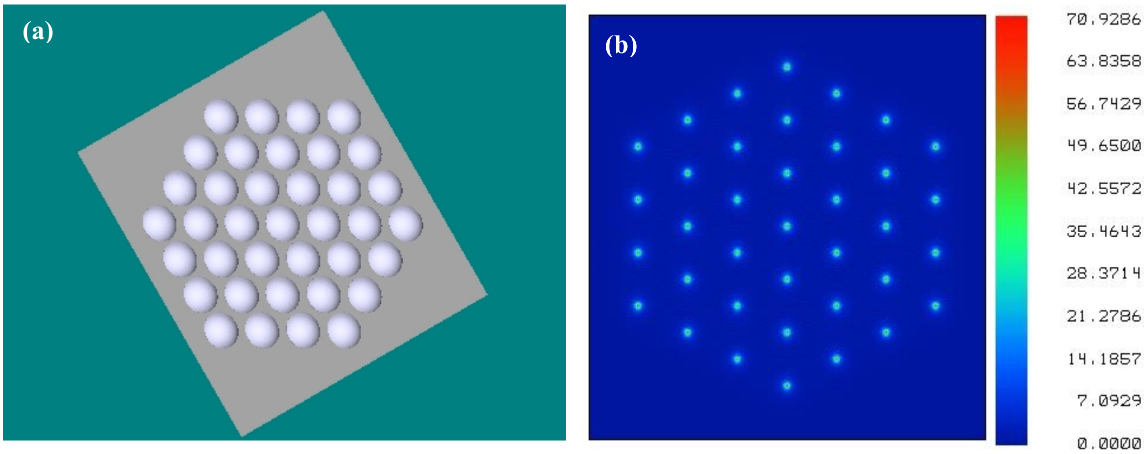

FIG. 4.1 (a) Microlens array model used in the simulation and (b) its corresponding intensity distribution at the focal plane.

The cross section of the focus spots was shown in Fig. 4.2. The figure shows that the incident laser beam was well focused by the microlenses whereby the energy was distributed at the center region with its full-width at half maximum (FWHM) measured at ~350 nm.

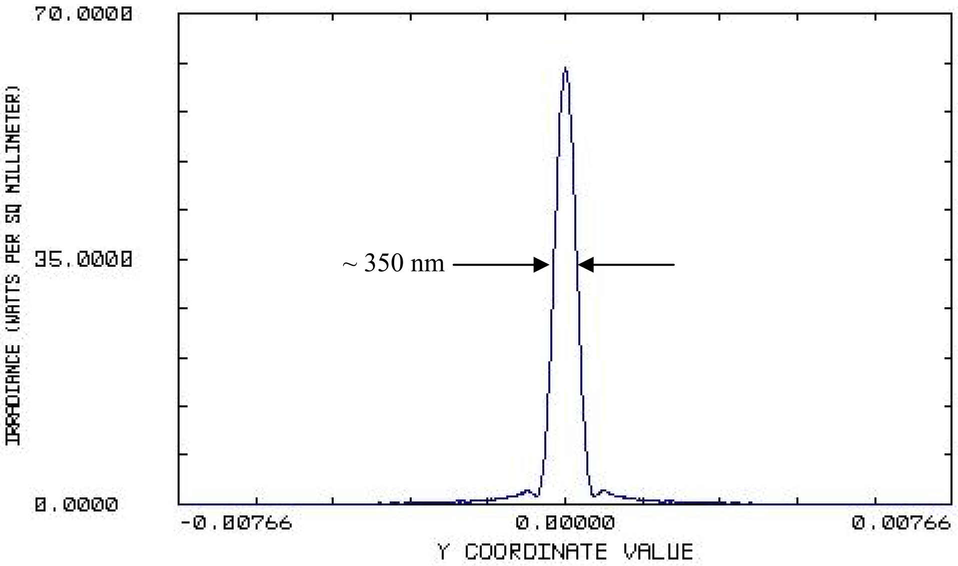

FIG. 4.2 The calculated FWHM of the focused laser spot from microlens arrays.

The model simulation shows that the combination of geometrical and physical optics gives a good prediction of the optical behavior and characteristic of light propagation through microlens arrays. However, geometrical ray model of light cannot adequately model the features with sizes in the order of wavelengths. When the size of microlenses becomes significantly small(close to wavelength of laser light), the strong diffraction effect takes place and therefore ray tracing approximation is no longer valid. The following section will introduce a numerical solution of Maxwell's equations for modeling the microlens arrays with a size of a few microns [137].

4.4 Finite-Difference Time-Domain (FDTD) Method

Finite-difference time-domain (FDTD) is one of the popular electromagnetic waves modeling and simulation techniques [138,139]. As compared to other techniques, such as finite elements methods (FEM) and method of moments, FDTD electromagnetic field analysis covers a wide range of wave frequencies; thus makes it suitable for numerical predictions of various problems that deal with electromagnetic wave-matter interactions. The FDTD solutions can be applied in engineering structures including antennas [140], photonic bandgap structures [141], liquid crystals [142], microcavity optical resonators [143], waveguides [144] and micro-optical components [145].

FDTD approach is simple, robust and yet gives a detail numerical prediction of electromagnetic wave behaviors. It does not need to solve a series of linear matrix equations as what FEM does. FDTD offers a direct solution of Maxwell's equations and transforms them into discretization equations. In general, FDTD provides a numerical solution to Maxwell's differential time-dependent equations [138]. It is a volume-based time-domain modeling technique which relates the electric field component, *E* and magnetic field component, *H* in space and time stepping process. In this case, the space and time derivatives of *E* and *H* components in Maxwell's curl equations are central-differenced and discretized before it is resolved in a so-called leapfrog manner. Therefore, the *E* field component is solved at a given instance of time followed by *H* field component, and is repeated over and over. The calculated *E* and *H* values are stored in the memory for the next time stepping process until the simulation process is completed.

4.4.1 Maxwell's Equations for Electromagnetic Wave

Maxwell's equations consist of a set of 4 equations that relate the electric field, *E* and magnetic field, *H* in the time-space relationships. Considering a space domain is free of electric or magnetic current source with a possibility of the existence of materials that absorb electric or magnetic field energy, the constitutive differential and integral forms of Maxwell's equations can be written as [138,139 ,146] following:

Ampere's Circuital Law:

$$\nabla \times H - \frac{\partial D}{\partial t} = J \tag{4.6a}$$

$$\frac{\partial}{\partial t} \iint_A D \cdot dA = \oint_l H \cdot dl - \iint_A J \cdot dA \tag{4.6b}$$

where *H* is the magnetic field strength in amperes per meter; *D* the electric flux density in coulomb per square meter and *J* the free current charge density in coulomb per cubic meter.

Faraday's Law of Induction:

$$\frac{\partial B}{\partial t} + \nabla \times E = 0 \tag{4.7a}$$

$$\frac{\partial}{\partial t} \iint_A B \cdot dA = -\oint_l E \cdot dl \tag{4.7b}$$

where *E* is the electric field in volts per meter and *B* the magnetic field density in tesla or weber per square meter.

Gauss's Laws for electric field and magnetic field:

$$\nabla \cdot D = 0 \tag{4.8a}$$

$$\oint\!\!\!\oint_A D \cdot dA = 0 \tag{4.8b}$$

$$\nabla \cdot B = 0 \tag{4.9a}$$

$$\oint\!\!\!\oint_A B \cdot dA = 0 \tag{4.9b}$$

For a linear, homogenous, isotropic and non-dispersive material, the interaction of electromagnetic wave with matter can be related to polarization density, *P* and magnetization density, *M* as following:

$$P = \chi_e \varepsilon_0 E \tag{4.10a}$$

$$M = \chi_m H \tag{4.10b}$$

The material equations of *D*, *B* and *J* [147] which relate to *E* and *H* are given as:

$$D = \varepsilon_0 E + P = \varepsilon_0 (1 + \chi_e) E = \varepsilon_0 \varepsilon_r E = \varepsilon E \tag{4.11a}$$

$$B = \mu_0 (H + M) = \mu_0 (1 + \chi_m) H = \mu_0 \mu_r H = \mu H \tag{4.11b}$$

$$J = \sigma E \tag{4.11c}$$

where P in coulombs per square meter, M in ampere per meter, χ_e the electrical susceptibility of the material, χ_m the magnetic susceptibility of the material, $\sigma$the electric conductivity in siemens per meter, ε the permittivity of the material and μ the permeability of the material. Subscripts *0* and *r* denote the free space and relative permittivity/permeability, respectively.

By rewriting Eqs. (4.6a), (4.7a), (4.8a) and (4.9a) by substituting Eq. (4.11) into respective equations, we obtain a set of Maxwell's equations that consist only 2 variables, which are *E* and *H* values.

$$\varepsilon \frac{\partial E}{\partial t} = \nabla \times H - \sigma E \tag{4.12a}$$

$$\mu \frac{\partial H}{\partial t} = -\nabla \times E \tag{4.12b}$$

$$\varepsilon [\nabla \cdot E] = 0 \tag{4.12c}$$

$$\mu [\nabla \cdot H] = 0 \tag{4.12d}$$

The constants of ε, μ and σ are scalars that are independent of time, position and field strength. The first equation of Maxwell's equations, Eq. (4.12a) implies that the changes of *E* field over a time step (time derivatives) is dependent on the changes of *H* field across a space step (curl). The second equation (Eq. 4.12b), on the other hand, which explains that magnetic field change in time is equal to the electric field variation in space. The divergence of *E* and *H* components in Eqs. 4.12c and 4.12d state that the net electric flux and magnetic flux out of any closed surface is zero, which means there is no free electric and magnetic charges within the space.

By expanding the vector components in curl operators of Eqs. (4.12a) and (4.12b) to scalar components in three dimensional rectangular Cartesian coordinates system, we will get the following partial differential equations:

$$\frac{\partial H_x}{\partial t}=\frac{1}{\mu}\left[\frac{\partial E_y}{\partial z}-\frac{\partial E_z}{\partial y}\right] \tag{4.13a}$$

$$\frac{\partial H_z}{\partial t}=\frac{1}{\mu}\left[\frac{\partial E_x}{\partial y}-\frac{\partial E_y}{\partial x}\right] \tag{4.13b}$$

$$\frac{\partial H_y}{\partial t}=\frac{1}{\mu}\left[\frac{\partial E_z}{\partial x}-\frac{\partial E_x}{\partial z}\right] \tag{4.13c}$$

$$\frac{\partial E_x}{\partial t}=\frac{1}{\varepsilon}\left[\frac{\partial H_z}{\partial y}-\frac{\partial H_y}{\partial z}-\left(\sigma E_x\right)\right] \tag{4.14a}$$

$$\frac{\partial E_y}{\partial t}=\frac{1}{\varepsilon}\left[\frac{\partial H_x}{\partial z}-\frac{\partial H_z}{\partial x}-\left(\sigma E_y\right)\right] \tag{4.14b}$$

$$\frac{\partial E_z}{\partial t}=\frac{1}{\varepsilon}\left[\frac{\partial H_y}{\partial x}-\frac{\partial H_x}{\partial y}-\left(\sigma E_z\right)\right] \tag{4.14c}$$

The six equations above give the detail time-space relationships between *E* and *H* field components, which are characterized by the three constants, μ, ε and σ respectively. These equations also form the basic algorithm for FDTD and will be used in development of Yee's algorithm for FDTD solution.

4.4.2 Yee's Algorithm for Three Dimensional Maxwell's Equations

This algorithm was first introduced by Yee [148] in 1966. A set of finite-difference equations was developed for the Maxwell's curl equations system which consists of partial differential equations (4.13) and (4.14) that were discussed in the previous section. As shown in Fig. 4.1, Yee defined a FDTD lattice unit cell in a three dimensional space. The space of solution is divided into a mesh of grid cells whereby the *E* and *H* field components are defined in each cell and staggered in space with *E* and *H* field components separated by one half of space cell. Each *E* field component is surrounded by four circulating *H* field components and vice versa.

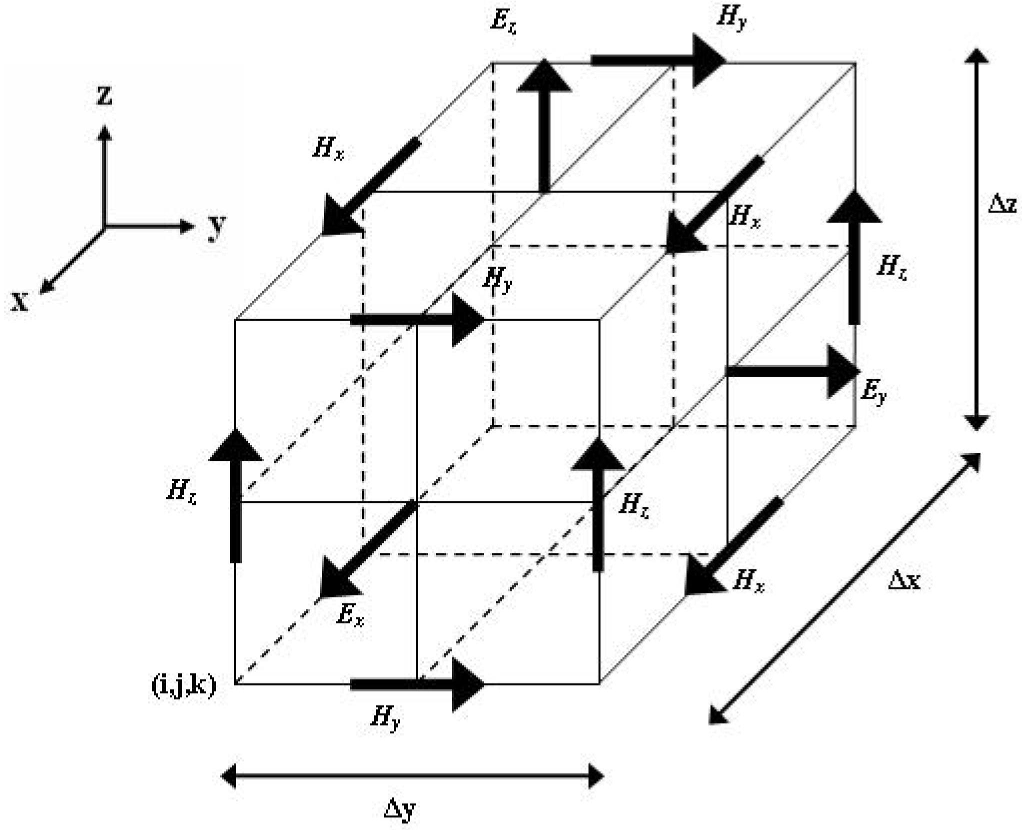

FIG. 4.3 Three dimensional unit cell of Yee's space lattice at the position of the electric and magnetic field components.

Considering a lattice with cell increment in *x*, *y* and *z* directions as *Δx*, *Δy* and *Δz*, the spatial cell point is denoted as

$$\left(i,j,k\right)=\left(i\Delta x,j\Delta y,k\Delta z\right) \tag{4.15}$$

and for time step of *Δt* the space-time function can be expressed as

$$F^{n}\left(i,j,k\right)=F(i\Delta x,j\Delta y,k\Delta z,n\Delta t) \tag{4.16}$$

where *i*, *j*, *k* and *n* are integers. Therefore the finite-difference expressions for both space derivatives at a fix time, *nΔt* and time derivative at a fix cell point, (*i*, *j*, *k*) can be expressed as

$$\frac{\partial F^{n}(i,j,k)}{\partial x}=\frac{F^{n}(i+\frac{1}{2},j,k)-F^{n}(i-\frac{1}{2},j,k)}{\Delta x}+O(\Delta x^{2}) \tag{4.17a}$$

$$\frac{\partial F^{n}(i,j,k)}{\partial t}=\frac{F^{n+\frac{1}{2}}(i,j,k)-F^{n-\frac{1}{2}}(i,j,k)}{\Delta t}+O(\Delta t^{2}) \tag{4.17b}$$

The expression of Eq. (4.17) illustrated the central differencing approximation that is in the second order accurate for spatial and temporal derivatives. In this case, Yee algorithm takes a central difference of ±1/2 increment in space and time coordinates (±1/2*Δx* and ±1/2*Δt*) instead of ±*Δ* due to the reason that it interleaves *E* and *H* field components at an interval of *Δ/2*. This allows a leapfrog algorithm and time stepping of field components to be implemented.

Applying the notation of Eqs. (4.17) to Maxwell's partial differential equations of (4.13) and (4.14), we will obtain a set of numerical solutions of Maxwell's equations as shown in Eqs. (4.15) and (4.16) for *E* and *H* fields interrelationship in a three dimensional space lattice [138,139,146].

Numerical solutions for Ampere Circuital Law:

$$\begin{aligned}E^{n+1}_{x(i,j,k)} &= \frac{2\varepsilon_{(i,j,k)}-\sigma_{(i,j,k)}\Delta t}{2\varepsilon_{(i,j,k)}+\sigma_{(i,j,k)}\Delta t}E^{n+1}_{x(i,j,k)}+\frac{2\Delta t}{(2\varepsilon_{(i,j,k)}+\sigma_{(i,j,k)}\Delta t)\Delta y}\left[H^{n+\frac{1}{2}}_{z(i,j+\frac{1}{2},k)}-H^{n+\frac{1}{2}}_{z(i,j-\frac{1}{2},k)}\right]\\ &\quad-\frac{2\Delta t}{(2\varepsilon_{(i,j,k)}+\sigma_{(i,j,k)}\Delta t)\Delta z}\left[H^{n+\frac{1}{2}}_{y(i,j,k+\frac{1}{2})}-H^{n+\frac{1}{2}}_{z(i,j,k-\frac{1}{2})}\right]\end{aligned} \tag{4.18a}$$

$$\begin{aligned}E^{n+1}_{y(i,j,k)} &= \frac{2\varepsilon_{(i,j,k)}-\sigma_{(i,j,k)}\Delta t}{2\varepsilon_{(i,j,k)}+\sigma_{(i,j,k)}\Delta t}E^{n+1}_{y(i,j,k)}+\frac{2\Delta t}{(2\varepsilon_{(i,j,k)}+\sigma_{(i,j,k)}\Delta t)\Delta z}\left[H^{n+\frac{1}{2}}_{x(i,j,k+\frac{1}{2})}-H^{n+\frac{1}{2}}_{x(i,j,k-\frac{1}{2})}\right]\\ &\quad-\frac{2\Delta t}{(2\varepsilon_{(i,j,k)}+\sigma_{(i,j,k)}\Delta t)\Delta x}\left[H^{n+\frac{1}{2}}_{z(i+\frac{1}{2},j,k)}-H^{n+\frac{1}{2}}_{z(i-\frac{1}{2},j,k)}\right]\end{aligned} \tag{4.18b}$$

$$\begin{aligned}E^{n+1}_{z(i,j,k)} &= \frac{2\varepsilon_{(i,j,k)}-\sigma_{(i,j,k)}\Delta t}{2\varepsilon_{(i,j,k)}+\sigma_{(i,j,k)}\Delta t}E^{n+1}_{z(i,j,k)}+\frac{2\Delta t}{(2\varepsilon_{(i,j,k)}+\sigma_{(i,j,k)}\Delta t)\Delta x}\left[H^{n+\frac{1}{2}}_{y(i+\frac{1}{2},j,k)}-H^{n+\frac{1}{2}}_{y(i-\frac{1}{2},j,k)}\right]\\ &\quad-\frac{2\Delta t}{(2\varepsilon_{(i,j,k)}+\sigma_{(i,j,k)}\Delta t)\Delta y}\left[H^{n+\frac{1}{2}}_{x(i,j+\frac{1}{2},k)}-H^{n+\frac{1}{2}}_{z(i,j-\frac{1}{2},k)}\right]\end{aligned} \tag{4.18c}$$

Numerical solutions for Faraday's Law of Induction:

$$\begin{aligned}H^{n+\frac{1}{2}}_{x(i,j,k)} &= H^{n-\frac{1}{2}}_{x(i,j,k)}+\frac{\Delta t}{\mu_{i,j,k}\Delta z}\left[E^{n}_{y(i,j,k+\frac{1}{2})}-E^{n}_{y(i,j,k-\frac{1}{2})}\right]\\ &\quad-\frac{\Delta t}{\mu_{i,j,k}\Delta y}\left[E^{n}_{z(i,j+\frac{1}{2},k)}-E^{n}_{z(i,j-\frac{1}{2},k)}\right]\end{aligned} \tag{4.19a}$$

$$\begin{aligned}H^{n+\frac{1}{2}}_{y(i,j,k)} &= H^{n-\frac{1}{2}}_{y(i,j,k)}+\frac{\Delta t}{\mu_{i,j,k}\Delta x}\left[E^{n}_{z(i+\frac{1}{2},j,k)}-E^{n}_{z(i-\frac{1}{2},j,k)}\right]\\ &\quad-\frac{\Delta t}{\mu_{i,j,k}\Delta z}\left[E^{n}_{x(i,j,k+\frac{1}{2})}-E^{n}_{x(i,j,k-\frac{1}{2})}\right]\end{aligned} \tag{4.19b}$$

$$\begin{aligned}H^{n+\frac{1}{2}}_{z(i,j,k)} &= H^{n-\frac{1}{2}}_{z(i,j,k)}+\frac{\Delta t}{\mu_{i,j,k}\Delta y}\left[E^{n}_{x(i,j+\frac{1}{2},k)}-E^{n}_{x(i,j-\frac{1}{2},k)}\right]\\ &\quad-\frac{\Delta t}{\mu_{i,j,k}\Delta x}\left[E^{n}_{y(i+\frac{1}{2},j,k)}-E^{n}_{y(i-\frac{1}{2},j,k)}\right]\end{aligned} \tag{4.19c}$$

In general, a new value of *E* or *H* fields at any lattice cell point is dependent on its previous respective value and the previous values of surrounding tangential field components. A field component is computed numerically at a time at any time step and it advances to one half of time step for another field component computation. This keeps going on until the simulation process is completed. Since all field components are assumed to be zero at the beginning of the simulation ($t = 0$), an incident wave source is defined before it enters the computation domain. The incident wave source can be a continuous wave (CW) or pulsed wave excitation. Yee's algorithm is more robust and straight forward because it solves both the *E* and *H* field components simultaneously in Maxwell's curl equations rather than solving them one by one by wave equations.

4.4.3 Numerical Stability and Mesh Truncation

The accuracy of FDTD method of Maxwell's equations depends on several factors. One of them is the numerical stability of Yee algorithm during the time stepping procedure [138,139,149]. The numerical stability requires the time increment, Δt defined in finite-difference expression in Maxwell's equations to be bound relatively to the lattice cell increment, Δx, Δy and Δz. This should satisfy the following relationship:

$$v\Delta t \le \frac{1}{\left[\frac{1}{(\Delta x)^2}+\frac{1}{(\Delta y)^2}+\frac{1}{(\Delta z)^2}\right]^{\frac{1}{2}}} \tag{4.20}$$

where v is the maximum phase velocity of the electromagnetic wave in the modeled region. For computational accuracy, the lattice cell increment should be the same whereby $\Delta x = \Delta y = \Delta z = \Delta$. Therefore, Eq. (4.12) is simplified as

$$\Delta t = \frac{1}{v\sqrt{\frac{3}{\Delta^2}}} = \frac{\Delta}{v\sqrt{3}} \tag{4.21}$$

Another factor that affects the FDTD system's stability is the boundary conditions where the lattice truncation method is employed. Since FDTD method is a volume based numerical method, the whole computational domain has to be discretized in order to achieve a numerical solution. However, when dealing with the geometries that are defined in an open region, the computational domain could be infinite or unbound. Due to the fact that it is impossible to simulate infinity spatial domain by considering the limited computer memory capacity, there is a need to define computational domain size by truncating it to a finite size. The truncation method enforces a boundary condition to the outer perimeter of the computational domain, which simulates the non-reflective nature of free space. It should allow the numerical wave propagating outward from computational domain to disappear at the lattice boundary without any reflection.

The most common truncation scheme used is absorbing boundary conditions (ABC), whereby the propagating wave is absorbed at the lattice boundary. Since 1980s, there were many researches on the physical and numerical approaches of ABC implementations [150-152]. A more recent approach of ABC-based truncation technique, which forms a perfectly matched layer (PML) at the boundary of computational domain [144,153-156]. PML is a lossy absorbing layer whose impedance matches that of free space and it absorbs any kind of wave at any frequency and at any incident angles without any reflection. An anisotropic PML is one of the PML boundary conditions that are based on Maxwellian formulation with the introduction of permittivity and permeability tensors s for three dimensional structures in spatial domain [155,156]:

$$\hat{\varepsilon} = \varepsilon \begin{bmatrix} s_y s_z s_x^{-1} & 0 & 0 \\ 0 & s_z s_z s_y^{-1} & 0 \\ 0 & 0 & s_y s_x s_z^{-1} \end{bmatrix} \tag{4.22a}$$

$$\hat{\mu} = \mu \begin{bmatrix} s_y s_z s_x^{-1} & 0 & 0 \\ 0 & s_z s_z s_y^{-1} & 0 \\ 0 & 0 & s_y s_x s_z^{-1} \end{bmatrix} \tag{4.22b}$$

where $s = \kappa - i\dfrac{\sigma}{\varepsilon_0 \omega}$. This medium gives a prefect attenuation of incident wave regardless of frequencies, polarizations and angle of incidence. Due to the reason that there might be significant reflection at the anisotropic PML interface, spatial scaling of the conductivity constant, σ is need in order to minimize it. The spatial variant is chosen in such at way that

$$\sigma = \sigma_{\max}\left(\frac{x}{L}\right)^m \qquad \text{and} \qquad \kappa = 1 + \left(\kappa_{\max} - 1\right)\left(\frac{x}{L}\right)^m \tag{4.23}$$

where L is the thickness of the anisotropic PML at each axis direction. m is the order o f the polynomial variation [155].

4.5 FDTD Simulation of Laser Irradiation through a Microlens Array

In this section, the implementation of the FDTD method to simulate the interaction of laser beam with microlens arrays will be introduced and discussed. Figure 4.4 shows the FDTD domain of computation with a microlens array is located at the free space. The incoming incident wave, which can be a pulsed or continuous wave excitation, is defined to propagate along *z* direction from *x*-*y* plane at $z = 0$. The microlens array is located at some distance from $z = 0$, parallel with *x*-*y* plane with its lens curvature surface facing +*z* direction.

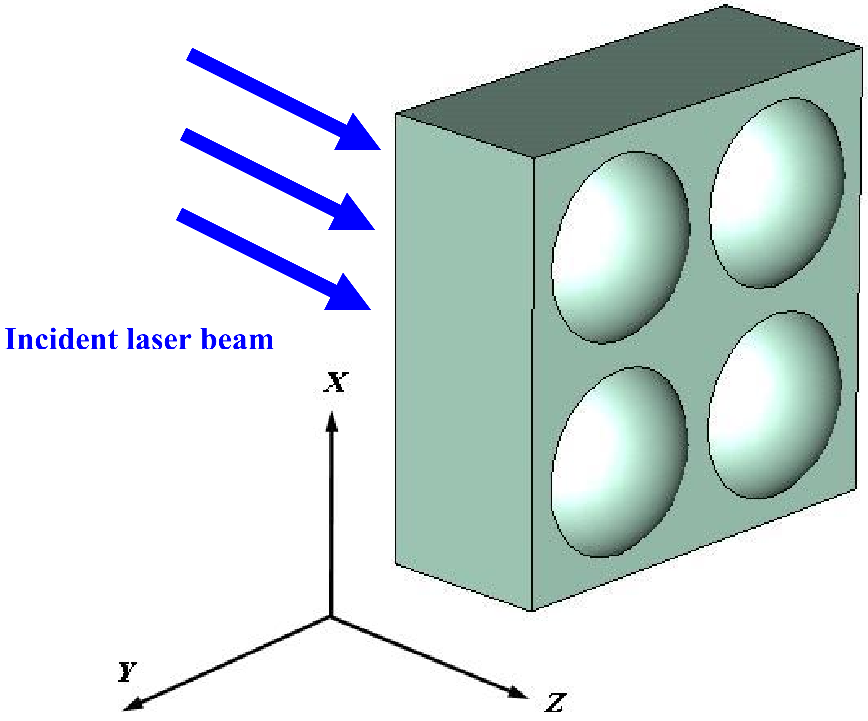

FIG. 4.4 The FDTD computational domain for laser irradiation of a microlens arrays in a three dimension free space region.

The free space is equivalent to air, therefore the permittivity and permeability are given as ε_0 and μ_0. Therefore, the partial differential equations (4.13a) and (4.14a) can be rewritten as

$$\frac{\partial H_x}{\partial t} = \frac{1}{\mu_0}\left[\frac{\partial E_y}{\partial z} - \frac{\partial E_z}{\partial y}\right] \quad \text{and} \quad \frac{\partial E_x}{\partial t} = \frac{1}{\varepsilon_0}\left[\frac{\partial H_z}{\partial y} - \frac{\partial H_y}{\partial z} - \left(\sigma E_x\right)\right] \tag{4.24}$$

The values of constants ε_0 and μ_0 are 8.85×10^{-12} farads per meter and $4\pi \times 10^{-7}$ henries per meter, respectively. Similar notation is applied to Eqs. (4.8b) – (4.9c) since the free space is considered as an isotropic, homogeneous and dispersionless medium.

As the incident wave propagates along the z direction, it starts to enter the region of microlens array. For a microlens array, the material is set as quartz which has refractive index n of 1.54. The permittivity of the microlens array is now changed to ε with its relationship with n as

$$\varepsilon = \varepsilon_0 \cdot \left(n\right)^2 = \varepsilon_0 \varepsilon_r \tag{4.25}$$

where ε the permittivity of quartz and ε_r the relative permittivity, which equals to n^2. For dielectric material, such as quartz, it is considered as non-permeable media, therefore $\mu = \mu_0$. The third constant, electric conductivity σ for both free space and quartz are set as zero since they are non-lossy mediums. The finite difference equations of (4.18a)-(4.19c) become simplified.

The output of the calculation can be viewed as E and H field distributions depending on the polarization direction or it can be presented in energy/power flux, Poynting vector, S. Poynting vector is the vector product of the E vector and the H vector given as

$$S = E \times H \tag{4.26}$$

Its unit is in watt per square meter, which describes the energy flow through a surface in terms of electric and magnetic properties and the vector point in the direction of the propagating electromagnetic wave.

4.5.1 Analysis of Focusing Ability of Microlens Array

The unique property of a microlens array is its ability to split an incoming incident light source into a series of tiny light spots. The simulation results obtained are used to examine its ability of focusing a collimated laser beam with a wavelength of 248 nm. As can seen from the Fig. 4.5, the 2 × 2 microlens array effectively focuses

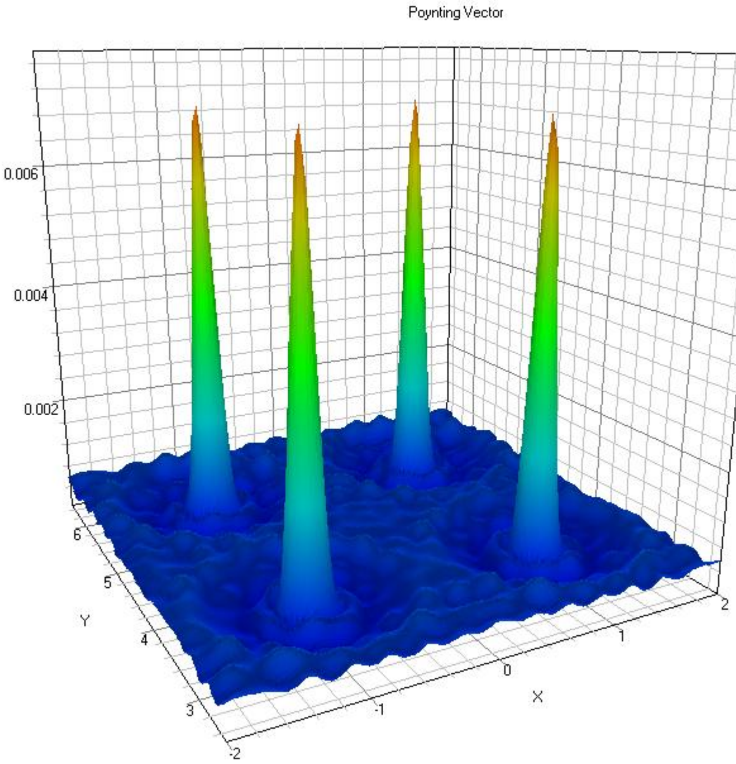

FIG. 4.5 The three dimensional Poynting vector plot with respected to the X-Y coordinate of the microlens array.

the laser beam into four equal intensity beam spots with its maximum Poynting vector value of 0.007 W/m^2.

At the focal plane, we observed an array of spots with a distance between 2 spots equal to the pitch of the microlens array. However, if the observation plane is away from the focal plane, different pattern arrays were observed as shown in Figs. 4.6 (a) – (d). A microlens array was illuminated with a coherent laser light and the image planes were captured using a microscope with a 40X objective lens and a color CCD camera. The images are compared with the simulation results and found to be identical to each other for some of the image planes. The images at these observation planes are different in terms of intensity distribution and pattern structures. However, the periodicity still remains the same. Such phenomenon is due to the several effects, such as interference, diffraction and divergence of the beam when it is propagated after the focal plane.

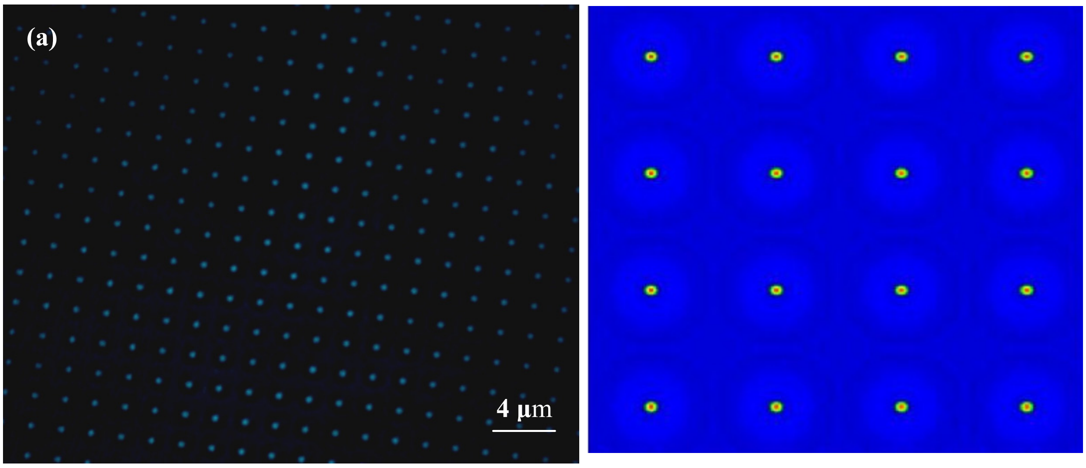

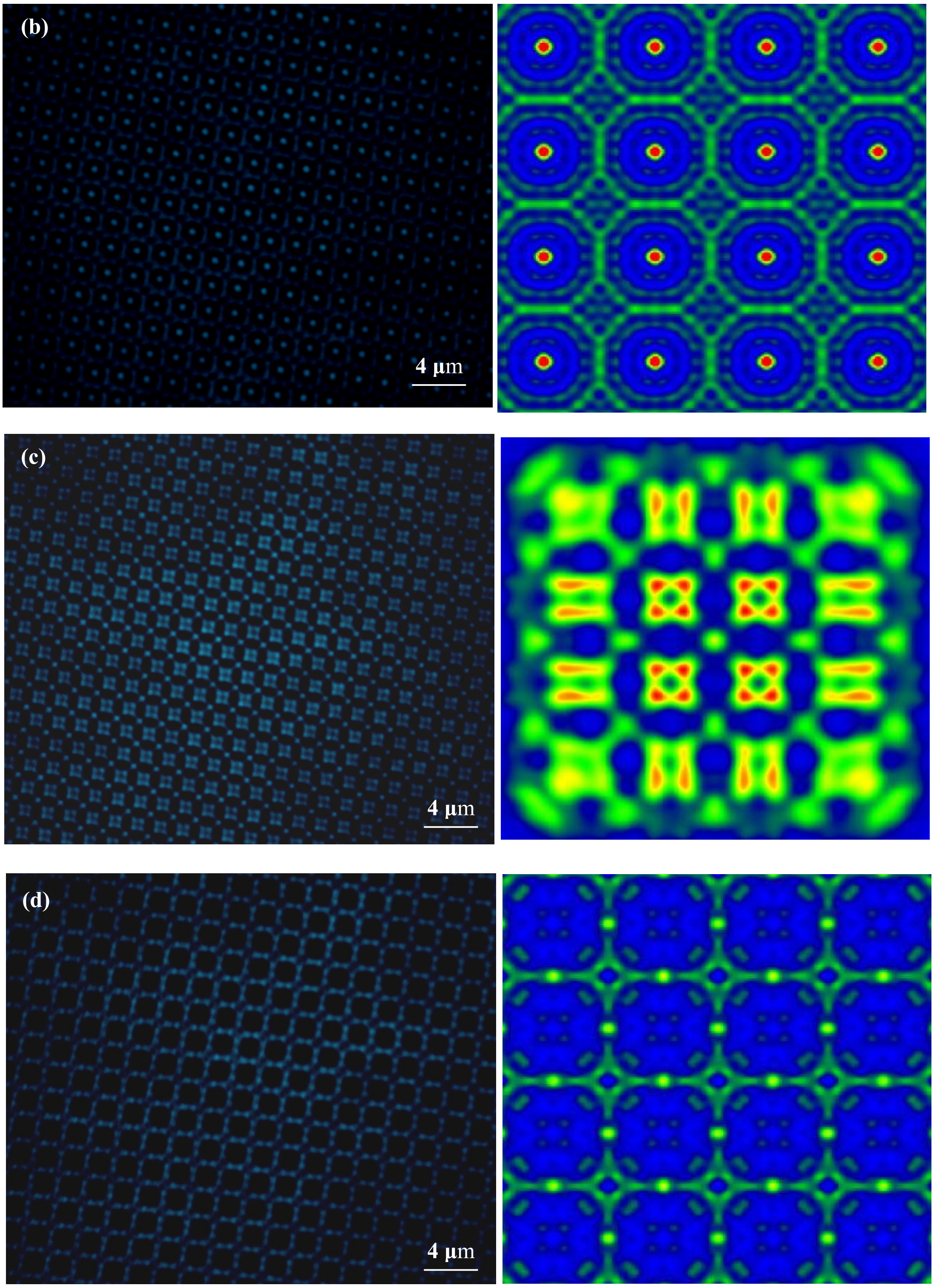

FIG. 4.6 Intensity distributions for different image planes of a laser illumination of a microlens array observed by microscope (left side) and FDTD simulations (right side).

4.5.2 Analysis of spot diameter with respect to sag height

By varying the different sag heights with reference to the microlens diameter, the intensity distribution of the laser light irradiation of the microlenses arrays at the focal plane is simulated. The microlens diameter is fixed at 1 μm while the sag height of the microlens is varied from 150 nm to 500 nm and the laser source chosen was 248 nm excimer laser at a repetition rate of 1 Hz.

Figure 4.7 shows the different intensity distributions obtained at the focal plane of the microlens arrays. Since the microlenses are symmetrical, we only took a single focus spot for analysis. The two dimensional intensity along the center of the microlens is plotted as shown in Figs. 4.7 (a) – (f). The FWHM of the focused laser spot and the maximum intensity was measured for each microlens sag height.

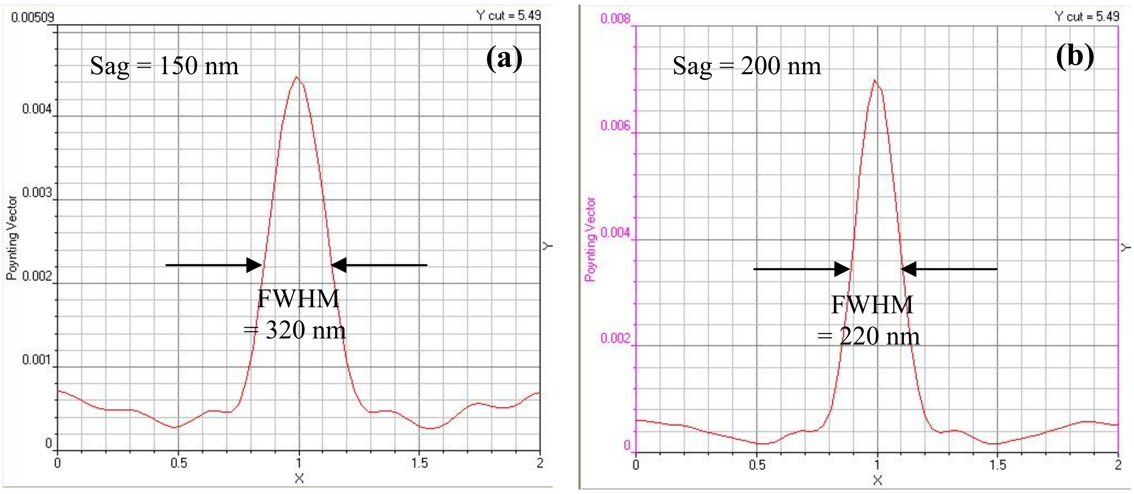

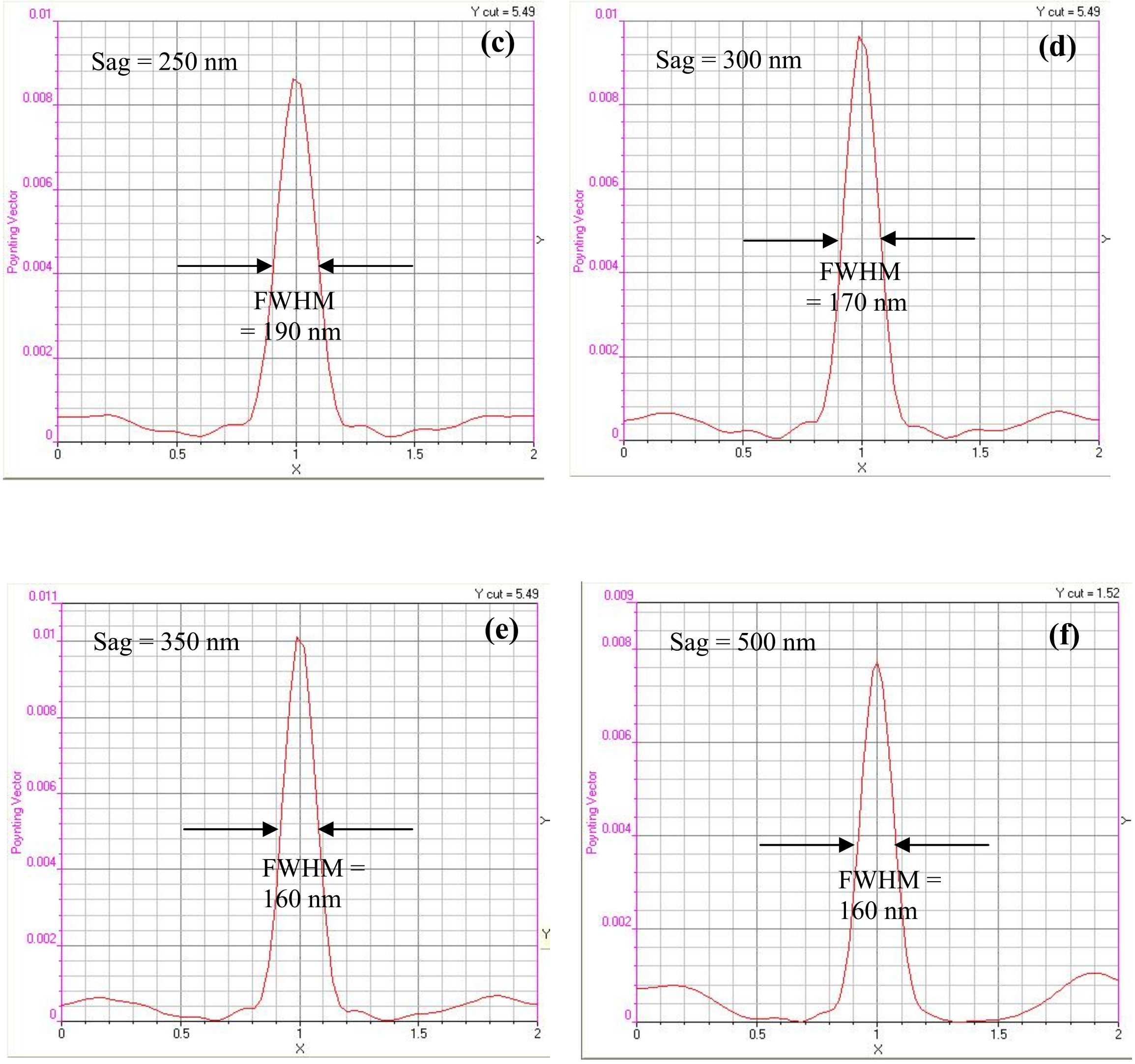

FIG. 4.7 Two dimensional intensity distributions of laser beam irradiation of different microlens sag heights.

As observed from Fig. 4.7, the FWHM increases when the sag height decreases. This can be explained by the optical diffraction limit whereby the minimum focus spot size is inversely proportional to the numerical aperture (NA) of the lens. Numerical aperture can be defined as ratio of microlens diameter to its focal length (*D/f*). As the sag of a microlens increases, the numerical aperture increases as well, thus the spot size decreases. As for the maximum intensity, when the spot size decreases, there is more energy confined per unit area thus the fluence increases. This can be observed from the Poynting vector plot in the simulation results shown in Figs. 4.7 (a) – (b). The results are summarized in Table 4.1 together with the calculated and measured focal lengths from the simulation results. The details of the intensity distribution are summarized in Table 4.1.

Table 4.1 Intensity distribution along center axis of microlens for different lens sag – diameter ratios.

Lens Sag-Diameter Ratio	**Focal Length (μm)**			**FWHM Value (nm)**	**Maximum Intensity**
	Measured	**Calculated**	**Delta**		
0.15	**1.682**	**1.674**	**0.008**	**320**	**0.00444**
0.20	**1.343**	**1.340**	**0.003**	**220**	**0.00710**
0.25	**1.157**	**1.104**	**0.053**	**190**	**0.00850**
0.30	**1.049**	**1.004**	**0.045**	**170**	**0.00975**
0.35	**0.985**	**0.949**	**0.036**	**160**	**0.01100**
0.50	**0.925**	**0.854**	**0.071**	**160**	**0.00790**

The next chapter will introduce the application of microlens array in maskless surface nanopatterning of identical periodic nano-features. The experimental setup and mechanism of nanopatterning will be revealed. The results obtained by using laser irradiation through a microlens array are discussed. Finally, some potential applications of this surface nanopatterning technique are recommended.

CHAPTER 5

SUB-MICRON SURFACE NANOPATTERNING BY LASER IRRADIATIONS THROUGH MICROLENS ARRAYS

5.1 Introduction

5.1.1 Review on surface nanopatterning

The advance in nanoelectronics, nanophotonics and data storage technology has stimulated the development of surface nanostructuring techniques. In recent years, surface nanopatterning has emerged as one of the areas of interest in scientific researches due to the rapid development in microelectronics components and MEMS devices fabrication. As the electronic devices nowadays are getting smaller and more compact, the miniaturization of these components requires large scale and fast speed patterning techniques in micro and sub-micron range of resolution.

In recent years, various techniques in performing sub-micron patterning have been extensively investigated and reported. One of the most commonly used techniques is lithographic technique which involves the replication of patterns on photoresist through light irradiation and transfer to the substrate by etching process. Optical lithography, or commonly known as photolithography, utilizes a light source to print patterns on a mask onto a photoresist by photochemical reaction. The resolution of this lithographic technique is controlled by the optical diffraction limit. According to Abbe's optical diffraction limit for far-field optics [157], the lateral resolution of a focused light beam r is related to the wavelength of the incident light λ and optics numerical aperture NA.

$$r = 1.22\frac{\lambda}{NA} \tag{5.1}$$

Over the decades, many researches have been carried out to develop various novel surface nano-patterning techniques to overcome this problem. As can be seen from Eq. (5.1), the optical diffraction limit can be overcome by either reducing the wavelength of the light source λ or by increasing the optic's numerical aperture NA, such as Deep UV lithography [158,159] and near-field scanning optical lithography (NSOL) [160,161]. On the other hand, different types of non-optical lithographic techniques, such as X-ray lithography [162,163], E-beam lithography [164,165] and nanoimprinting lithography [166,167], are also capable to produce patterns in nanometer scale. However these lithographic techniques suffer from either high setup cost or low throughput that concerns the manufacturing industry.

5.1.2 Laser micro and nanoprocessing

Laser processing is one of the promising tools in non-contact material processing that gives the advantages of low cost and is suitable for processing different kinds of materials. Conventional laser processing technique by focusing the laser light through a focusing lens can achieve features in micron range [168-170]. The high intense laser energy enables one to perform numerous materials processing by laser ablation. Therefore, two and three dimensional micro-structures can be generated by applying the intense laser beam to the material and controlling the toolpath of the laser beam. For laser surface nanostrucuring, microsphere nanopatterning [171,172] is a laser-induced highly localized surface modification by simply focusing laser light onto the substrate through a layer of self-assembly micro-particles. The particles are capable of enhancing the laser intensity at a near field region of a few tenth of nanometer. This technique has been promising and capable of producing sub-micron periodic patterns directly on a substrate over a large area uniformly. However, the major drawbacks are the difficulty in controlling the particle arrangement, the existence of bi-layer of particles and the impossibility of particles re-use.

In this chapter, a hybrid surface sub-micron patterning method of combing the laser and microlens arrays (MLA) has been proposed. MLA is one of important microoptics components that consist of a series of miniaturized lenses with same size and focal length. These lenses are arranged in a certain form of order [3], mostly hexagonally or squarely packed and spherical or cylindrical in shape. As compared to normal single lens in a typical optical system, MLA focuses an incident light and forms a series of parallel light spots at the focal plane [173,174]. By illuminating laser beam through a MLA, sub-micron patterns are produced efficiently on photoresist through the lithographic method. This surface nanopatterning technique is similar to that using a monolayer of micro-particles, which can generate thousands to millions nanopatterns (depending on the size of the MLA and also the numbers of microlenses) by a single or multiple pulses. However, due to the non-contact nature of the MLA surface nanopatterning, it gives the advantages over microsphere nanopatterning in term of repeatability of the process and the reusability of the MLA as compared to micro-particles.

5.2 Experimental details

5.2.1 Sample preparation

The sample used in this experiment was silicon substrate coated with a layer of photoresist. Before the silicon substrate can be used, it was first cleaned in the ultrasonic bath by isopropanol solvent (IPA) and de-donised water (DI water) to remove particle and organic contamination. After the silicon susbtrate was cleaned, a layer of adhesion promoter, such as HMDS with a thickness of a few nm, was coated on the substrate. Two types of photoresists were used in this experiment, Microresist ma-P 1205 UV photoresist and Shipley UV 54 deep UV amplified photoresist. Both photoresists have sub-micron resolution, which make them suitable for surface nanopatterning applications. The photoresist was spin coated on the substrate at a spin speed of 6000 rpm to obtain a resist thickness of about 400 nm. The coated sample was then put on a hotplate to bake the photoresist at a temperature of 90 – 100 °C in order to remove the moisture.

5.2.2 Microlens arrays used for surface nanopatterning

Figures 5.1 (a) and (b) show the MLAs used in this experiment, a hexagonally packed MLA and a squarely pakced MLA, both made of quartz that were used to perform the patterning process. For the hexagonally pack MLA, the pitch between 2 lenses is 25 μm with a diameter of 23 μm and sag of 9 μm. There were totally 401 x 401 lenses covering an area of 1 cm^2, which is equivalent to 160,000 focused light spots at the focal plane when illuminated by a laser source. For the squarely pack MLA, the pitch is 2 μm with a diameter of 1 μm over an area of 5 mm x 5mm, which corresponds to 6,250,000 of microlenses. Figure 5.2 shows the schematic drawing of basic principle of MLA patterning on photoresist. A single incident laser beam source passed through the MLA and focused by each individual microlens due to the refraction. The focusing of the incoming laser beam by the microlenses divides the single beam into multiple tiny focused laser beams at the MLA focal plane, with the distance between 2 laser beams mimicking the pitch of the MLA. When a sample with photoresist coated on it was place

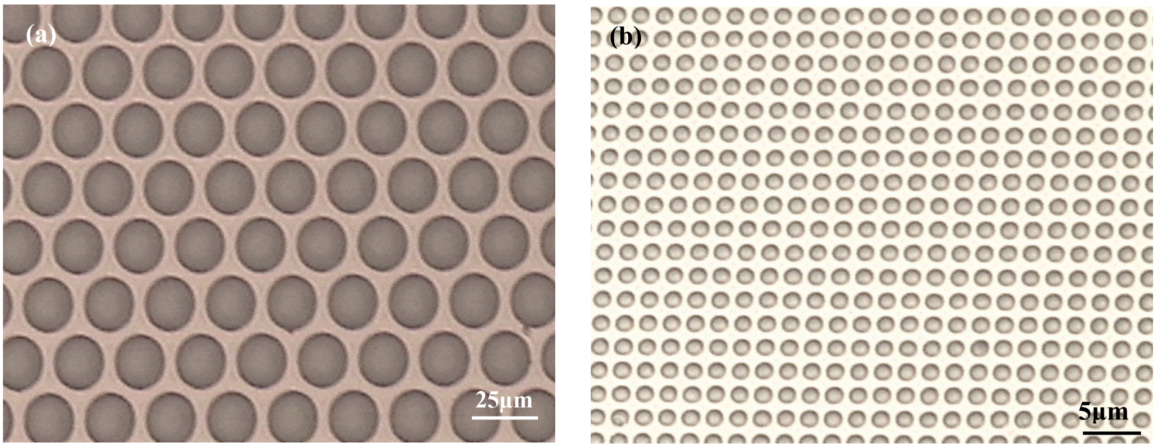

FIG. 5.1 (a) hexagonally and (b) squarely packed microlens arrays used for laser surface nanopatterning.

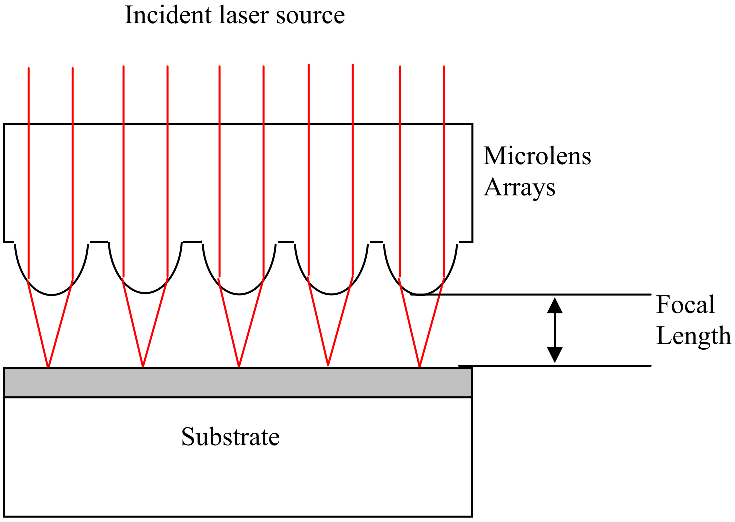

FIG. 5.2 Schematic drawing of working principle of MLA nanopatterning. Each microlenses focuses the incident light into a small spot at the focal distance.

at the focal plane, sufficient laser intensity and irradiation time change the chemical properties of the photoresist material. This exposed material reacts with developer and is dissolved away, thus generating a series of periodic patterns.

5.2.3 Experimental setup

The laser systems used for the exposure are Ti:Sapphire second harmonic generation femtosecond laser (Spectra Physics Tsunami, Mode 3960, λ = 400 nm, τ = 100 fs, repetition rate = 82 MHz) and KrF excimer laser (Lambda Physik LEXTRA 50, λ = 248 nm, τ = 23 ns, repetition rate = 1 Hz). The laser emits from the laser head and passes through a beam splitter or an attenuator before it is directed to the reflective mirror for irradiation through the MLA. The purpose of beam splitter/attenuator is to reduce the laser energy going into the system. In order to control the distance between sample and MLA, the laser was coupled with a precision XYZ translation nanopositioning stage with NC control as shown in Fig. 5.3. A high resolution precision Z stage was needed in order to maintain a consistent gap distance between the MLA and the sample. This was achieved by using a piezo actuator, which has a closed loop resolution of 5 Å. The system also enables lines and dots with a distance other than the pitch of 2 μm to be patterned on the photoresist by moving the stage in X-Y directions during the exposure. The patterned samples were then characterized by a high resolution optical microscope, scanning electron microscope (SEM) and atomic force microscope (AFM) for their 2D and 3D surface profiles.

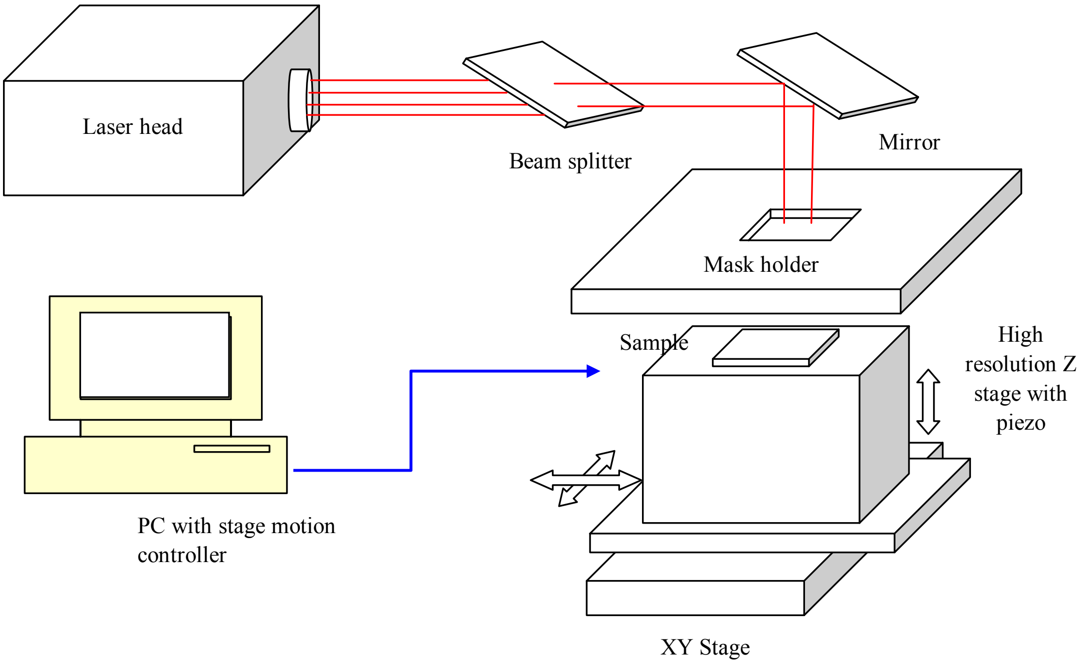

FIG. 5.3 Nanopositioning system used to control Z height during the nanopatterning process.

5.3 Surface nanopatterning by femtosecond laser

5.3.1 Sub-micron patterns

Sub-micron periodic nanopatterns can be generated by simply irradiating the MLA with laser and moving the sample close to the focal plane. Figure 5.4 shows the image of a sample after exposure at a laser fluence of 12.3 mJ/cm^2 by the femtosecond laser. As it can be seen from the image, the measured average pattern size is 410 nm and the distance between 2 dot patterns is measured at about 25 µm, which is equivalent to the pitch of the lenses. This can be attributed to the patterning which was done at the focal distance by the MLA. The focal length of a MLA f is the distance whereby the laser source is focused to the smallest spots by the lenses and has the highest laser fluence. The focal length of the MLA depends on the radius of curvature

R of the lens surface, sag height h and radius r of the lens, which can be calculated from the Eqs. 5.2 and 5.3 [175].

$$f = \frac{R}{n-1} \tag{5.2}$$

$$R = \frac{h^2 + r^2}{2h} \tag{5.3}$$

The radius of the fused silica lens is 11.5 μm and sag is 9 μm, which corresponds to R of 11.86 μm and f of 28.7 μm. When the laser irradiates through the MLA, large numbers of tiny focused laser beams form at the plane parallel to the sample surface at a distance equal to the focal length. The focal plane was obtained by using a spacer. Due to the intense laser energy at the focal point, the photoresist absorbs the laser energy and changes its chemical property so that the developer solution only dissolves photoresist in the exposed areas.

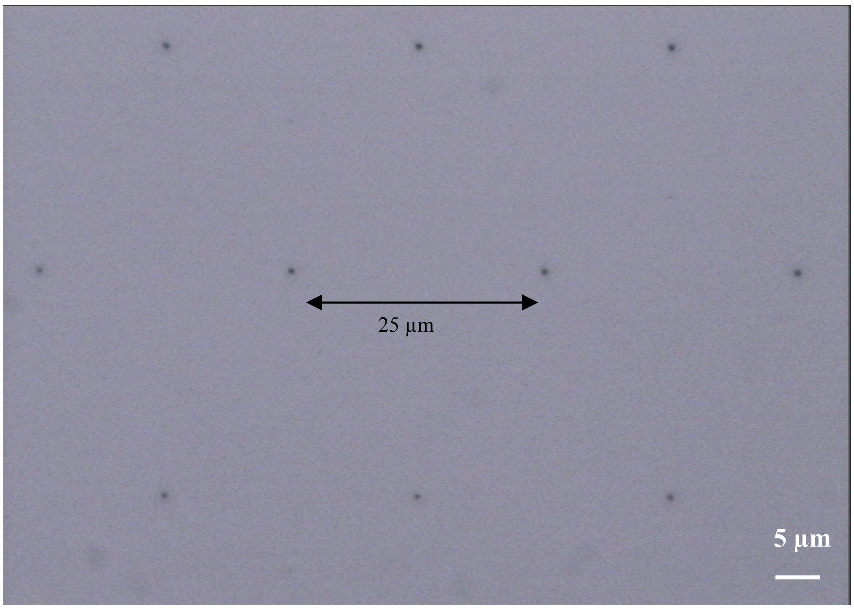

FIG. 5.4 Dots arrays patterns on the photoresist after exposure using MLA at the focal plane.

5.3.2 Influence of laser pulse number

The nanopattern feature size can be altered by changing the exposure conditions. Figure 5.5 shows the influence of exposure time to the size of patterns after development at a laser fluence of 3.2 mJ/cm^2. The exposure time was varied from 1 second to 6 seconds and the sizes of the patterns were measured by a high resolution microscope. It can be found that the pattern size increases with exposure time. The laser system used was a pulsed laser at a repetition rate of 82 MHz, which means there were 82 x 10^6 pulses of irradiation in one second. Therefore, as the exposure time increases, the pulse number also increases; thus more energy is supplied to the photoresist.

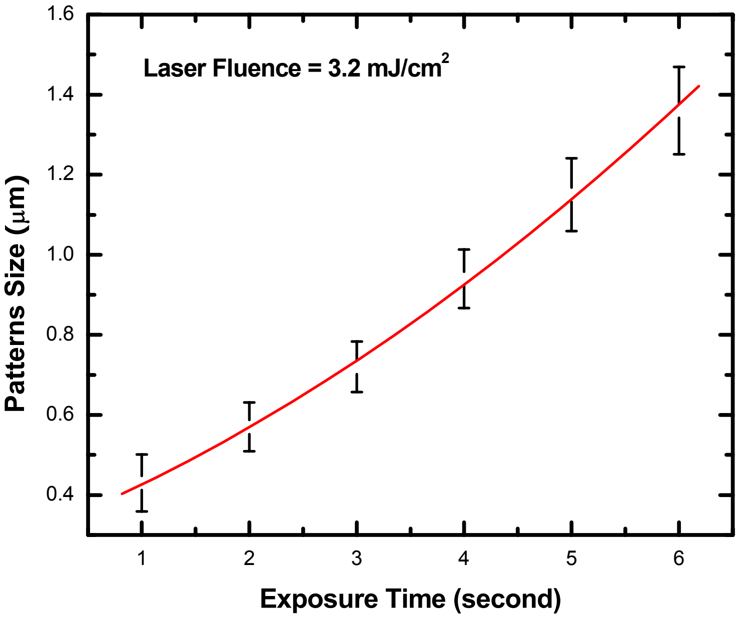

FIG. 5.5 Dependence of the pattern size on the laser irradiation time at a constant laser fluence of 3.2 mJ/cm^2.

This subsequently causes the exposed area to become bigger and as a result pattern size becomes bigger. The increase of patterns size with exposure time is not linear due to the effect of ultra-high peak power of the laser pulse and the non-linear adsorption phenomenon of the femtosecond laser light when it interacts with the photoresist material during photochemical reaction process.

5.3.3 Influence of laser fluence

The pattern size is highly dependent on the laser irradiation energy as well as the exposure time. As the laser fluence increases, the pattern size increases. However, when the laser fluence is too high, exceeding the ablation threshold, the photoresist is ablated away instead of reacting photochemically, leaving holes with a diameter of a few microns. The minimum spot size that can be focused by a lens is described by Eq. 5.4,

$$d_{\min} = \frac{4M^2 \lambda f}{\pi d_0} \tag{5.4}$$

In this case, the wavelength of the femtosecond laser λ is 400 nm, focal length of the MLA f is 28.7 µm and the size of incoming light source, d_0 equal to the lens diameter 23 µm. Assuming that the laser is a perfect Gaussian beam and therefore M^2 is equal to 1, it gives d_{min} of 636 nm. Figure 5.6 shows the 2D profile obtained by an AFM on two different patterns exposed at different laser fluences of 12.6 mJ/cm^2 and 4.1 mJ/cm^2, respectively. For Fig. 5.6 (a), the pattern feature size was 635 nm with its full width at half maximum (FWHM) of 439 nm, which was very close to the calculated d_{min} value. However as the laser fluence was further decreased, pattern size can be further reduced to 340 nm with the FHWM of 274 nm, as shown in Fig. 5.6 (b). This could be due to lower laser fluence that leads to the less energy absorbed by the photoresist and only the area at the top photoresist layer to be resolved by the developer. The other reason was the multi-photon absorption characteristic of extremely high peak power induced by the ultrashort laser pulse duration (100 fs).

The pattern profiles reassemble a valley shape with the deepest point at the center of the pattern. This is due to the Gaussian beam profile of the femtosecond laser source whereby its power intensity is the highest at the center of the beam and gradually reduced from the beam center. When the focused laser beam was irradiating on the photoresist surface, the center of the focused beam gives the most energy that is absorbed by the photoresist material.

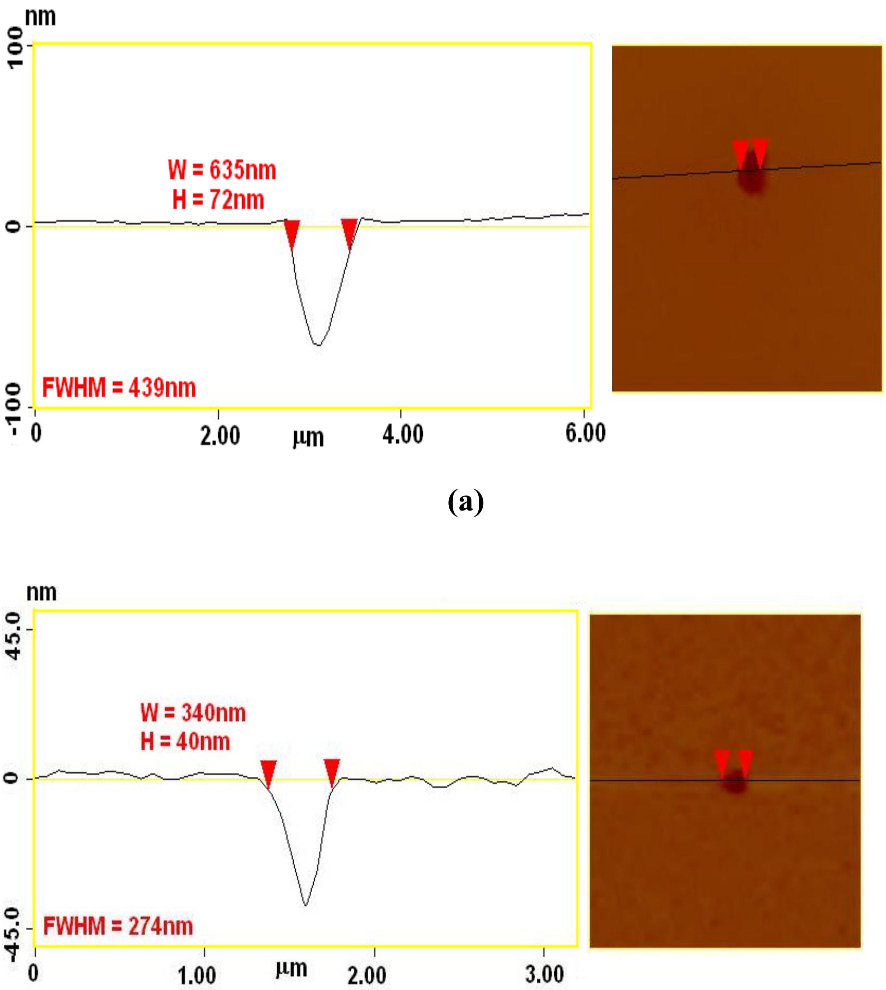

(a)

(b)

FIG. 5.6 AFM profiles of patterns exposed at laser fluences of (a) 12.6 mJ/cm^2 and (b) 4.1 mJ/cm^2, respectively.

5.3.4 Fractional Talbot effect

When the sample was exposed at the focal plane of the MLA, the pattern arrays generated after resist developed re-assemble the pitch of the lenses. However, if the sample was exposed at the distance that is not equal to the focal length of the lenses, more complicated patterns can be observed. This is because the laser light coming out from the each of the lenses acts as an individual point source and interferes with other adjacent lenses. This creates complex periodic patterns with different light distributions. At different distances from the focal plane, the patterns generated have different light distributions. This phenomenon was first described by Talbot [176**Error! Reference source not found.**] in 1836 for all periodic structures, such as interference of light through a grating. Besold et. al. [177,178] further investigated and explained this phenomenon appeared in microlens arrays.

The fractional Talbot effect for a MLA plane explains that for a distance away from the focal plane multiplied foci can be observed on the plane parallel to the focal plane. The fractional Talbot distance z is described as M/N z_T, whereby z_T is the Talbot length while M and N are non-negative integers [178]. When the Talbot plane is 0, it is at the focal length of MLA and the pattern obtained is exactly the replication of the foci of MLA as shown in Fig. 5.1. Figures 5.7 (a)-(c) show the patterns with multiplied foci at different fractional Talbot planes. As can be seen from the figures, there were several other ‘sub-foci’ surrounding the foci of the focal plane. The amplitude function in a plane parallel to the focal plane at $z = z_0$ can be calculated with the method of the propagation of the angular spectrum of plane waves (Eq. 5.5):

$$u(x.y.z=z_0)=\int_{-\infty}^{+\infty}\int_{-\infty}^{+\infty}\tilde{u}(v_x,v_y)\exp[2\pi i\frac{z_0}{\lambda}\sqrt{1-\lambda^2({v_x}^2+{v_y}^2)}] \times\exp[2\pi i(v_x x+v_y y)]\mathrm{d}v_x\mathrm{d}v_y \tag{5.5}$$

where λ is the wavelength of the light, v_x and v_y spatial frequencies and the function is the Fourier transform of $\tilde{u}(v_x,v_y)$. The wave amplitude in a fractional Talbot plane therefore can be expressed as:

$$u\left(x,y,z=\frac{M}{N}z_T\right)=\exp[2\pi i\frac{Mz_T}{N\lambda}]\sum_{k=-\infty}^{+\infty}\sum_{l=-\infty}^{+\infty}F_{k,l,M,N}A\left(x-k\frac{p}{N},y-l\frac{p}{N}\right) \tag{5.6}$$

The complex factor F in Eq. 5.6 is responsible for the multiple foci at the fractional Talbot plane. The numbers of multiplied foci depend on the location of sample, which is the Talbot distance. For ½ and 1 Talbot planes there are not multiplied foci but the intensity of these planes is not the same as that at focal plane. The phenomenon of multiplied foci at the fractional Talbot plane is useful for patterning substrate that requires high density of patterns per unit area (higher than the density of microlenses on the MLA) with only a single exposure. However the non-uniformity of the intensities of the multiplied foci in the fractional Talbot planes could be the limitation to its applications.

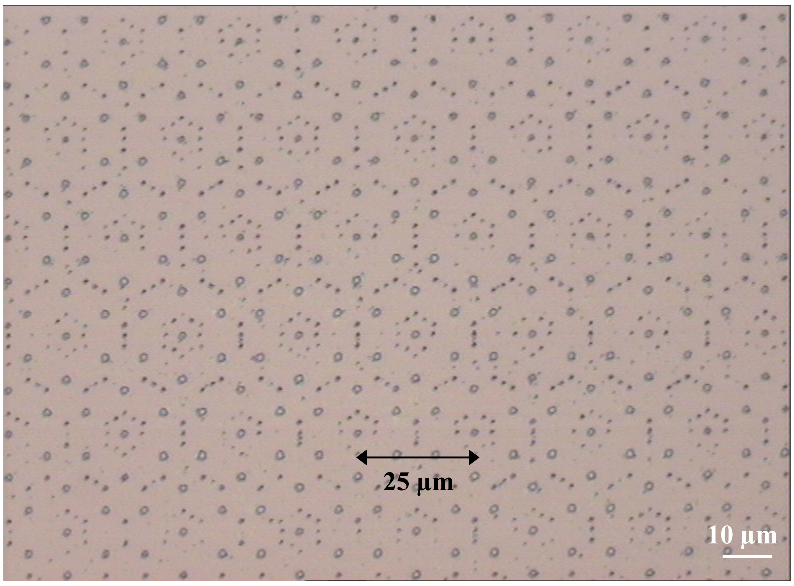

(a)

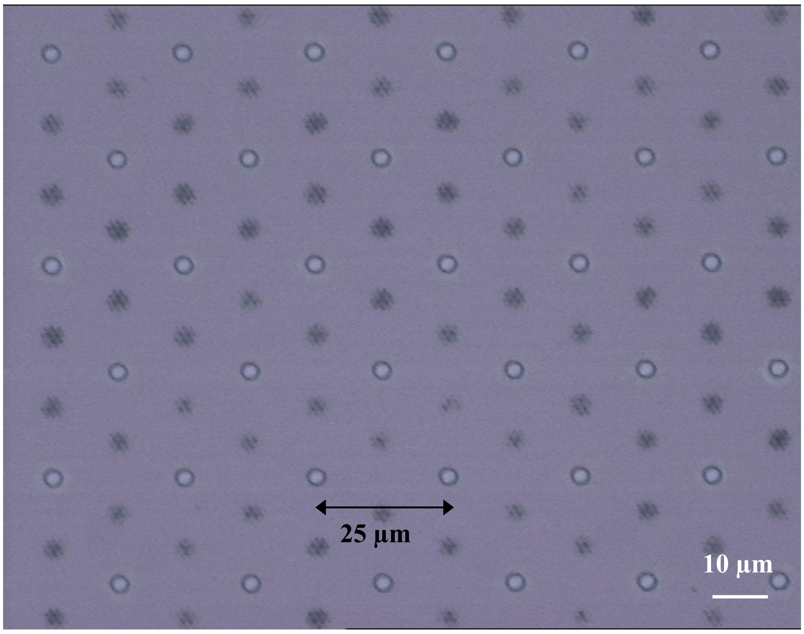

(b)

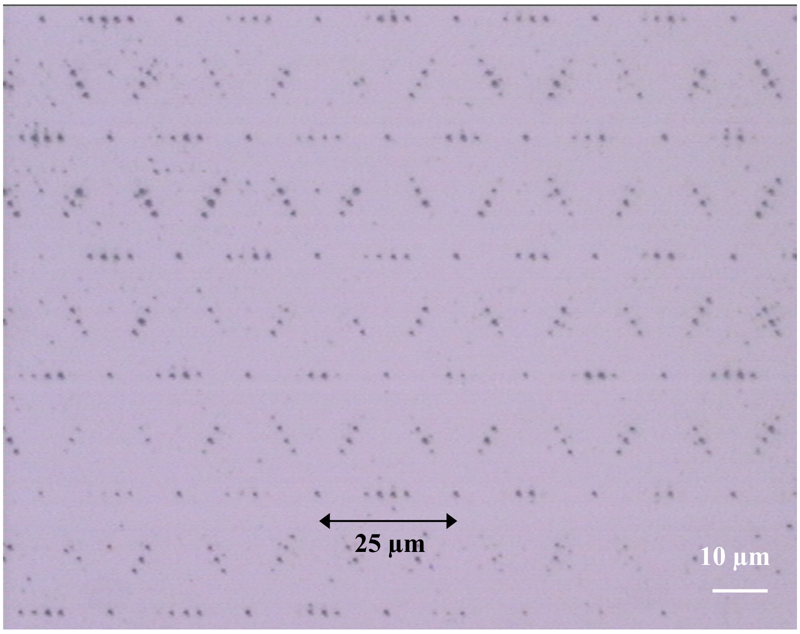

(c)

FIG. 5.7 Multiplied foci patterns on photoresist caused by the fractional Talbot effect at different fractional Talbot planes.

5.3.5 Arbitrary pattern fabrication by moving the XY stage

Single exposure at the focal plane enables patterning of features with a period equal to the pitch of MLA only. Fractional Talbot plane effect does not allow one to pattern any desired features. The unequal intensity of multiple foci may give unequal patterns dimension. Hence, in order to pattern other periodic structures, the NC controlled moving X-Y stage was used to carry out multiple exposures at the MLA focal plane. The patterning was done by controlling the steps of the stage movement as well as the traveling speed of the stage. Figure 5.8 shows two different pattern structures patterned by coupling the MLA to the X-Y stage. Figure 5.8 (a) was a dot array with a period of 2.5 µm exposed at a laser fluence of 5.4 mJ/cm^2. The average feature size was measured at 589 nm. To achieve such squarely arranged array of patterns, the stage was programmed to move 2.5 μm and shutter was open to expose the sample. This was repeated by moving the stage horizontally and vertically until all the areas were exposed. As the feature size is affected by the exposure time, to control the duration of shutter open enables the control of the desire feature size.

Figures 5.8 (b) shows another array of patterns created using the MLA. Each lens of MLA patterned 4 rows of uniform line patterns. The length of each line was 20 μm and average width of 760 nm. For the line patterns, the width of the line is controlled by the stage moving speed since the shutter was remained open during the patterning process. The MLA acts as a series of ‘light’ pens, which ‘drew’ thousands of same features simultaneously. Figure 5.9 shows the AFM image obtained by scanning the sample in Fig. 5.8 (a). It was shown that the dots were uniformly distributed with an average depth of 92 nm.

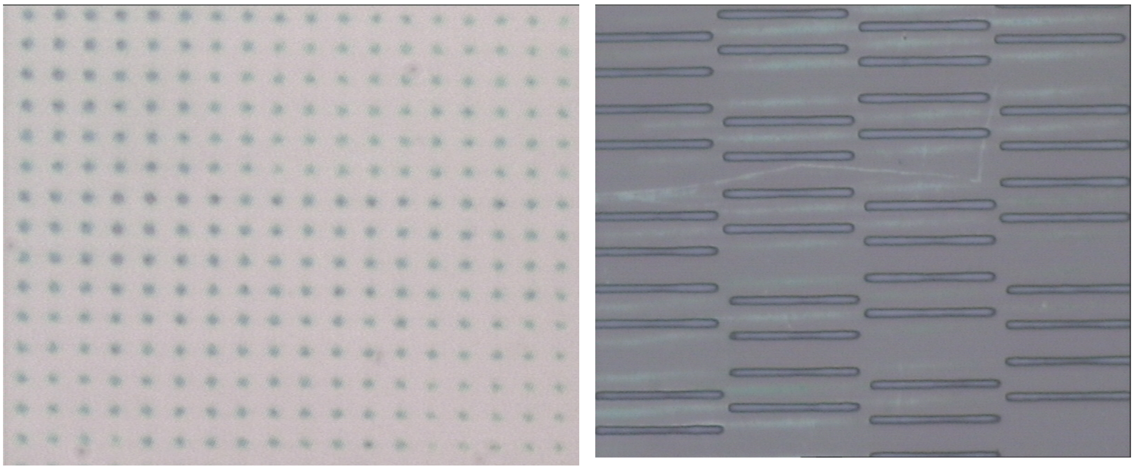

(a) **(b)**

FIG. 5.8 MLA patterning of (a) dot arrays and (b) line arrays by coupling the MLA to X-Y precision stage.

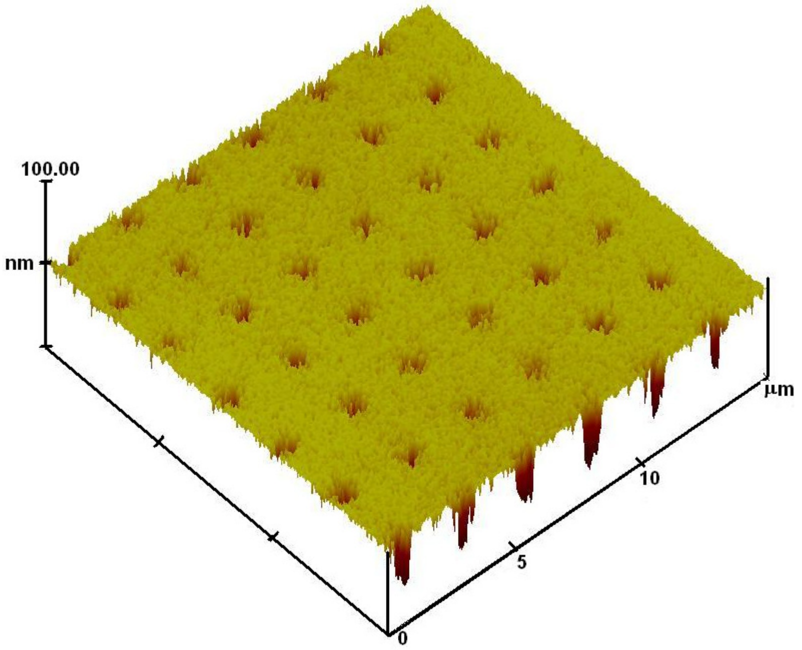

FIG. 5.9 AFM profile of dot arrays with a period of 2.5 µm by moving the X-Y stage at a step size of 2.5 µm vertically and horizontally.

5.3.6 Pattern transfer onto substrate

Reactive ion etching (RIE) was used to etch the samples to transfer the patterns onto the substrate. The advantages of RIE are that it has high etching selectivity and is suitable to etch silicon. Figure 5.10 (a) shows the AFM image of a sample that the resist has been stripped away after the RIE. The etching was done using CF_4 with a flow rate of 55 sccm for 5 minutes. The depth of the etched pattern was 68 nm and width of 845 nm. Figure 5.10 (b) shows another etched sample with patterns similar to the one shown in Fig. 5.7 (c). From both figures, it was found that both etched samples have patterns arrangement similar to those after being exposed. It has been demonstrated that the periodic features patterned by the MLA can be successfully transferred to the substrate by RIE. By changing the etching time and etchant's flow rate, the depth of the patterns can be altered.

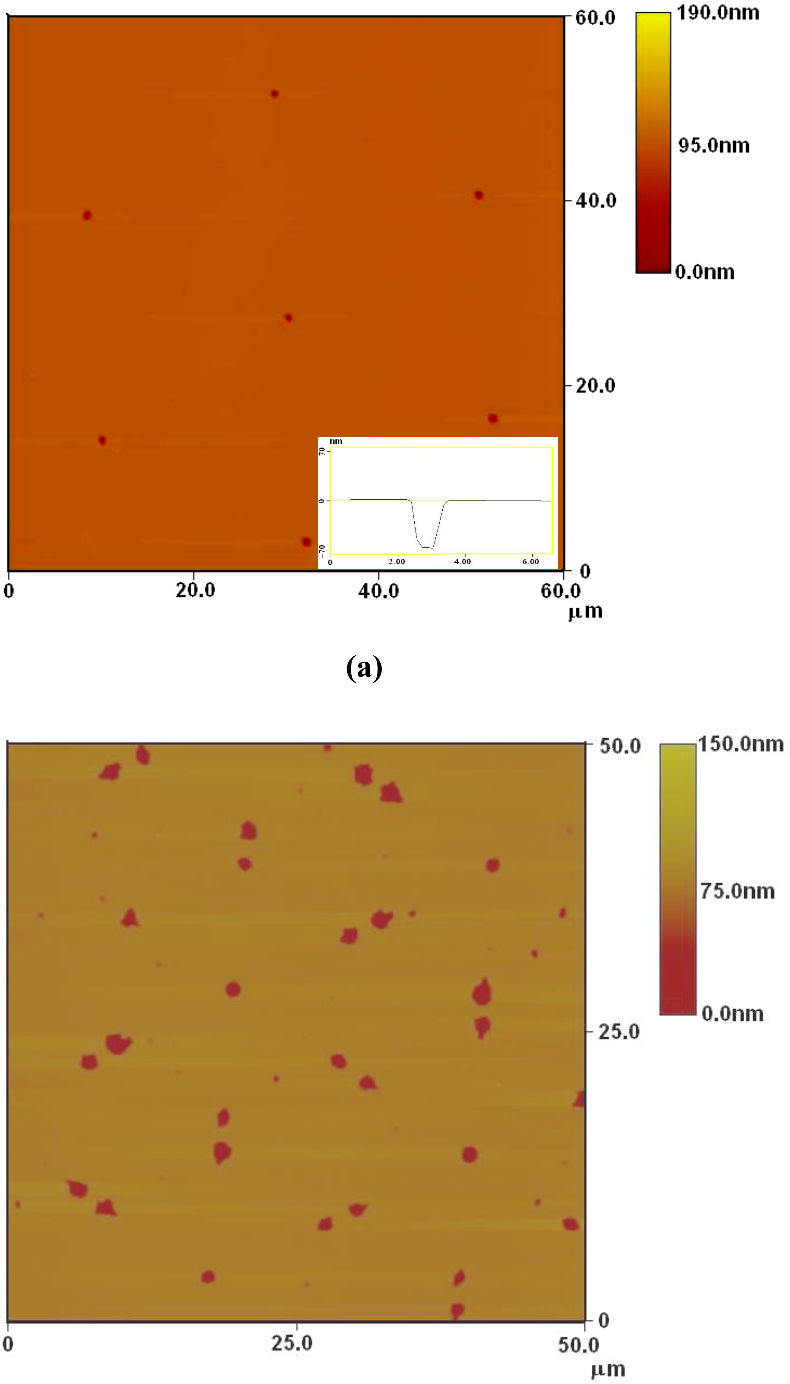

(a)

(b)

FIG. 5.10 Reactive ion etching (RIE) of samples with patterns exposed at (a) focal plane and (b) fractional Talbot planes.

5.4 Surface nanopatterning by nanosecond laser irradiation

5.4.1 Single pulse nanopatterning

Figure 5.11 shows the SEM images of the array pattern generated after the laser irradiation through the MLA (pitch = 2 μm, diameter = 1 μm) using a 248 nm KrF excimer laser. During the surface nanopatterning process, the sample was brought to the focal plane of the MLA with the highest intensity at this point. The MLA used has a diameter of 1 μm and sag height of 270 nm, which gives a focal length of ~ 1.1 μm. By varying the distance between the sample and the MLA, an array of periodic nano-dot patterns was created after the photoresist was developed. In Fig. 5.11 (a), an array of dot structures with a diameter of 400 nm formed at a laser fluence of 45 mJ/cm^2 was observed. Each individual hemispherical microlens refracted the laser light and focused it into a small light spot. As it was a photo-chemical reaction process involved under UV laser irradiation, the photo-polymer material underwent a chemical transformation at the point where the intensity of light irradiation was above the exposure threshold. Therefore, only those areas at the focal points where the photo-polymer had undergone chemical change were soluble to the developer for the formation of nano-dot arrays. The same phenomenon is shown in Fig. 5.11 (b) but with a nano-line array from the cylindrical lenses structure. The width of the lines is 300 ± 12 nm formed at a laser fluence of 38 mJ/cm^2.

Figure 5.12 shows the AFM three and two dimensional cross section profiles of a sample patterned at a laser fluence of 15 mJ/cm^2. The distance between two neighboring dot patterns is 2 μm, which is equivalent to the lens pitch of the MLA. The average dot size is 185 nm measured at its full width at half maximum (FWHM), 82% reduction as

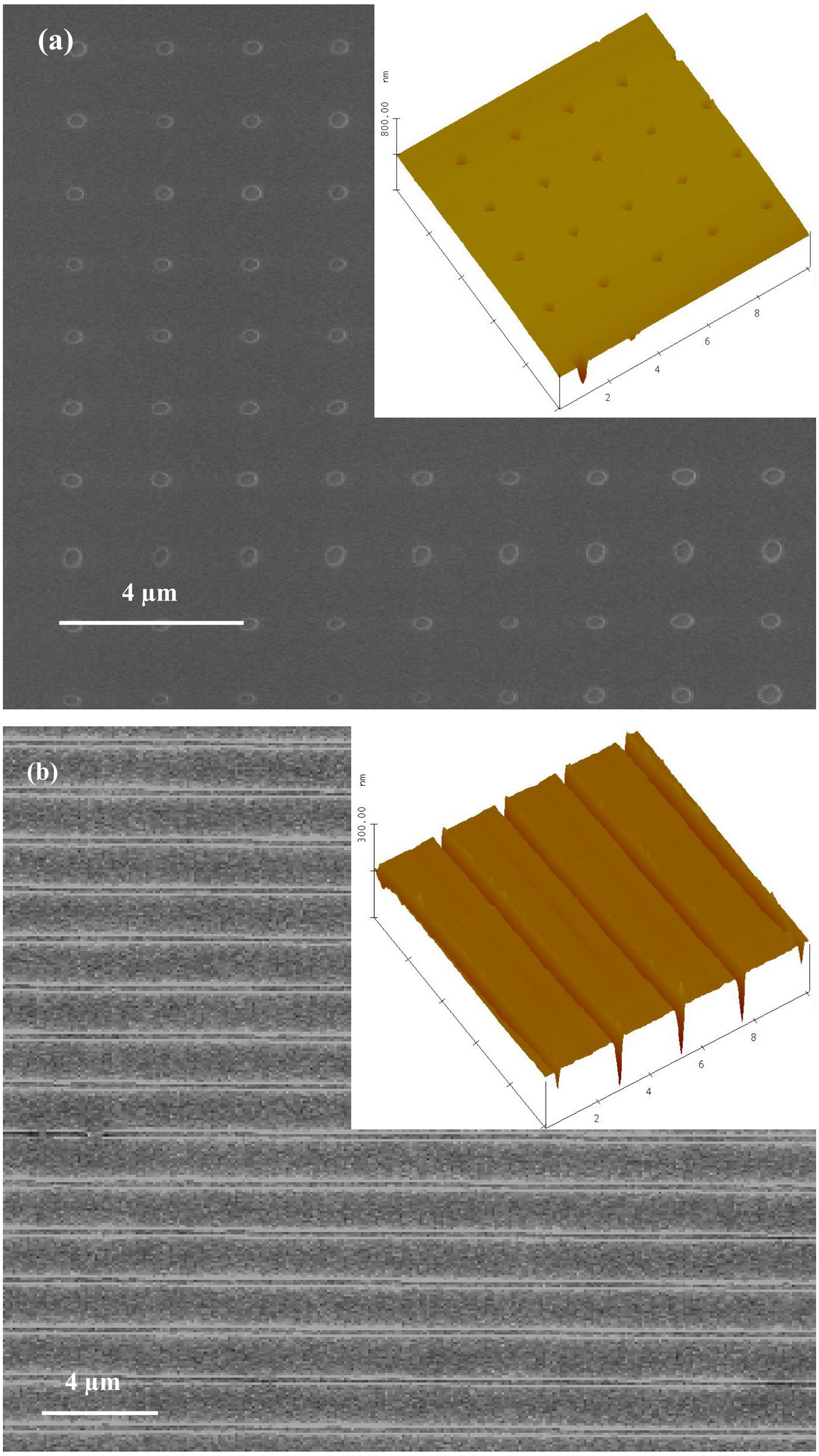

FIG. 5.11 SEM and three dimensional AFM images of (a) nano-dot patterns and (b) nano-line patterns formed on photoresist with single pulse KrF excimer laser exposure at laser fluences of 45 mJ/cm^2 and 38 mJ/cm^2, respectively.

compared to the diameter of the lenses. The depth of the patterns is 32 nm. By a single pulse exposure, as many as 6,250,000 tiny dot patterns can be generated uniformly over an area of 5 mm x 5 mm. Similar to what has been discussed in section 5.3.2, the pattern size increases with respect to the laser fluence because more photon energy is absorbed by the photoresist.

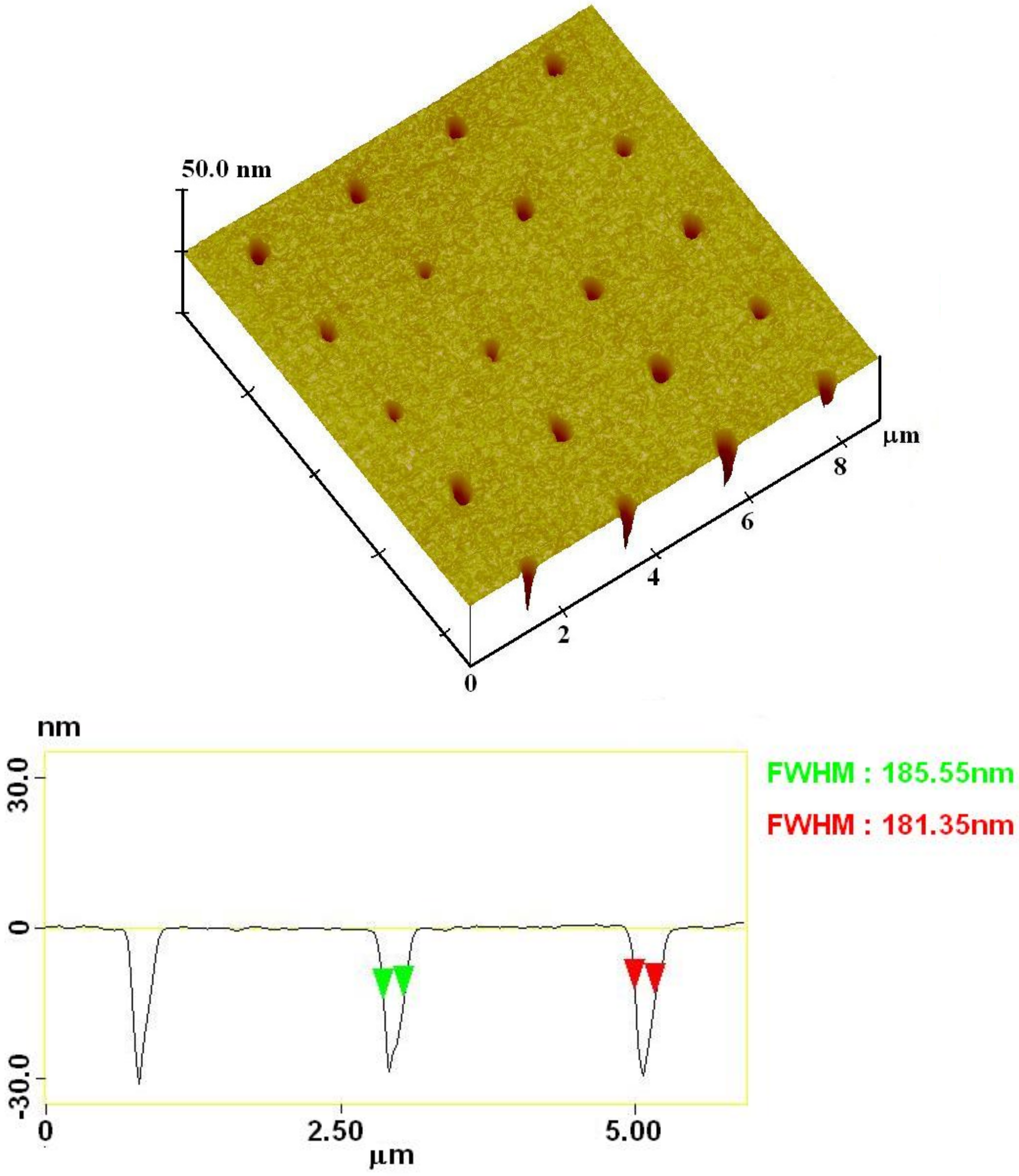

FIG. 5.12 AFM cross sectional of an array of nanopatterns exposed at a laser fluence of 15 mJ/cm^2.

5.4.2 Super-resolution nanopatterning

For a laser system, the minimum waist of a focused laser light spot is around a half of the incident wavelength. In this case, it is 124 nm for a 248 nm excimer laser beam processing. However, by the proper control of the laser irradiation doses and energy, a much finer pattern can be generated. Figures 5.13 (a) and (b) show a SEM image and the AFM 2D profile of a 4 x 4 array patterns generated by the laser patterning with the MLA of NA equals to 0.47. It was found that the pattern feature size can go down to as small as 78 nm measured at its FWHM. This is equivalent to $\lambda/3$, which is a super-resolution over the optical diffraction limit by the nanosecond pulse laser irradiation.

In order to verify the results, the light energy enhancement induced after the laser irradiation through MLA is modeled and simulated by the FDTD simulation software. As shown in Fig. 5.13 (a), the cross sectional electric energy, $|E|^2$ distribution indicates that the focused laser beam has the highest $|E|^2$ enhancement at the central region. The corresponding $|E|^2$ field plot along the X-axis along MLA surface as shown in Fig. 5.14 shows that the calculated FWHM is 185 nm with the $|E|^2$ enhancement of 6.1, which well agrees with the experimental result as shown in Fig. 5.12. In the case of Fig. 5.13, the exposed area is limited at sub-100 nm regime as shown in Fig. 5.14 (b). The deviation in patterns size at the adjacent area for Fig. 5.13 (b) is because of the different distance between MLA and sample resulted from the unparallel of the MLA above Si surface. Since the focal length of the MLA is only 1.1 μm, a small difference in distance creates a big different among different lens focal points.

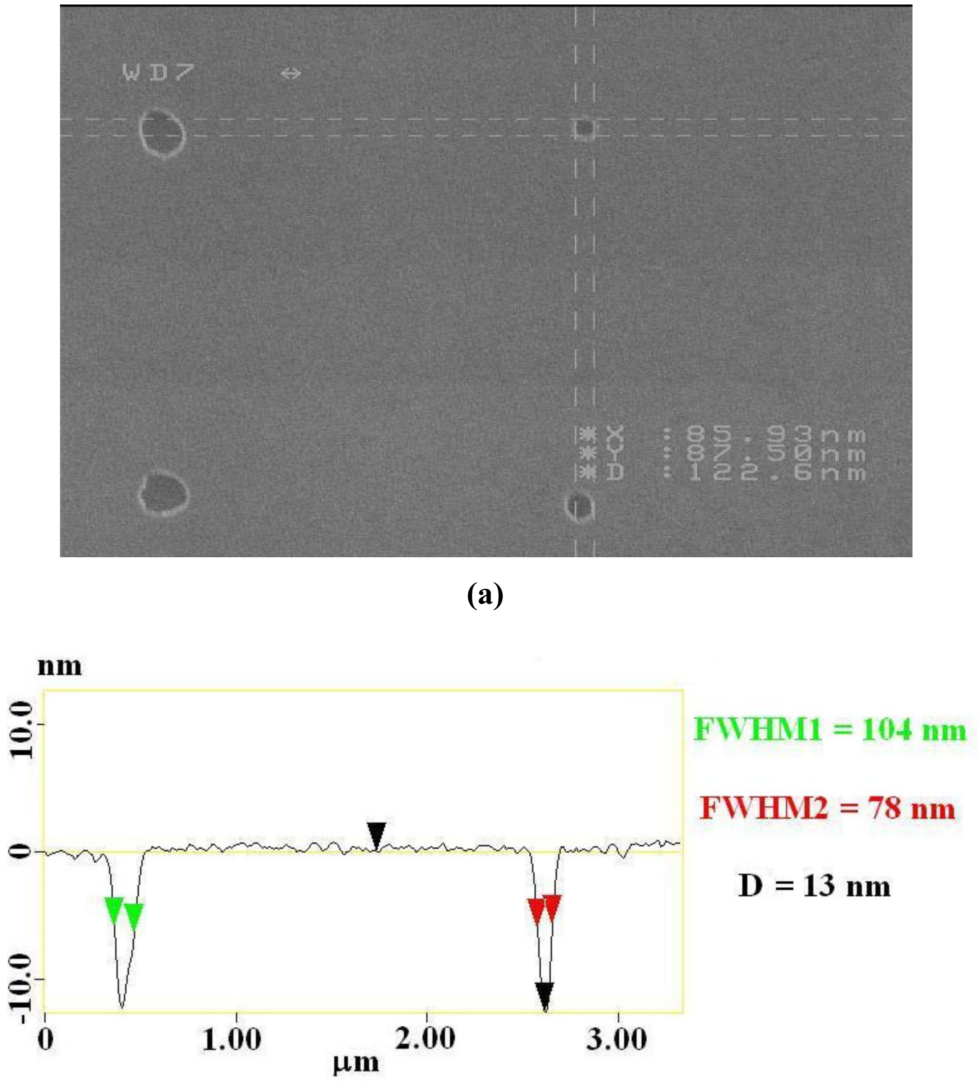

(a)

(b)

FIG. 5.13 (a) Scanning electron microscope image of a pattern with a feature size of 78 nm measured at FWHM equivalent to $\lambda/3$ and (b) the corresponding AFM profile.

Therefore, a high resolution nanostage with MLA alignment system combined with an air gap detection system to detect the focal plane of the MLA is critical to form a uniform large area nanostructures in a short time by this new nanolithography technique. The reason for this phenomenon is largely possible due to interaction of the photopolymer materials with focused laser beam during the exposure. The photochemical reaction of photopolymer materials is initiated if sufficient photon energy is supplied. In this case, the $\lambda/3$ super-resolution nanopatterning is achieved only when the peak region at the center of the focused light beam is above the material's photo-chemical reaction threshold.

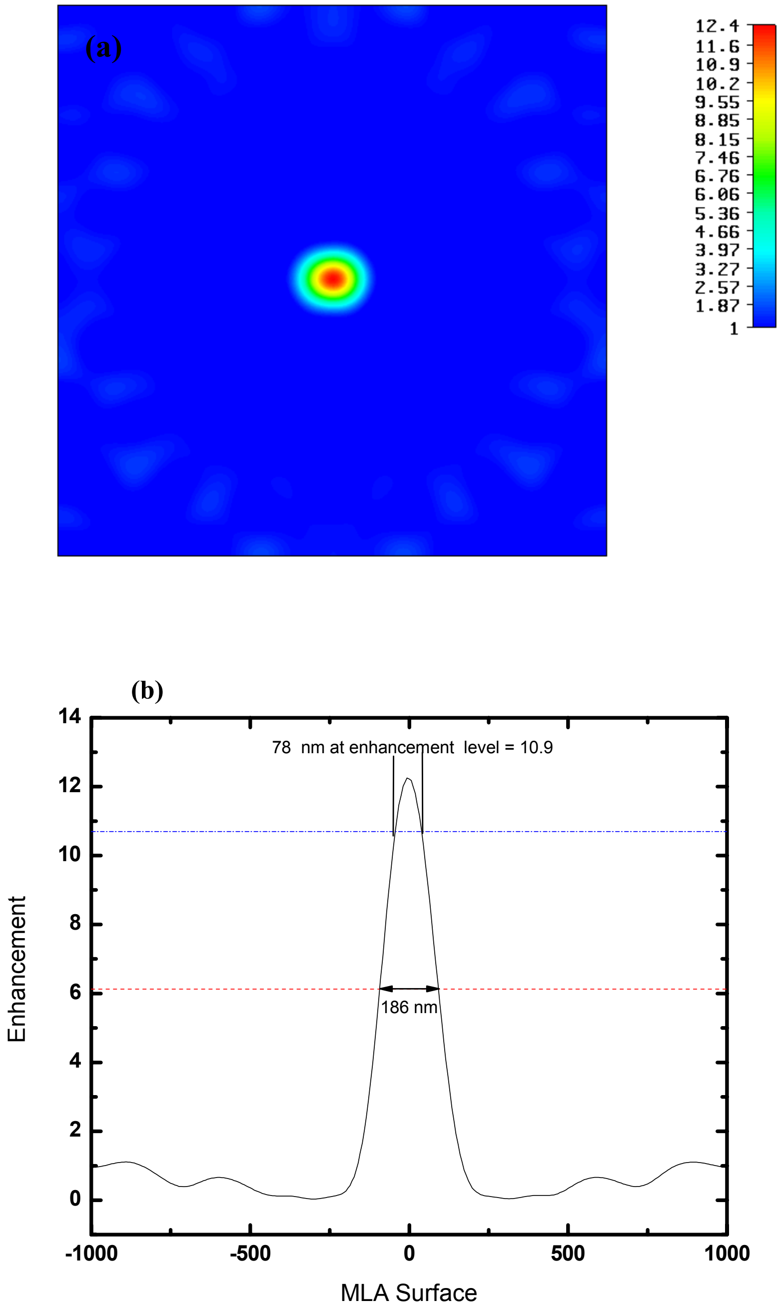

FIG. 5.14 $|E|^2$ distribution at (a) X-Y plane and (b) $|E|^2$ plot along X-direction by KrF excimer laser irradiation through the 1 μm MLA.

5.4.3 Multiple pulse exposure

The size of the nano-features is highly dependent on laser fluence, which can be achieved by controlling laser exposure doses. A higher laser fluence causes more photoresist to be exposed due to more energy absorbed. In this case, protruded line arrays can be obtained if the resist material is ‘over-exposed’ by several laser pulses. This squeezes the line width to the sub-micron region as shown in Fig. 5.15. The sample was coated with UV 54 amplified photoresist, which has a better sensitivity as compared to ma-P 1205 resist. The sample was exposed at a laser fluence of 5.9 mJ/cm^2 for 5 pulses. As can be seen from Fig. 5.15 (a), an array of protruded nano-lines was formed, with the distance of 2 μm between two adjacent lines. The corresponding cross sectional profile is shown in Fig. 5.15 (b). The average width is 400 nm at a height of about 230 nm. The considerable vertical height of the patterns provides sufficient protection for the etching down process to transfer patterns onto the substrate.

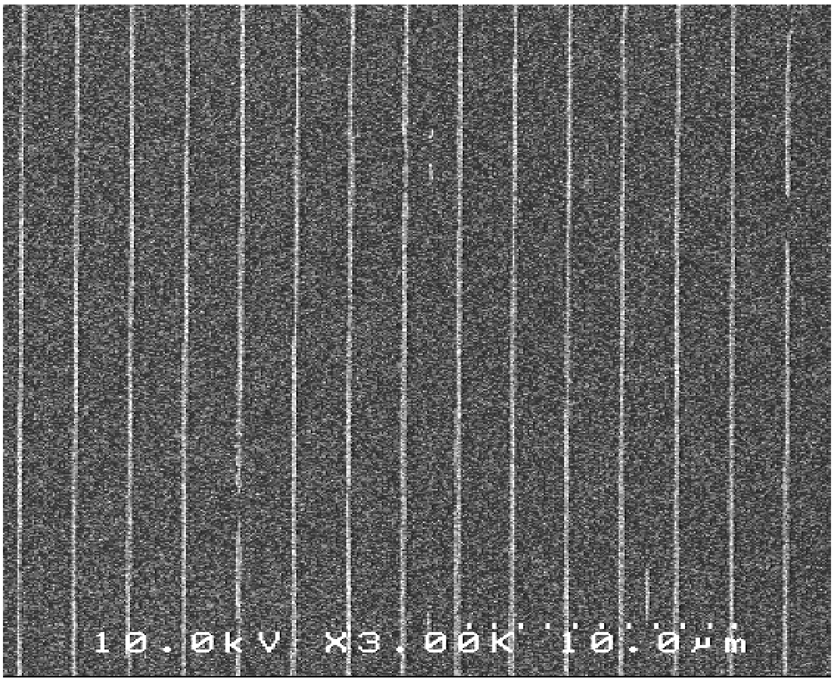

(a)

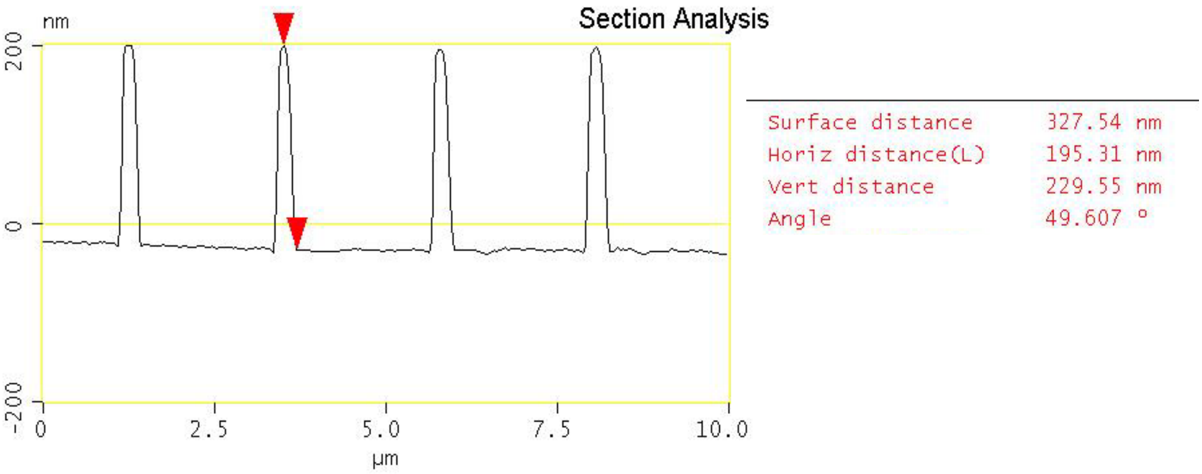

(b)

FIG. 5.15 (a) SEM image and (b) its corresponding cross sectional AFM profile of a sample with multiple pulse exposure by using a 2 µm pitch cylindrical MLA.

However, due to the multiple doses of exposure, there is a large amount of reflected light which makes the edge jagged, as shown in Fig. 5.16 (a). To overcome this problem, a layer of anti-reflective coating was coated underneath the photoresist to reduce the effect of the reflected light on the patterns. As can be seen from Fig 5.16 (b), the width of the pattern is 90±4 nm, with improvement over the pattern edge profile.

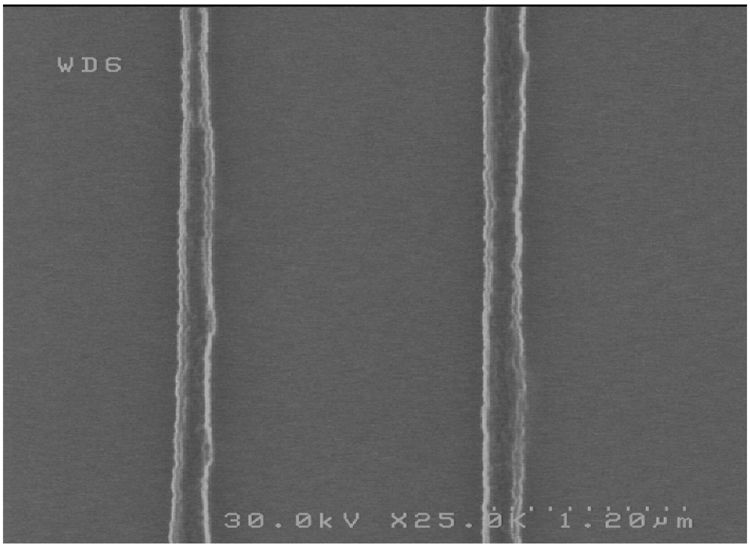

(a)

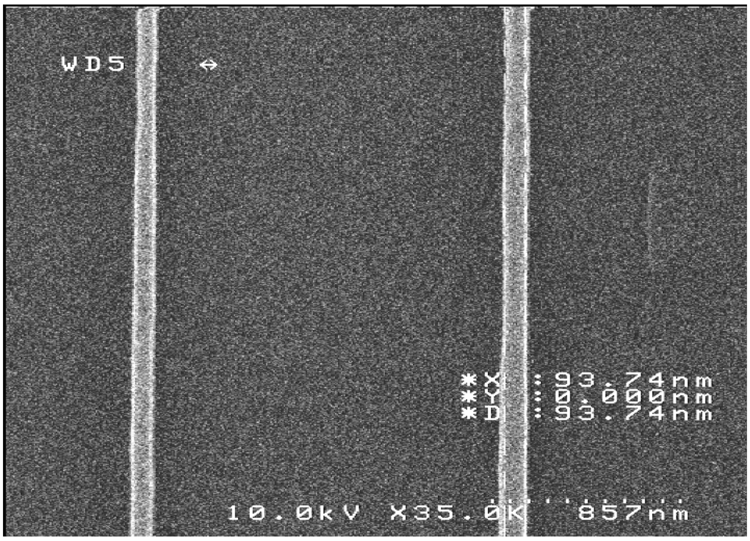

(b)

FIG. 5.16 SEM images of protruded nano-line patterns (a) without and (b) with an anti-reflective coating.

The nano-line width can be further reduced by simply increase the pulse number. Figures 5.17 (a) and (b) show the profiles of two samples with line width measured at 40 nm and 53 nm, respectively. Both samples were exposed for 7 pulses at a laser fluence of 7.8 mJ/cm^2. This gives a six-fold reduction as compared to the exposure wavelength used. However, further increases in exposure pulses generate discontinue lines and uneven line width. This could be due to the poor adhesion of the structure and also the tendency of over-development of the photoresist when the line width becomes smaller.

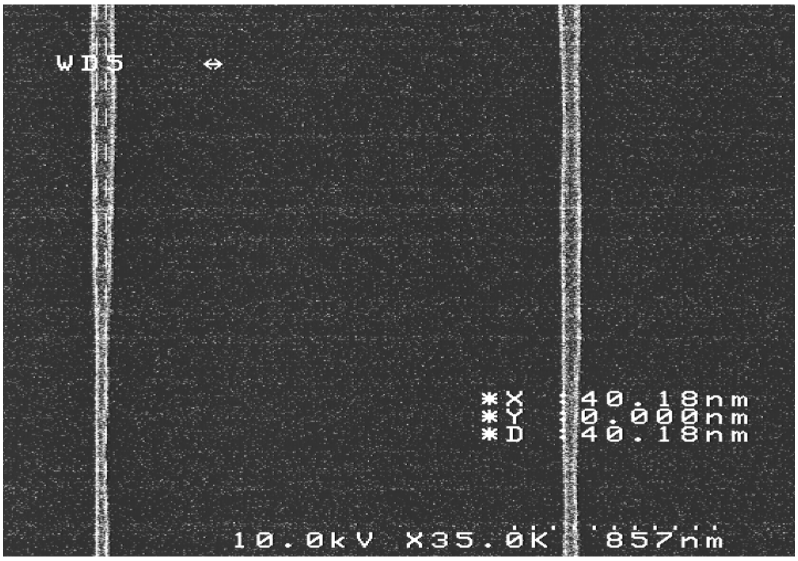

(a)

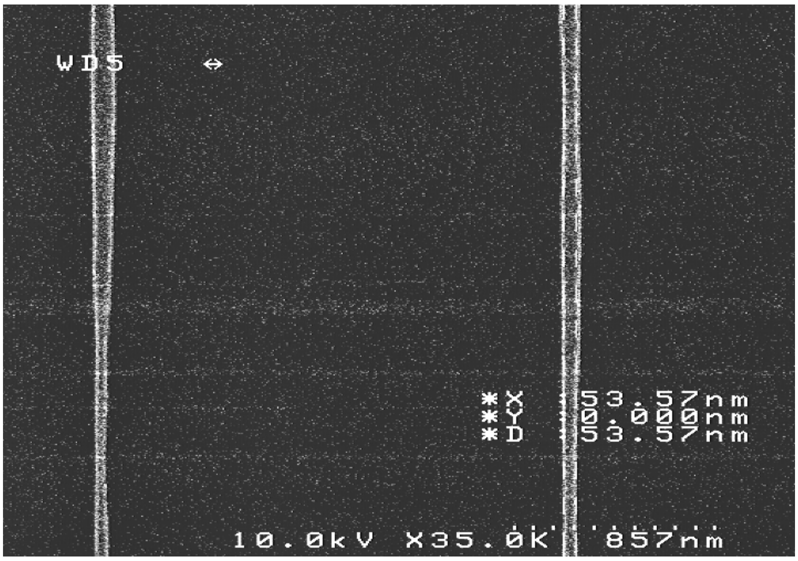

(b)

FIG. 5.17 The SEM images of the samples exposed at a laser fluence of 7.8 mJ/cm^2 for 7 pulses, which gives a line width of (a) 40 nm and (b) 53 nm, respectively.

5.5 MLA surface nanopatterning – applications in precision engineering

The irradiation of laser beam to the MLA generates thousands of focused tiny light beams at the focal plane which acts as a laser writer. This enables features with a size of about a few hundred nanometers to be patterned in single exposure. This patterning technique offers a high throughput and low cost nanopatterning alternative to existing techniques, such as E-beam, NSOL and ion beams. The MLA-based surface patterning has a great potential in various applications. One of them is to pattern phase change material for optical storage media [38,179]. With the utilization of MLA to perform surface patterning, the fabrication of such sub-micron features can be done flexibly.

Table 5.1 Comparison of different surface nanopatterning techniques.

Nanopatterning Technique	**Resolution**	**Throughput**	**Cost**	**Working environment**
E-beam/X-ray lithography	Sub-10 nm	Low	High, sophisticated equipment tools needed	Vacuum
Ion beam	Sub-10 nm	Low	High, sophisticated equipment tools needed	Vacuum
Near-field optical lithography	Sub-30 nm	Low	High, sophisticated equipment tools needed	Flexible
Microlens array nanopatterning	Sub-100 nm	High	Low, no special equipment needed	Flexible

As the media density is a concern to data storage, the coupling of MLA to a precision stage to generate high density of patterns can be a solution. This could also be the case to fabricate photonic crystal as the periodic 2-D structure of photonic crystals [180] can be patterned at any period by altering the movement of each step. It also provides a solution to pattern samples in a large scale and at a fast speed since MLA consists of thousand of lenses. This is particularly important for the fabrication of microelectronic and microfluidic devices.

CHAPTER 6

CONCLUSIONS AND FUTURE WORKS

6.1 Conclusions and Research Contributions

In this thesis, three major works have been presented. Firstly the fabrication techniques of both concave and convex microlens arrays are described. Then the simulation study and results of the light interaction with microlens arrays are discussed. Finally the application of microlens arrays in the large area surface nanopatterning is studied. The following summarizes and concludes the research contributions in this thesis:

1. Novel techniques of microlens array fabrication are demonstrated. Firstly, the feasibility to fabricate microlens arrays (MLA) by the combination of direct laser patterning and chemical wet etching is demonstrated. Experimental results show that concave microlens arrays of diameters 20 μm, 50 μm and 100 μm with hexagonal arrangement were successfully fabricated. The isotropic nature of the wet chemical etching process by hydrofluoric acid (HF) causes the dissolution of the SiO_2 in all directions thus generates spherical concave microlenses on the glass substrates.
2. Both 2D Alpha Step profiler and 3D atomic force microscope (AFM) images show that these microlenses have concave spherical profile whereas the optical microscope and scanning electron microscope (SEM) images show that a smooth lens surface can be obtained. The chemical etching by diluted HF was found to be more efficient as compared to buffered HF due to the fact that the etch rate is determined by

the F^- ion concentrations. It is also found that by varying the percentage of ion F^-, different lens sags are obtained. It demonstrates that the lens curvature can be controlled.

3. The direct laser patterning method provides the flexibility in designing and controlling of lens patterns by modifying the initial design and translating it into NC codes, which can be done in a few minutes. This method also eliminates the need of the complicated lithography process that is much dependent on the photomask production. However, this fabrication technique is only limited to the fabrication of concave microlens arrays because the shape of the microlenses, either concave or convex, is largely dependent on the nature of the etching process. Since the etching method used in this experiment was the wet chemical etching, it is impossible to fabricate a convex microlens array by this technique.

4. Another novel fabrication technique that was explored in this research study was the fabrication of MLAs by using a combination of laser interference lithography (LIL), thermal reflow process and reactive ion etching. MLAs of convex lenses with diameter ~1 μm were successfully fabricated by a novel hybrid technique of combination of laser interference lithography by Lloyd's mirror set-up, thermal reflow process and reactive ion etching. With the laser interference lithography, the production of identical photoresist structure arrays is made possible. These periodic lines and circular structures were formed on photoresist by the exposure of fringes generated by laser interference, which were effectively thermally reflowed into hemispherical and cylindrical MLAs due to the surface tension between photoresist and the substrate surface. Subsequently, the MLA profiles were successfully transferred to the quartz substrate by reactive ion etching without much change to the profile due to the etch rates slightly differ.

5. The AFM and SEM images of the etched quartz profile show that a smooth lens surface with average roughness *Ra* of ~ 3 nm was obtained. The deviation of the fabricated microlenses sag height and diameter is below 5 %, which suggests a uniform microlens array can be produced by this technique. The laser interference lithography technique can provide a feasible way to create rectangular packed MLAs on quartz without using a photomask. This hybrid technique is able to control the size of the microlenses by changing the interference angle of the 2 laser beams thus suggesting that the use of expensive photomasks is not needed.

6. The optical behaviour and characteristics of microlens arrays is studied extensively by classical optical simulation technique and numerical solution method. Theoretical study and simulation are used to define the optical behavior of the light propagation through microlens arrays during the patterning process. Both simulation techniques offer a good prediction to the laser light interaction with microlens arrays and give insight details of the intensity distribution of the focused laser spots at the microlens array's focal plane. The classical optical simulation is suitable for microlens arrays with size in the range of few tenths of micrometer while numerical method of FDTD is suitable for microlens arrays with size of below 5 microns.

7. The intensity profile of various microlenses sag height at different image planes parallel to focal plane is studied. It is found that the increase of the sag height increases the intensity and decreases the FWHM. It is also found that various periodic patterns are observed at different image planes as it moves away from the focal plane of the microlens arrays.

8 A surface nanopatterning method by the irradiation of laser beam through a microlens array is developed and studies intensively. The microlens arrays were used for surface nanopatterning on photoresist material by femtosecond and nanosecond

lasers. The effects of laser fluence, pulse number and fraction Talbot phenomena on the patterns generated were investigated. It was found that large area and high speed surface nanopatterning can be easily performed by just a single pulse or multiple pulses exposure. Thousands to millions of identical nanopatterns can be generated depending on the size of the microlens arrays.

9 Sub-100 nm patterns can be fabricated by proper control of the laser exposure doses. This super-resolution surface nanopatterning of feature size of λ/3 is a breakthrough in overcoming optical diffraction limit. The nanopattern size can go down to 50 nm by over exposure and 70 nm by single exposure.

6.2 Recommendations for Future Works

For the future works, a few recommendations are proposed as the following:

1. Fabrication of micro-ball lens arrays to further reduce the features size that can be obtained. The near-field enhancement by the micro-spheres has been proven to be able to produce feature size down to sub-100 nm. However the issue is the repeatability. If one can fabricate a microlens arrays with the lens structure re-assembling a ball-shape, it will greatly improve the nanopatterning resolution.
2. Fabrication of microlens arrays for bioengineering applications. One of the important areas is the synthetic of biological optics for better imaging capability. The biological optics such as fish-eye and insect eye have similar structures as a microlens array and have some unique features such as wide field of view (FOV). Therefore, the success of fabrication of such biological optics can improve the imaging ability in micro- and nano- scales.

3. Detailed theoretical study of the surface nanopatterning by laser irradiation through microlens arrays. The interaction of focus laser beam with the photoresist needs to be characterized since the early simulation study only concentrated on the optical behavior of microlens arrays. These can give a detailed insight into the surface nanopatterning mechanism.
4. The dependence of microlense size on the wavelength of the laser limits the size of the microlenses. Since the current LIL setup was using a single wavelength laser, which was a 325 nm laser, the size of the microlenses fabricated was limited to < 2 μm. On the other hand, this study was concentrated more on the development of the fabrication process, so the study of the optimisation of process parameters were still lacking. Hence, in future, a comprehensive study on the laser fluence is required to remove the photoresist for a certain thickness as well as the effects on how different heating temperatures and different heating times affect the reflow process should be carried out so as to maximise the packing ratio of the MLAs. Furthermore, different angles for the Lloyd's mirror set-up and different types of laser can be tested to fabricate MLAs at different sizes

REFERENCES

1. S. Sinzinger and J. Jahns. Microoptics. pp. 3-5, New York: Wiley-VCH, 1999.
2. H. Bach and N. Neuroth (ed). The properties of optical glass. Berlin:Springer Verlag, 1995.
3. Nicholas F. Borrelli. Microoptics Technology: Fabrication and Applications of Lens Arrays and Devices. New York: Marcel Dekker Inc., 1999.
4. J. W. Blaker and W.M. Rosenblum, Optics: An Introduction for Student of Engineering, New York: Macmillan Publishing, 1993.
5. N.F. Borrelli, R.H. Bellman, J.A. Durbin and W. Lama, Imaging and radiometric properties of microlens arrays, Appl Opt., *30(25)*, pp.3683-3686, 1991.
6. M. Kawazu and Y. Ogura, Application of gradient-index fiber arrays to copying machines, Appl. Opt., *19(7)*, 1105-1107, 1980.
7. M.C. Hutley and R.F. Stevens. The formation of integral images by afocal pairs of lens arrays ("superlenses"), Microlens Arrays: IOP Short Meeting Series, *30*, pp.147-154, 1991.
8. N. Davies and M. McCormick. The use of microlens arrays in integral photography, Microlens Arrays: IOP Short Meeting Series, *30*, pp.109-122, 1991.
9. L. Erdmann and K.J. Gabriel. High-resolution digital integral photography by use of a scanning microlens array, Appl. Opt., *40(31)*, pp.5592-5599, 2001.

10. F. Okano, H. Hoshino and I. Yuyama. Real-time pickup method for a three-dimensional image based on integral photography, Appl. Opt., *36(7)*, pp.1598-1603, 1997.
11. J. Arai, H. Kawai and F. Okano. Microlens arrays for integral imaging system, Appl. Opt., *45(36)*, pp.9066-9078, 2006.
12. B. Javidi and Y. Frauel. Three-dimensional object visualization and regconition based on computational integral imaging, Proc. SPIE, *5106*, pp.22-29, 2003.
13. H. Choi, J.H. Park, J. Kim, S.W. Cho and B. Lee. Wide-viewing-angle 3D/2D convertible display system using two display devices and a lens array, Optics Express, *13(21)*, pp.8424-8432, 2005.
14. R. Ng, M. Levoy, M. Brédif, G. Duval, M. Horowitz and P. Hanrahan. Light field photography with a hand-held plenoptic camera. Stanford Tech report CTSR 2005-02, Stanford University, 2005.
15. R. Völkel, M. Eisner and K.J. Weible. Miniaturization of Imaging Systems, MST news, *2*, pp.36-38, 2003.
16. R. Völkel, M. Eisner and K.J. Weible. Miniaturized imaging systems, Microelectronic Eng., *67-68*, pp.461-472, 2003.
17. N. Stauffer and D. Wilwerding, Scientific Honeyweller, 3, 1-10, 1982
18. S. Aoyama, T. Kurahashi, D. Uchida, M. Shinohara and T. Yamashita. Giant microoptics: wide applications in liquid crystal display (LCD) systems, Diffractive Optics and Micro-Optics: OSA Technical Digest Series, *5*, pp.266-268, 1996.

19. L.C. Ling, Y.I. Yen and F.C. Ho. An Efficient Illumination System for Single-Pane LCD Projector, SID 01 Digest, *46*, pp.1184-1187, 2001.
20. R.M. Tasso. High-contrast screen with random microlens array, US Patent, *6700702*, 2002.
21. H. Urey and K.D. Powell. Microlens array-based pupil expander for fll color display applications, Proc. SPIE, *5456*, 2004.
22. H.J. Tiziani, R. Achi, R.N. Krämer, T. Hessler, M.T. Gale, M. Rossi and R.E. Kunz. Microlens arrays for confocal microscopy, Opt. & Laser Tech., *29(2)*, pp.85-91, 1997.
23. K. Fujit, O. Nakamura, T. Kaneko, M. Oyamada, T. Takanatsu and S. Kawata. Confocal multipoint multiphoton excitation microscope with microlens and pinhole arrays, Opt. Comm., *174*, pp.7-12, 2000.
24. J.C. Roulet, R. Völkel, H.P. Herzig, E. Verpoorte, N.F de Rooij and R. Dändliker, Microlens systems for fluorescence detection in chemical Microsystems, Opt. Eng., *40(5)*, pp.814-821, 2001.
25. K.P. Bishop, R.E. Pierson and E.Y. Chen. A multiview fast optical tomography system using microlens arrays, Diffractive Optics and Micro-Optics, OSA Technical Digest Series, *5*, pp.274-279, 1996.
26. C.H. Sow, A.A. Bettol, Y.Y.G. Lee, F.C. Cheong, C.T. Lim and F. Watt. Multiple-spot optical tweezers created with microlens arrays fabricated by proton beam writing, Appl. Phys. B, *78*, pp.705-709, 2004.

27. T.G. McDonald, R.M. Boysel and J.B. Sampsell, Opt. Fiber Conf. OFC, *paper WM-22*, pp.22-26, 1990.
28. J.S. Leggatt. Single mode fibre interconnect with microlenses, Microlens Arrays: IOP Short Meeting Series, *30*, pp.103-108, 1991.
29. K. Nishiza and M. Oikawa, SPIE vol. 1751, 54, 1992.
30. A.W. Lohmann, Array illuminatiors and complexity theory, Opt. Comm., *89*, pp.167-172, 1992.
31. N. Rajkumar, J.N. McMullin, B.P. Keyworth and R.I. MacDonald. 3×3 optoelectronic cross-barswitch using vertical cavity surface emitting laser arrays, Diffractive Optics and Micro-Optics, OSA Technical Digest Series, *5*, pp.75-78, 1996.
32. R. Völkel, H.P. Herzip, Ph. Nussbaum, W. Singer and R. Dändliker. Microlens lithography, Diffractive Optics and Micro-Optics: OSA Technical Digest Series, *5*, pp.278-281, 1996.
33. R. Völkel, H.P. Herzip, Ph. Nussbaum, P. Blattner, R. Dändliker, E. Cullmann and W.B. Hugle. Microlens lithography and smart masks, Microelectronic Eng., *35*, pp.513-516, 1997.
34. M.H. Wu, K.E. Paul and G.M. Whitesides. Patterning flood illumination with microlens arrays, Appl. Opt., *41(13)*, pp.2575-2585, 2002.
35. M.H. Wu and G.M. Whitesides. Fabrication of arrays of two-dimensional micropatterns using microspheres as lenses for projection photolithography, Appl. Phys. Lett., *78(16)*, pp. 2273-2275, 2001.

36. M.H. Wu and G.M. Whitesides. Fabrication of two-dimensional arrays of microlenses and their applications in photolithography, J. Micromech. Microeng., *12*, pp.747-758, 2002.

37. J. Kato, N. Takeyasu, Y. Adachi, H.B. Sun and S. Kawata. Multi-spot parallel processing for laser micronanofabrication, Appl. Phys. Lett., *86*, 044102, 2005.

38. Y. Lin, M. H. Hong, C. S. Lim, G. X. Chen, L. S. Tan, Z. B. Wang, L. P. Shi, and T. C. Chong. Ultrafast laser induced parallel phase change nanolithography, Appl. Phy. Lett., *89*, 041108, 2006.

39. C.D. Popovic, R.A. Sprague and G.A. Neville Connell. Technique for monolithic fabrication of microlens arrays, Appl. Opt., *27*, pp.1281-1284, 1998.

40. K. Mersereau, C.R. Nijander, W.P. Townsend and A.Y. Feldblum. Aberration-corrected etched microlens arrays, Diffractive Optics and Micro-Optics, OSA Technical Digest Series, *5*, pp.24-26, 1996.

41. C.P. Lin, H. Yang and C.K. Chao. Hexagonal microlens array modeling and fabrication using a thermal reflow process, J. Micromech. Microeng., *13*, pp.775-781, 2003.

42. Ph. Nussbaum, R. Völkel, H.P. Herzig, M. Eisner and S. Haselbeck. Design, fabrication and testing of microlens arrays for sensors and microsystems, Pure Appl. Opt., *6*, pp.617-636, 1997.

43. J. Yao, Z. Cui, F.H. Gao, Y.X. Zhang, Y.K. Guo, C.L. Du, H.J. Zeng and C.K. Qiu. Refractive micro lens array made of dichromate gelatin with gray-tone photolithography, Microelectronic Engineering, *57-58*, pp.729-735, 2001.

44. X.C. Yuan, W.X. Yu, N.Q. Ngo and W.C. Cheong. Cost-effective fabrication of microlenses on hybrid sol-gel glass with a high-energy beam-sensitive gray-tone mask, Opt. Express, *10(7)*, pp.303-308, 2002.

45. M. Pitchumani, J. Brown, W. Mohammed and E.G. Johnson. Micro-optic fabrication with subdomain masking, Appl. Opt., *43(8)*, pp.1676-1682, 2004.

46. S.H. Lee and W. Däschner. Method for producing micro-optic elements with gray scale mask, US Patent, *6107000*, 2000.

47. K. Bird and T.J. Hall. The computer controlled generation of microlens arrays, Microlens Arrays: IOP Short Meeting Series, *30*, pp.35-40, 1991.

48. F. Gex, D. Horville, G. Lelièvre and D. Mercier. Improvement of a manufacturing technique for long focal length microlens arrays, Pure Appl. Opt., *5*, pp.863-872, 1996.

49. T.R.M. Sales, S. Chakmakjian, G.M. Morris and D.J. Schertler. Light tamers: Engineered microlens arrays provide new control for display and lighting applications, Photonic Spectra, pp.58-64, June 2004.

50. D.H. Raguin, G.M. Morris and P.M. Emmel. Method for making optical microstructures having profile heights exceeding fifteen microns, US Paternt, *6410213*, 2002.

51. C.L. Du, X.C. Dong, C.K Qiu, Q.L. Deng and C.X. Zhou. Profile control technology for high-performance microlens array, Opt. Eng., *43(11)*, pp.2595-2602, 2004.

52. Heather W. Maskless patterning can create micro-optics, Laser Focus World, *32(1)*, pp.15-16, 1996.

53. M. Fritze, M.B. Stern and P.W. Wyatt. Laser-fabricated glass microlens arrays, Opt. Lett., *23(2)*, pp.141-143, 1998.

54. M. Wakaki, Y. Komachi and G. Kanai. Microlenses and Microlens Arrays Formed on a Glass Plate by Use of a CO 2 Laser, Appl. Opt., *37(4)*, pp.627-631 (1998)

55. A.Y. Smuk and N.M. Lawandy. Direct laser fabrication of dense microlens arrays in semiconductor-doped glass, J. Appl. Phys., *87(8)*, pp.4026-4030, 2000.

56. G. Beadie and N.M. Lawandy. Single-step laser fabrication of refractive microlenses in semiconductor-doped glasses, Opt. Lett., *20(21)*, pp.2153-2155, 1995.

57. N. Fromer and N.M. Lawandy. Single step fabrication of glass microlenses for array and diode laser applications, Diffractive Optics and Micro-Optics, OSA Technical Digest Series, *5*, pp.31-34, 1996.

58. N.F. Borrelli. The generation of lens arrays using photothermal techniques, Microlens Arrays: IOP Short Meeting Series, *30*, pp.1-16, 1991.

59. N.F. Borrelli, D.L. Morse, R.H. Bellman and W.L. Morgan. Photolytic technique for producing microlenses in photosensitive glass, Appl. Opt., *42*, pp.2520-2525, 1985.

60. N.F. Borrelli and D.L. Morse. Microlens arrays produced by a photolytic technique, Appl. Opt., *27(3)*, pp.476-479, 1988.

61. W.X. Yu and X.C. Yuan. Fabrication of refractive microlens in hybrid SiO2/TiO2 sol-gel glass by electron beam lithography, Optics Express, *11(8)*, pp.899-903, 2003.

62. M. He, X.C. Yuan, N.Q. Ngo and S.H. Tao. Single-step fabrication of a microlens array in sol-gel material by direct laser writing and its application in optical coupling, J. Opt. A: Pure Appl. Opt., *6*, pp.94-97, 2004.

63. M. He, X.C. Yuan, J. Bu and W.C. Cheong. Fabrication of concave refractive microlens arrays in solgel glass by a simple proximity-effect-assisted reflow technique, Opt. Lett., *29(9)*, pp.1007-1009, 2004.

64. X.C. Yuan, W.X. Yu, M. He, J. Bu, W.C. Cheong, H.B. Niu and X. Peng. Soft-lithography-enabled fabrication of large numerical aperture refractive microlens array in hybrid SiO2–TiO2 sol-gel glass, Appl. Phys. Lett., *86*, pp.114102, 2005.

65. A.H.O. Kärkkäinen, J.T. Rantaa, J.M. Tamkin and M.R. Descour. Photolithographic processing of hybrid glasses for microoptics, J. Lightwave Tech., *21(3)*, pp.614-623, 2003.

66. A.H.O. Kärkkäinen, J.M. Tamkin, J.D. Roger, D.R. Neal, O.E. Hormi, G.E. Jabbour, J.T. Rantaa and M.R. Descour. Direct photolithographic deforming of organomodified siloxane films for micro-optics fabrication, Appl. Opt., *41(19)*, pp.3988-3998, 2002.

67. D. MacFarlane, V. Narayan, W. Cox, T. Chen and D. Hayes. Microjet fabrication of microlens arrays, IEEE Phot. Tech. Lett., *6*, pp1112-1115, 1994.

68. W.R. Cox, T. Chen, D.W. Ussery, D.J. Hayes, and, R.F. Hoenigman, Microjet printing of anamorphic microlens arrays, SPIE Proceedings, *2687*, pp.89-98, 1996.

69. W.R. Cox, D.J. Hayes, T. Chen, H-J Trost, M.E. Grove, R.F. Hoenigman and D.L. MacFarlane. Low cost optical interconnects by microjet printing, IMAPS International Journal of Microcircuits & Electronic Packaging, *20(2)*, pp.89-95, 1997.

70. U. Köhler, A.E. Guber, W. Bier and M. Heckele. Fabrication of microlenses by plasmaless isotropic etching combined with plastic moulding, Sensors and Actuators A, *53(1-3)*, pp.361-363, 1996.

71. L.W. Pan, X.J. Shen and L.W. Lin. Microplastic lens array fabricated by a hot intrusion process, J. Microelectromechanical Sys., *13(6)*, pp.1063-1071, 2004.

72. T.L. Hoopman and D.J.W. Aastuen. Method of making a microlens arrya and mold, US Patent, 5300263, April 1994.

73. T. Teshima, T. Yagi, Y. Shimada and T. Ushijima. Methods of fabricating a microstructure array, US Patent, 6632342, October 2003.

74. S. Möller and S.R. Forrest. Improved light out-coupling in organic emitting diodes employing ordered microlens arrays, J. Appl. Phys., *91(5)*, pp.3324-3327, 2002.

75. S.D. Moon, N. Lee and S. Kang. Fabrication of a microlens array using micro-compression molding with an electroformed mold insert, J. Micromech. Microeng., *13*, pp.98-103, 2003.

76. S. Kang. Replication technology for micro/nano optical components, Jpn. J. Appl. Phys., *43(8B)*, pp.5706-5716, 2004.

77. M.A. Fitch. Molded Optics: mating precision and mass production, Photonic Spectra, *25*, pp.83-87, 1991.

78. Y.Q. Fu and K.A. Ngoi Bryan. Investigation of diffractive-refractive microlens array fabricated by focused ion beam technology, Opt. Eng., *40(4)*, pp.511-526, 2001.

79. P. Ruther, B. Gerlach, J. Göttert, M. Ilie, J. Mohr, A. Müllerand C. Oβmann. Fabrication and Characterization of microlenses realized by a modified LIGA process, Pure Appl. Opt., *6*, pp.643-653, 1997.

80. E.P. Chan and A.J. Crosby. Fabricating microlens arrays by surface wrinkling, Adv. Mat., *18*, pp.3238-3242, 2006.

81. J.F. Ready (ed). Handbook of laser materials processing. pp. 27-90, US:LCCN, 2001.

82. Bäuerle, D. Laser Processing and Chemistry. pp. 191-208, New York: Springer. 1996

83. B. S. Yilbas and A. Kar. Thermal and efficiency analysis of the CO_2 laser cutting process, Opt. Lasers Eng. *30*, pp. 93-106, 1998.

84. M. L. Ngan, K. C. Lee, and K. W. Cheah. High power density laser etching of silicon, J. Appl. Phys. *83*, pp. 1637, 1998.

85. H. Grebel, T. Gayen, and H. W. Wu. Laser-induced etching of Si surfaces: The effect of weak background light, J. Appl. Phys. *79*, pp. 4414-4417, 1996.

86. A. Luft, U. Franz, A. Emsermann, and J. Kaspar. A study of thermal and mechanical effects on materials induced by pulsed laser drilling, Appl. Phys. A: Mater. Sci. Process. *63*, pp. 93-101, 1996.

87. B. J. Bartholomeusz and M. C. Gupta, Laser marking of thin organic films, Appl. Opt. *31*, 4829-4833, 1992.

88. M. Ignatiev, I. Smurov, and G. Flamant. Laser marking of thin organic films, Meas. Sci. Technol., *5*, pp. 563-573, 1994.

89. W. Radley and W.C. Swope. Laser drilling with focused Gaussian beams, J. Appl. Phys., *72(8)*, pp. 3686-3696, 1992.

90. H.K. Tonshoff, V. Alvensleben, A. Ostendorf, G. Willmann and T. Wagner. Precision machining using UV and ultrashort pulse lasers, Proc. SPIE, *3680*, pp. 536-545, 1999.

91. Thomas, A.W. Repair of Thin Film Wiring with Laser-Assisted Processes, IEEE, pp. 759-762, 1992

92. X. Zhang, S.S. Chum J.R. Ho and C.P. Grigoropoulos. Excimer laser ablation of thin gold films on a quartz crystal microbalance at various argon background pressures, Appl. Phys. A, *64*, pp. 545-552, 1997.

93. Y. Kaganovskii, H. Vladomirsky and M. Rosenbluh. Periodic lines and holes produced in thin Au films by pulsed laser irradiation, J. Appl. Phys., *100*, 044317, 2006.

94. Y.W. Zheng, Y.F. Lu, Z.H. Mai and W.D. Song. Removing spherical silica particles from Si, Ge and NiP substrates by KrF excimer laser, Jpn. J. Appl. Phys., *39*, pp. 5894-5898, 2000.

95. Miller, J.C. (ed). Laser Ablation, Principles and Applications. pp. 1-26, London: Springer-Verlag. 1994

96. F. Bachman. Excimer lasers in a fabrication line for a highly integrated printed circuit board, Chemtronics, *4*, pp. 149-156, 1989.

97. B. Lan. Laser-assisted MEMS fabrication by third harmonic DPSS Nd:YAG laser. MS Thesis, National University of Singapore. 2003.

98. P. Heyl, T. Olschewski and R.W. Wijnaendts. Manufacturing of 3D structures for micro-tools using laser ablation, Microelectronic Eng., *57-58*, pp. 775-780, 2001.

99. M. Elwenspoek and H.V. Jansen. Silicon micromachining, pp.1-7, New York: Cambridge University Press, 1998.

100. Y. Nishi and R. Doering (ed). Handbook of semiconductor manufacturing technology, New York : Marcel Dekker, 2000.

101. S. Middleman and A. K. Hochberg. Process engineering analysis in semiconductor device fabrication, pp.392-394, New York: McGraw-Hill. 1993.

102. G.T.A. Kovacsm N.I. Maluf and K.E. Petersen. Bulk machining of silicon, Proc. IEEE, *86(8)*, pp.1536-1551, 1998.

103. K.E. Petersen. Silicon as a Mechanical Material, Proc. IEEE, *70(5)*, pp.420-457, 1982.

104. J.D. Mansell, D.R. Neal and S.W. Smith. Binary-optic smoothing with isotropic etching, Appl. Opt., *36(20)*, pp. 4644-4647, 1997.

105. T. Diepold and E. Obermeier. Smoothing of ultrasonically drilled holes in borosilicate glass by wet chemical etching, J. Micromech. Microeng., *6*, pp.29-32, 1996.

106. H. Nielsen and D. Hackleman. Some Illumination on the Mechanism of SiO Etching in HF Solutions, J. Electrochem. Soc., *130*, pp.708-712, 1983.

107. J. Judge. A study of the dissolution of SiO_2 in acidic fluoride solutions, J. Electrochem. Soc., 118, pp. 1772-1775, 1971.

108. G. Parisi, S. Haszko and G. Rozgonyi. Tapered Windows in SiO_2: The Effect of NH_4F:HF Dilution and Etching Temperature, J. Electrochem. Soc., *124*, pp.917-921, 1977.

109. J.E. Andrew, P.E. Dyer, R.D. Greennough and P.H. Key. Metal film removal and patterning using a XeCl laser, Appl. Phys. Lett., *43(11)*, pp. 1076–1078, 1983.

110. M. Born and E. Wolf, Principles of optics, 7 ed., UK: Cambridge University Press, 1999.

111. H.I. Smith, Submicron- and Nanometer-Structures Technology, MA: NanoStructures Press Sudbury, 1994.

112. Walsh M E , Nanostructuring magnetic thin films using interference lithography, M.S. Thesis, Massachusetts Institute of Technology, 2000.

113. Yu F, Li P, Shen H, Mathur S, Lehn C L, Bakowsky U and Mücklich F, Laser interference lithography as a new and efficient technique for micropatterning of biopolymer surface, Biomaterials, *26*, pp.2307-2312. 2005.

114. S.I. Nesterov, D.V. Myagjov and E.L. Portnoi, Nanoscale periodical structures fabricated by interference photolithography, Int. J. Nanoscience, *3*, pp.59-64. 2004.

115. N.D. Lai, W.P. Lai, J.H. Lin, C.C. Hsu and C.H. Lin. Fabrication of two- and three-dimensional periodic structures by multi-exposure of two-beam interference technique, Opt. Exp., *13(23)*, pp. 9605-9611, 2005.

116. C. Vass and K. Osvay. Fabrication of 150 nm period grating in fused silica by two-beam interferemotric laser induced backside wet etching method, Opt. Exp., *14(18)*, pp. 8354-8359, 2006.

117. D. Daly, R.F. Stevens, M.C. Hutley and N. Davies. The manufacture of microlenses by melting photoresist, Meas. Sci. Technol., *1*, pp.759-766, 1990.

118. O'Neill F T and Sheridan J T, Photoresist reflow method of microlens production Part 1: Background and experiments, Optik, *113*, pp.391-404, 2002.

119. S. Audan, B. Faure, B. Mortini, J. Regolini, G. Schlatter and G. Hadziioannou, Study of mechanism involved in photoresist microlens formation, Microelectronic Eng., *83*, pp.1087-1090, 2006.

120. S. Haselbeck, H. Schreiber, J. Schwider and N. Streibl. Microlenses fabricated by melting a photoresist on a base layer, Opt. Eng., *32*, pp. 1322-1324, 1993.

121. H.S.M. Eisner, S. Haselbeck and J. Schwider, Reactive ion etching of microlens arrays into fused silica, SPIE, *2*, pp.142-146, 1994.

122. P. Savander. Microlens arrays etched into glass and silicon, Opt. Lasers Eng., *20(2)*, pp. 97-107, 1994.

123. H. Sanker, E. Motamedi, R. Hall, W.J. Gunning and M. Khoshnevisan. Fabrication of refractive microlens arrays, Proc. SPIE, *2383*, pp. 179-183, 1995.

124. R. Shen and G.C. Righini. Characterization of reactive ion etching of glass and its applications in integrated optics, J. Vac. Sci. Technol. A, *9(5)*, pp. 2709-2712, 1991.

125. M.V. Bazylenko and M. Gross. Reactive ion etching of silica structures for integrated optics applications, J. Vac. Sci. Technol. A, *14(6)*, pp. 2994-3003, 1996.

126. M. Severi and P. Mottier. Etching selectivity control during resist pattern transfer into silica for fabrication of microlenses with reduced spherical aberration, Opt. Eng., *38(1)*, pp. 146-150, 1999.

127. G. Fortuño. Silicon dioxide reactive ion etching dependence on sheath voltage, J. Vac. Sci. Technol. A, *4(3)*, pp. 744-747, 1986.

128. J.W. Coburn. Role of ions in reactive ion etching, J. Vac. Sci. Technol. A, *12(4)*, pp. 1417-1424, 1994.

129. B.A. Rashap. Real-time feedback for etch rate and sidewall profile control in reactive ion etching, PhD thesis, The University of Michigan, 1995.

130. Kris Naessens. Excimer laser ablation of microstructures in polymer for photonic applications, PhD thesis, Universiteit Gent, 2004.
131. N. Lindlein and H.P. Herzig. Design and Modeling of a Miniature System containing Micro-optics, Proc. of SPIE, *4437*, pp. 1-13, 2001.
132. N. Lindlein. Simulation of Micro-optical Systems including Microlens Arrays, J. Opt. A: Pure Appl. Opt., *4*, pp. S1-S9, 2002.
133. N. Lindlein, F. Simon and J. Schwider. Simulation of Micro-optical array systems with RAYTRACE, Opt. Eng., *37(6)*, pp. 1809-1816, 1998.
134. G.H. spencer and M.V.R.K. Murty. General Ray-Tracing Procedure, J. Opt. Soc. Am., *52(6)*, pp. 672-678, 1962.
135. M. Born and E. Wolf. Principles of Optics, pp. 459-490, Cambridge: Cambridge University Press. 1980.
136. J.W. Goodman. Introduction to Fourier Optics, New York: McGraw Hill. 1988.
137. S.A. Miller, J. Pond and B. Michel. Raytracing meets Maxwell’s Equations: Integrating micro- and macro-optical Design, Photonik International, *6*, pp. 76-79, 2005.
138. A. Taflove and S. C. Hagness. Computational Electrodynamics: The Finite-Difference Time-Domain Method, pp. 1-109, Boston: Artech House, 2000.
139. A. Taflove. Review of The Formulation and Applications of The Finite-Difference Time-Domain Method for Numerical Modeling of Electromagnetic Wave Interactions with Arbitrary Structures, Wave Motion, *10*, pp.547-582, 1988.

140. J.G. Maloney, G.S. Smith and W.R. Scott, Jr., Accurate Computation of the Radiation from Simple Antennas using the Finite-Difference Time-domain Method, IEEE Transaction on Antennas and Propagation, *38*, pp. 1059-1068, 1990.

141. P.K. Kelly, J.G. Maloney, B.L. Shirley and R.L. Moore. Photonic Bandgap Structures of Finite Thickness: Theory and Experiment, Proc. IEEE on Antennas and Propagation Society International Symposium, *2*, pp. 718-721, 1994.

142. C.M. Titus, P.J. Bos, J.R. Kelly and E.C. Gartland. Comparison of Analytical Calculations to Finite-Difference Time-Domain Simulations of One-Dimensional Spatial Varying Anisotropic Liquid Crystal Structures, Jpn. J. Appl. Phys., *38*, pp. 1488-1494, 1999.

143. S.C. Hagness, C.D. Rafizadeh, S.T. Ho and A. Taflove. FDTD Microcavity Simulations: Design and Experimental Realization of Waveguide-coupled Single-mode Ring and Whispering-gallery-mode Disk Resonators. J. Lightwave Tech., *15*, pp.2154-2165, 1997.

144. S.T. Chu and S.K Chaudhuri. A Finite-Difference Time-Domain Method for the Design and Analysis of Guided-Wave Optical Structures, J. Lightwave Tech., *7(12)*, pp. 2033-2038, 1989.

145. W.L. Chang and P.K. Wei. Fabrication of a Close-packed Hemispherical Submicron Lens Array and its Application in Photolithography, Opt. Express, *15(11)*, pp. 6774-6783, 2007.

146. B. Archambeault, C. Brench and O.M. Ramahi. EMI/EMC Computational Modeling Handbook, pp. 13-68, Boston: Kluwer Academic. 2001.

147. M. Born and E. Wolf. Principles of Optics, pp. 1-29, Cambridge: Cambridge University Press. 1980.

148. K.S. Yee. Numerical Solution of Initial Boundary Value Problems Involving Maxwell's Equations in Isotropic Media, IEEE Transaction on Antennas and Propagation, *14(3)*, pp. 302-307, 1966.

149. A. Taflove and M.E. Brodwin. Numerical Solution of Steady-State Electromagnetic Scattering Problems using the Time-dependent Maxwell's Equations, IEEE Trans. Microwave Theory and Techniques, *23*, pp. 623-630, 1975.

150. G. Mur. Absorbing Boundary Conditions for the Finite-difference Approximation of the Time-Domain electromagnetic Field Equations, IEEE Trans. Electromagnetic Compatibility, *23*, pp.377-382, 1981.

151. B. Engquist and A. Majda. Absorbing Boundary Conditions for the Numerical Simulation of Waves, Mathematics of Computation, *31*, pp. 629-651, 1977.

152. L.N. Trefethen and L. Halpern. Well-posedness of One-way Wave Equations and Absorbing Boundary Conditions, Mathematics of Computation, *47*, pp.421-435, 1986.

153. J.P. Berenger. A Prefectly Matched Layer for the Absorption of Electromagnetic Waves, J. Computational Phys., *114*, pp. 185-200, 1994.

154. D.M. Hockanson. Perfectly Matched Layers Used as Absorbing Boundaries in a Three-dimensional FDTD Code, Technical report-UMR EMC Laboratory, pp. 1-10

155. S.D. Gedney. An Anisotropic Perfectly Matched Layer-Absorbing Medium for the Truncation of FDTD Lattices, IEEE Trans. Antennas and Propagation, *44(12)*, pp. 1630-1639, 1996.

156. Z.S. Sacks, D.M. Kingsland, R. Lee and J.F. Lee. A Perfectly Matched Anisotropic Absorber for use as an Absorbing Boundary Condition. IEEE Trans. Antennas and Propagation, *43(12)*, pp. 1460-1463, 1995.

157. E. Abbe and J. Roy. Micr. Soc. 2, pp. 300, 1882.

158. F. Yokogawa, S. Ohsawa, T. Iida, Y. Araki, K. Yamamoto, and Y. Moriyama. The Path from a Digital Versatile Disc (DVD) Using a Red Laser to a DVD using a Blue Laser, Jpn. J. Appl. Phys., 3*7,* pp.2176-2178. 1998.

159. I. Ichimura, F. Maeda, K. Osato, K. Yamamoto, and Y. Kasami. Optical Disk Recording Using a GaN Blue-violet Laser Diode, Jpn. J. Appl. Phys., 3*9,* pp.937-942. 2000.

160. I. I. Smolyaninov, D.L. Mazzoni and C.C. Davis. Near-field direct-write ultraviolet lithography and shear force microscopic studies of the lithographic process, Appl. Phys. Lett., *67(26)*, pp. 3859-3861, 1995.

161. Y. Lin, M. H. Hong, W. J. Wang, Y. Z. Law, and T. C. Chong. Sub-30 nm lithography with near-field scanning optical microscope combined with femtosecond laser, Appl. Phys. A. *80*, pp. 461-465, 2005.

162. D. Flanders. Replication of 175-Å lines and spaces in polymethylmethacrylate using x-ray lithography, Appl. Phy. Lett., *36*, pp. 93-96, 1980.
163. K. Early, M. L. Schattenburg, and H. I. Smith. Absence of resolution degradation in X-ray lithography for λ from 4.5nm to 0.83nm, Microelectron. Eng. *11*, pp. 317-321, 1990.
164. J.R. Wendt, G.A. Vawter, R.E. Smith and M.E. Warren. Nanofabrication of subwavelength, binary, high-efficiency diffractive optical elements in GaAs, J. Vac. Sci. Technolo. B, *13*, pp. 2705-2708, 1995.
165. A. N. Broers, J. M. Harper, and W. W. Molzen. 250-Å linewidths with PMMA electron resist, Appl. Phy. Lett., *33*, pp. 392-394, 1978.
166. S. Y. Chou, P. R. Krauss, and P. J. Renstrom. Imprint Lithography with 25-Nanometer Resolution, Science, *272,* pp.85-87. 1996.
167. S. Y. Chou, P. R. Krauss, and P. J. Renstrom. Imprint of Sub-25 nm Vias and Trenches in Polymers, Appl. Phy. Lett., *67,* pp.3114-3116. 1995.
168. K. Sugioka, K. Obatam K. Midorikawa, M.H. Hong, D.J. Wu, L.L. Wong, Y.F. Lu and T.C. Chong. Advanced materials processing based on interaction of laser beam and a medium, J. Photochem and Photobio. A, *158*, pp. 171-178, 2003.
169. J. Wei, N. Hoogen, T. Lippert, O. Nuyken, and A. Wokaun. Novel Laser Ablation Resists for Excimer Laser Ablation Lithography. Influence of Photochemical Properties on Ablation, J. Phys. Chem. B, *105*, pp. 1267-1275, 2001.

170. C J Hayden. Three-dimensional excimer laser micromachining using greyscale masks, J. Micromech. And Microeng., *13*, pp. 599-603, 2003.

171. S.M. Huang, M.H. Hong, B.S. Luk'yanchuk and T.C. Chong. Direct and subdiffraction-limit laser nanofabrication in silicon, Appl. Phys. Lett., *82(26)*, pp. 4809-4811, 2003.

172. K. Piglmayer, R. Denk, and D. Bäuerle. Laser-induced surface patterning by means of microspheres, Appl. Phys. Lett., *80(25)*, pp. 4693-4695, 2002

173. J. Aizenberg and G. Hendler. Designing efficient microlens arrays: lessons from Nature, J. Mat. Chem., *14*, pp. 2066-2072, 2004.

174. L. Xu, S.C. Vemula, M. Jain, S.K. Nam, V.M Donelly, D.J. Economou and P. Ruchhoeft. Nanopantography: A New Method for Massively Parallel Nanopatterning over Large Areas, Nano Lett., *5(12)*, pp. 2563-2568, 2005.

175. Feidhlim T. O'Neill and John T. Sheridan, Photoresist reflow method of microlens production Part I: Background and experiments, Optik, *113(9)*, pp. 391-404, 2002.

176. H. F. Talbot, Phil. Mag. *9*, pp. 401-407, 1836.

177. B. Besold and N. Lindlein, Practical limitaitons of talbot imaging with microlens arrays, Pure Appl. Opt., *6*, pp. 691-698, 1997.

178. B. Besold and N. Lindlein. Fractional Talbot effect for periodic microlens arrays, Opt. Eng., *36*, pp. 1099-1105, 1997.

179. Y. Lin, M. H. Hong, G. X. Chen, C. S. Lim, Z. B. Wang, L. S. Tan, L. P. Shi, and T. C. Chong. Microlens array patterning on phase change film. In 1st

International Symposium on Functional Materials 2005, 2005, Kuala Lumpur, Malaysia, pp. 737-746.

180. A. Birner, R.B. Wehrspohn, U.M. Gösele and K. Busch. Silicon-Based Photonic Crystals, Adv. Mat., 13(6), pp. 377-388, 2001.

LIST OF PUBLICATIONS

Journal Papers:

1. C. S. Lim, M. H. Hong, A. Senthil Kumar, M. Rahman and X. D. Liu, *Fabrication of Concave Micro Lens Array using Laser Patterning and Isotropic Etching,* Int'l Journal of Machine Tools and Manufacture, 46(5), 2006, pp. 552-558
2. C. S. Lim, M. H. Hong, Y. Lin, Q. Xie, A. S. Kumar, M. Rahman, and S. Z. Lee, *Microlens arrays fabrication by laser interference lithography for super resolution surface nanopatterning,* Appl. Phy. Lett., 89, 191125 (2006).
3. C.S. Lim, M.H. Hong, Y. Lin, G.X. Chen, A. Senthil Kumar, M. Rahman, G.C. Lim, *Sub-Micron Surface Nanopatterning by laser irradiation through Microlens Arrays*, J. Materials Processing Technology, 192–193 (2007) pp. 328–333
4. C.S. Lim, M.H.Hong, Y. Lin, L. S. Tan, A. Senthil Kumar, and M. Rahman, *Large Area Parallel Surface Nanostructuring with Laser Irradiation through Microlens Arrays*, Surface Review and Letter, Accepted (2007).
5. Y. Lin, M. H. Hong, C. S. Lim, G. X. Chen, L. S. Tan, Z. B. Wang, L. P. Shi, and Chong. T. C., *Ultrafast-laser-induced parallel phase-change nanolithography*, Appl. Phy. Lett., 89, 041108 (2006).
6. Y. Lin, M. H. Hong, G. X. Chen, C. S. Lim, L. S. Tan, Z. B. Wang, L. P. Shi, and T. C. Chong, H*ybrid laser micro/nanofabrication of phase change materials with combination of chemical processing*, J. Materials Processing

Technology, 192–193 (2007) pp. 340–345.

Conference Papers:

7. Chin Seong Lim, MingHui Hong, A. Senthil Kumar, M. Rahman and XiangDong Liu, *Technique for Fabrication of Micro Lens Arrays Combining Laser Patterning and Wet Etching*, ICMAT 2005, Singapore.

8. C.S. Lim, M.H.Hong, Y. Lin, L. S. Tan, A. Senthil Kumar, M. Rahman, *Large Area Parallel Surface Nanostructuring using Microlens Arrays*, 2nd International Symposium on Functional Materials, Hangzhou, 2007.

9. M.H. Hong, F. Ma, C.S. Lim, Y. Lin, Z.Q. Huang, L.S. Tan, L.P. Shi and T.C. Chong, *Multi-lens Array Fabrication and its Applications in Laser Precision Engineering*, The 8th International Symposium on Laser Precision Microfabrication, Vienna, Austria, p. 49, 2007.

10. L. S. Tan, M. H. Hong, Y. Lin, C. S. Lim, *Laser Nanoimprinting Technique for a Large Area Surface Nanostructuring*, 51st International Conference on Electron, Ion, and Photon Beam Technology & Nanofabrication 2007.

11. Y. Lin, M.H. Hong, L.S. Tan, C.S. Lim, L.P. Shi and T.C. Chong, 3D *Micro/Nano-structure Fabrication of Phase-change film*, The 8th International Symposium on Laser Precision Microfabrication, p. 149, 2007.

APPENDIX A

VISUAL BASIC SCRIPT FOR FDTD SIMULATOR

The following script describe the VB script that is used to create layout and to perform FDTD simulation by the FDTD simulator.

```
Dim Sphere1
Set Sphere1 = WGMgr.CreateObj ( "WG3DSphere",  WGMgr.FindID( "Sphere" ) )

'Set position for Sphere1
Sphere1.SetPositionExpr "", "", ""
Sphere1.SetPosition   -1,    1,  2.1

'Set orientation for Sphere1
Sphere1.SetOrientationExpr "", "", ""
Sphere1.SetOrientationOffset    0,    0,    0

'Set material name for Sphere1
Sphere1.SetMaterial "n=1.54"

'Set clipping plane for Sphere1

Sphere1.SetRadiusExpr "0.9083"

Dim Sphere2
Set Sphere2 = WGMgr.CreateObj ( "WG3DSphere",  WGMgr.FindID( "Sphere" ) )

'Set position for Sphere2
Sphere2.SetPositionExpr "", "", ""
Sphere2.SetPosition    1,    1,  2.1

'Set orientation for Sphere2
Sphere2.SetOrientationExpr "", "", ""
Sphere2.SetOrientationOffset    0,    0,    0

'Set material name for Sphere2
Sphere2.SetMaterial "n=1.54"

'Set clipping plane for Sphere2

Sphere2.SetRadiusExpr "0.9083"

Dim Sphere3
Set Sphere3 = WGMgr.CreateObj ( "WG3DSphere",  WGMgr.FindID( "Sphere" ) )
```

```
'Set position for Sphere3
Sphere3.SetPositionExpr "", "", ""
Sphere3.SetPosition   -1,    3,  2.1

'Set orientation for Sphere3
Sphere3.SetOrientationExpr "", "", ""
Sphere3.SetOrientationOffset    0,    0,    0

'Set material name for Sphere3
Sphere3.SetMaterial "n=1.54"

'Set clipping plane for Sphere3

Sphere3.SetRadiusExpr "0.9083"

Dim Sphere4
Set Sphere4 = WGMgr.CreateObj ( "WG3DSphere",  WGMgr.FindID( "Sphere" ) )

'Set position for Sphere4
Sphere4.SetPositionExpr "", "", ""
Sphere4.SetPosition    1,    7,  2.1

'Set orientation for Sphere4
Sphere4.SetOrientationExpr "", "", ""
Sphere4.SetOrientationOffset    0,    0,    0

'Set material name for Sphere4
Sphere4.SetMaterial "n=1.54"

'Set clipping plane for Sphere4

Sphere4.SetRadiusExpr "0.9083"

Dim Block1
Set Block1 = WGMgr.CreateObj ( "WG3DBlock",  WGMgr.FindID( "Block" ) )

'Set position for Block1
Block1.SetPositionExpr "", "", ""
Block1.SetPosition    0,  2.5, 1.8583

'Set orientation for Block1
Block1.SetOrientationExpr "", "", ""
Block1.SetOrientationOffset    0,    0,    0

'Set material name for Block1
Block1.SetMaterial "n=1.54"

'Set clipping plane for Block1

Block1.SetV1zExpr "2"
```

```
Block1.SetV2xExpr "8"
Block1.SetV2zExpr "0"
Block1.SetV3xExpr ""
Block1.SetV3yExpr "11"
Block1.SetV3zExpr ""

Dim Sphere5
Set Sphere5 = WGMgr.CreateObj ( "WG3DSphere",  WGMgr.FindID( "Sphere" ) )

'Set position for Sphere5
Sphere5.SetPositionExpr "", "", ""
Sphere5.SetPosition    3,    1,  2.1

'Set orientation for Sphere5
Sphere5.SetOrientationExpr "", "", ""
Sphere5.SetOrientationOffset    0,    0,    0

'Set material name for Sphere5
Sphere5.SetMaterial "n=1.54"

'Set clipping plane for Sphere5

Sphere5.SetRadiusExpr "0.9083"

Dim Sphere6
Set Sphere6 = WGMgr.CreateObj ( "WG3DSphere",  WGMgr.FindID( "Sphere" ) )

'Set position for Sphere6
Sphere6.SetPositionExpr "", "", ""
Sphere6.SetPosition    3,    7,  2.1

'Set orientation for Sphere6
Sphere6.SetOrientationExpr "", "", ""
Sphere6.SetOrientationOffset    0,    0,    0

'Set material name for Sphere6
Sphere6.SetMaterial "n=1.54"

'Set clipping plane for Sphere6

Sphere6.SetRadiusExpr "0.9083"

Dim Sphere7
Set Sphere7 = WGMgr.CreateObj ( "WG3DSphere",  WGMgr.FindID( "Sphere" ) )

'Set position for Sphere7
Sphere7.SetPositionExpr "", "", ""
Sphere7.SetPosition    3,    5,  2.1

'Set orientation for Sphere7
```

```
Sphere7.SetOrientationExpr "", "", ""
Sphere7.SetOrientationOffset    0,    0,    0

'Set material name for Sphere7
Sphere7.SetMaterial "n=1.54"

'Set clipping plane for Sphere7

Sphere7.SetRadiusExpr "0.9083"

Dim Sphere8
Set Sphere8 = WGMgr.CreateObj ( "WG3DSphere",  WGMgr.FindID( "Sphere" ) )

'Set position for Sphere8
Sphere8.SetPositionExpr "", "", ""
Sphere8.SetPosition    3,    3,  2.1

'Set orientation for Sphere8
Sphere8.SetOrientationExpr "", "", ""
Sphere8.SetOrientationOffset    0,    0,    0

'Set material name for Sphere8
Sphere8.SetMaterial "n=1.54"

'Set clipping plane for Sphere8

Sphere8.SetRadiusExpr "0.9083"

Dim Sphere9
Set Sphere9 = WGMgr.CreateObj ( "WG3DSphere",  WGMgr.FindID( "Sphere" ) )

'Set position for Sphere9
Sphere9.SetPositionExpr "", "", ""
Sphere9.SetPosition   -3,    7,  2.1

'Set orientation for Sphere9
Sphere9.SetOrientationExpr "", "", ""
Sphere9.SetOrientationOffset    0,    0,    0

'Set material name for Sphere9
Sphere9.SetMaterial "n=1.54"

'Set clipping plane for Sphere9

Sphere9.SetRadiusExpr "0.9083"

Dim Sphere10
Set Sphere10 = WGMgr.CreateObj ( "WG3DSphere",  WGMgr.FindID( "Sphere" ) )

'Set position for Sphere10
```

```
Sphere10.SetPositionExpr "", "", ""
Sphere10.SetPosition   -3,    5,  2.1

'Set orientation for Sphere10
Sphere10.SetOrientationExpr "", "", ""
Sphere10.SetOrientationOffset    0,    0,    0

'Set material name for Sphere10
Sphere10.SetMaterial "n=1.54"

'Set clipping plane for Sphere10

Sphere10.SetRadiusExpr "0.9083"

Dim Sphere11
Set Sphere11 = WGMgr.CreateObj ( "WG3DSphere",  WGMgr.FindID( "Sphere" ) )

'Set position for Sphere11
Sphere11.SetPositionExpr "", "", ""
Sphere11.SetPosition   -3,    3,  2.1

'Set orientation for Sphere11
Sphere11.SetOrientationExpr "", "", ""
Sphere11.SetOrientationOffset    0,    0,    0

'Set material name for Sphere11
Sphere11.SetMaterial "n=1.54"

'Set clipping plane for Sphere11

Sphere11.SetRadiusExpr "0.9083"

Dim Sphere12
Set Sphere12 = WGMgr.CreateObj ( "WG3DSphere",  WGMgr.FindID( "Sphere" ) )

'Set position for Sphere12
Sphere12.SetPositionExpr "", "", ""
Sphere12.SetPosition   -3,    1,  2.1

'Set orientation for Sphere12
Sphere12.SetOrientationExpr "", "", ""
Sphere12.SetOrientationOffset    0,    0,    0

'Set material name for Sphere12
Sphere12.SetMaterial "n=1.54"

'Set clipping plane for Sphere12

Sphere12.SetRadiusExpr "0.9083"
```

```
Dim Sphere13
Set Sphere13 = WGMgr.CreateObj ( "WG3DSphere",  WGMgr.FindID( "Sphere" ) )

'Set position for Sphere13
Sphere13.SetPositionExpr "", "", ""
Sphere13.SetPosition   -1,    7,  2.1

'Set orientation for Sphere13
Sphere13.SetOrientationExpr "", "", ""
Sphere13.SetOrientationOffset    0,    0,    0

'Set material name for Sphere13
Sphere13.SetMaterial "n=1.54"

'Set clipping plane for Sphere13

Sphere13.SetRadiusExpr "0.9083"

Dim Sphere14
Set Sphere14 = WGMgr.CreateObj ( "WG3DSphere",  WGMgr.FindID( "Sphere" ) )

'Set position for Sphere14
Sphere14.SetPositionExpr "", "", ""
Sphere14.SetPosition   -1,    5,  2.1

'Set orientation for Sphere14
Sphere14.SetOrientationExpr "", "", ""
Sphere14.SetOrientationOffset    0,    0,    0

'Set material name for Sphere14
Sphere14.SetMaterial "n=1.54"

'Set clipping plane for Sphere14

Sphere14.SetRadiusExpr "0.9083"

Dim Sphere15
Set Sphere15 = WGMgr.CreateObj ( "WG3DSphere",  WGMgr.FindID( "Sphere" ) )

'Set position for Sphere15
Sphere15.SetPositionExpr "", "", ""
Sphere15.SetPosition    1,    5,  2.1

'Set orientation for Sphere15
Sphere15.SetOrientationExpr "", "", ""
Sphere15.SetOrientationOffset    0,    0,    0

'Set material name for Sphere15
Sphere15.SetMaterial "n=1.54"
```

```
'Set clipping plane for Sphere15

Sphere15.SetRadiusExpr "0.9083"

Dim Sphere16
Set Sphere16 = WGMgr.CreateObj ( "WG3DSphere",  WGMgr.FindID( "Sphere" ) )

'Set position for Sphere16
Sphere16.SetPositionExpr "", "", ""
Sphere16.SetPosition    1,    3,  2.1

'Set orientation for Sphere16
Sphere16.SetOrientationExpr "", "", ""
Sphere16.SetOrientationOffset    0,    0,    0

'Set material name for Sphere16
Sphere16.SetMaterial "n=1.54"

'Set clipping plane for Sphere16

Sphere16.SetRadiusExpr "0.9083"

Dim InputPlane1
Set InputPlane1 = InputPlaneMgr.CreateInputObj ("Pulse", "Rectangular",
InputPlaneMgr.FindID( "InputPlane"), "Vertical" )
'Common data for 2D and 3D.
InputPlane1.SetPosition    0
InputPlane1.SetDirection "Forward"
InputPlane1.SetWaveLength "0.248"
InputPlane1.SetTimeHalfWidth "23e-9"
InputPlane1.SetTimeOffset "4.0e-14"
InputPlane1.SetEnabled  True
'Data for 2D.
InputPlane1.SetAmplitudeOrPower "Amplitude", "1.0"
InputPlane1.SetRefLocal
InputPlane1.SetCenterPos "0.0"
InputPlane1.SetHalfWidth "0.5"
InputPlane1.SetTiltingAngle "0"
'Data for 3D.
InputPlane1.SetAmplitudeExpr3D "1.0"
InputPlane1.SetRefLocal3D
InputPlane1.SetCenterPosExpr3D "0.0", "4"
InputPlane1.SetHalfWidthExpr3D "50", "50"
InputPlane1.SetTiltingAngleExpr3D "0"
InputPlane1.SetLYPolarization3D
InputPlane1.RefreshInputField

Const NumIterations = 1

For x = 1 to NumIterations
```

```
    ParamMgr.Simulate
    WGMgr.Sleep( 50 )
Next
```